PARAMETRIC MODELING TO DESIGN PERIODIC HYDRAULIC TESTS AND DETERMINE FRACTURE CONNECTIVITY AT THE UTAH FRONTIER OBSERVATORY FOR RESEARCH IN GEOTHERMAL ENERGY

A THESIS

Presented to the Department of Earth Science

California State University, Long Beach

In Partial Fulfillment

of the Requirements for the Degree

Master of Science in Geology

Committee Members:

Matthew Becker, Ph.D. (Chair)
Benjamin Hagedorn, Ph.D.
Alyssa Abbey, Ph.D.

College Designee:

Lora Landon-Stevens, Ph.D.

By Megan Ward-Baranyay

B.S., 2021, California State Polytechnic University, Pomona

December 2023

ABSTRACT

Stimulated fracture hydraulic connectivity between injecting and producing wells is a critical prerequisite for efficient enhanced geothermal systems (EGS) thermal recovery. To measure connectivity and optimize injection rates and periods for EGS, Distributed Acoustic Sensing (DAS) may be used as a sensor for hydraulic testing. In this mode, DAS strain measurements are a proxy for fluid pressure. Periodic hydraulic tests monitored by DAS are proposed at the Utah Frontier Observatory for Research in Geothermal Energy (FORGE) to understand flow continuity between injecting and producing wells for EGS. Herein are described parametric hydromechanical models generated to understand how various hydraulic test design parameters affect DAS response, including injection rate, injection duration for each pulse, and number of repeated pulses to use in the test. These simulations, based on measured properties, were applied to decipher the system response to injection and optimize injection rates and periods. After hydraulic stimulation, fractures may be incomplete, approaching but not intersecting the production well. These "near-miss" fractures can be addressed in future stimulation stages or re-stimulated to complete the connection. We investigated the use of DAS as a method by which near-miss stimulated fractures may be identified and distinguished from hydraulically connected fractures. The low-frequency sub-nanostrain signatures of both complete and near-miss fractures in DAS data were simulated in this study using a hydrogeomechanical discrete fracture network model. The spatial distribution of strain was found to be an accurate indication of hydraulically stimulated fractures. However, this indicator must be evaluated in the context of DAS gauge length and spatial sampling. These simulations are a precursor to tests to be conducted at the Utah Frontier Observatory for Research in Geothermal Energy (FORGE) in 2024.

TABLE OF CONTENTS

LIST OF TABLES

LIST OF FIGURES

CHAPTER 1

INTRODUCTION

1.1 Motivation

Faced with the urgent need for inexhaustible, renewable energy available at all times, researchers look to new technologies to expand the production of geothermal energy, which has significant potential to improve energy security (Tester et al., 2006). Currently, geothermal power is generated by the extraction of heat from natural hydrothermal circulation systems. Enhanced Geothermal Systems (EGS) enable heat extraction from formations that are naturally hot, but do not permit fluid movement, thus overcoming the limits of where geothermal power may be produced (Tester et al., 2006). An EGS reservoir is engineered by creating new flow pathways, that is, fracture permeability, in hot bedrock. The enhanced permeability allows fluid to be circulated between injection and production well pairs to extract thermal energy. Permeability is created through hydraulic fracturing or shear activation (stimulation) of the rock mass, developing a fracture network that hydraulically connects wells. EGS has the potential to provide cost-effective, environmentally conscious, renewable energy to communities around the globe (Duchane and Brown, 2002). Tester et al. (2006) estimated that EGS contains a total resource base of at least 10^6 exajoules (EJ) in the U.S. from bottom-hole temperature and geologic data. An estimate of 100 GW_e U.S. commercial EGS power production capabilities over the next few decades was calculated from reasonable resource and market prices (Tester et al., 2006). However, the economic viability of EGS is closely tied to an even distribution of fluid flow through the fracture network.

The Utah Frontier Observatory for Research in Geothermal Energy is a testbed to demonstrate that EGS technologies have the potential to contribute significantly to future power generation (Moore et al., 2019). It is necessary to understand flow continuity between EGS injecting and producing wells to extract this energy efficiently and cost effectively. To evaluate the stimulated fracture network connecting the injection well 16A(78)-32 and a production well 16B(78)-32, periodic hydraulic testing will be conducted. Fluid will be injected in 16A and the hydromechanical response observed in 16B. To detect the distribution of flow response in 16B, rock strain will be measured using low-frequency fiber optic distributed acoustic sensing (DAS) as well as Brillouin distributed strain sensing (DSS) observations. Fluid pressure increase in fractures will result in displacement of fractures in the connected networks, which can be measured at sub-nanostrain levels using DAS (Becker et al., 2017). Because DAS is best suited to measuring strain rate, the dynamic fluid behavior will be enhanced by injecting fluid as a series of pulses. An additional objective of these experiments is to identify any stimulated fractures that are close, but do not intersect the production well by sensing their extensional strain rate fronts as the fractures open and compressional stress shadows as the fractures close. These “near-miss” fractures are of interest because they may be extended to the production well by re-stimulation in targeted stages to complete incomplete connections. To prepare for and assist with the design of periodic hydraulic tests to be conducted at Utah FORGE, simulations of various test design parameters were experimented on a hydromechanical numerical model of the FORGE reservoir.

1.2 Approach

To assist with injection strategies at FORGE, we developed forward parametric numerical models to understand how injection test design affects the interrogation of the stimulated flow system at FORGE. These hypothetical models, based on measured properties, will be used to design post-stimulation periodic hydraulic tests to be conducted at FORGE and contribute to improving fracture connectivity. To our knowledge, hydraulic testing of this type has not been conducted at a geothermal site using DAS as the measurement modality. We created a numerical model involving a fracture network connecting the injection well 16A(78)-32 and a planned production well 16B(78)-32 in the granitoid basement at FORGE in COMSOL® Multiphysics. COMSOL is a generic finite element multiphysics numerical simulator. COMSOL solved a time-dependent study to simulate the DAS hydromechanical response to periodic injection.

Parametric studies were conducted to understand how various design parameters affect DAS response, including injection rate, injection duration for each pulse, and number of repeated pulses to use in the test. Because the fracture permeability is currently unknown, a range of fracture apertures were included in the parametric simulations. The range of apertures used is supported by fullbore formation microimager (FMI) log data, wells test, and modeling (Finnila et al., 2021). To determine how DAS may contribute to improving fracture connectivity by identifying zones that can be re-stimulated to complete the connection, both complete and "near-miss" fractures were simulated in this study using a hydromechanical discrete fracture network (DFN) model with geometry variations. Predicted DAS response to these simulations was achieved by post-processing the strain data from the COMSOL solution in MATLAB. We performed a numerical assessment to align our results with a simulation carried out by Ratnayake and Ghassemi in 2023, as the authors of the latter will leverage the results of our study in shaping the test designs for FORGE. The modeling workflow developed in this study may be used for DAS hydraulic tests at EGS reservoirs at FORGE and elsewhere.

CHAPTER 2

PREVIOUS WORK

2.1 Current Standard Methods

Hydraulic testing is a standard method for characterizing hydraulically connected fractures in geothermal reservoirs. Traditional hydraulic tests in fractured bedrock are usually insensitive to heterogeneous permeability, transmissivity, and storativity due to a large radius of influence associated with low effective porosity (Guiltinan, 2012). However, periodic hydraulic tests are more sensitive to heterogeneous hydraulic properties than constant-rate tests (Becker and Guiltinan, 2010). Fluid pressure increase in fractures in response to periodic hydraulic testing results in displacement of fractures in connected networks, and Becker et al. (2017) demonstrated that DAS can be used to measure this displacement at sub-nanostrain levels in EGS reservoir conditions.

2.2 Enhanced Geothermal Systems

Natural hydrothermal systems, such as those in Mammoth Lakes, USA and the Salton Sea Geothermal Field, USA, contain a natural plumbing system (permeability), a sufficient water source, and a shallow heat source. These natural systems are rare. However, heat exists at depth everywhere on Earth. Natural hydrothermal systems can be mimicked if permeability is created through hydraulic fracturing. This concept of Enhanced Geothermal Systems (EGS) reduces the limitations of the extraction of geothermal energy (McClure, 2009).

To create an EGS reservoir, a well is drilled to a target depth through which water is injected deep into crystalline bedrock to create permeability by enhancing natural fractures and creating new ones (McClure, 2009) (Figure 1). This process is referred to as stimulation. An important factor when selecting an EGS site is the geothermal gradient, or how temperature increases with depth. Most commonly, energy is extracted from EGS by injecting water deep into an enhanced natural fracture network in the subsurface, as the subsurface typically increases in temperature with increasing depth. The water, heated by flowing through the hot, fractured rock pathways, is then brought back to the surface through a second well. After producing electricity from steam-driven turbines, the water is recycled, as in it is injected back into the subsurface, for continuous heat extraction (McClure, 2009).

The hot rock containing the fracture network through which the water circulates must be sustainable. If injected fluid is constrained to only a few fracture pathways and not dispersed across many fractures, the pathways will cool quickly, known as short-circuiting. The cost to develop EGS reservoirs is high, specifically due to drilling. Due to the high cost of developing an EGS reservoir, short-circuiting must be prevented (McClure, 2009).

As discussed by Duchane and Brown (2002), the first EGS test site was in the granodiorite Fenton Hill reservoir in New Mexico, USA with development beginning in 1974. In an attempt to connect the first two drilled boreholes in the Phase 1 reservoir, fractures were stimulated, but their locations were insufficiently mapped. Flow tests showed that flow was constrained to few pathways, which cooled quickly. Cooling of the reservoir during the first three flow tests totaling 108 days indicated that the fracture network was not well-dispersed within the reservoir. After 9 months of stimulation, the wells were hydraulically connected, and the produced fluid temperature declined by 7°C, from 156°C to 149°C. Flow channeling, which is when preferential pathways transport most of the fluid, causes local thermal drawdown, which acts as positive feedback in that it exacerbates flow channeling due to fracture aperture increase caused by thermal stress (Guo et al., 2016). Thermal drawdown reduces the productivity of EGS. Stimulation had to be reattempted after well connectivity failed. The Phase 2 system at Fenton hill was deeper and hotter. The Phase 1 reservoir was between 180°C to 200°C at a depth of 2800 to 2950 m, while the Phase 2 reservoir was approximately 240°C at 3500 m depth (Kelkar et al., 2016). Initially, stimulation failed to connect the inclined wells that were drilled up to 4400 m depth. After additional drilling and stimulation, the wells were successfully hydraulically connected, water loss declined over time, and dissolved solid concentrations never exceeded 10% of seawater (Duchane and Brown, 2002). However, circulation standards for commercial purposes were not accomplished. Fluid production rates of 5 to 7 l/s were achieved, but commercial standards require 80 l/s (Kelkar et al., 2016; Tester et al., 2006). Seismic studies indicated that pre-existing natural fractures and sealed joints were opened by stimulation (Duchane and Brown, 2002). Several EGS test sites have been attempted worldwide since then, an incomplete list is shown in Table 1. Based on these rigorous tests, it is reasonable to conclude that if EGS are designed advisedly, sustainable reservoirs can be accomplished.

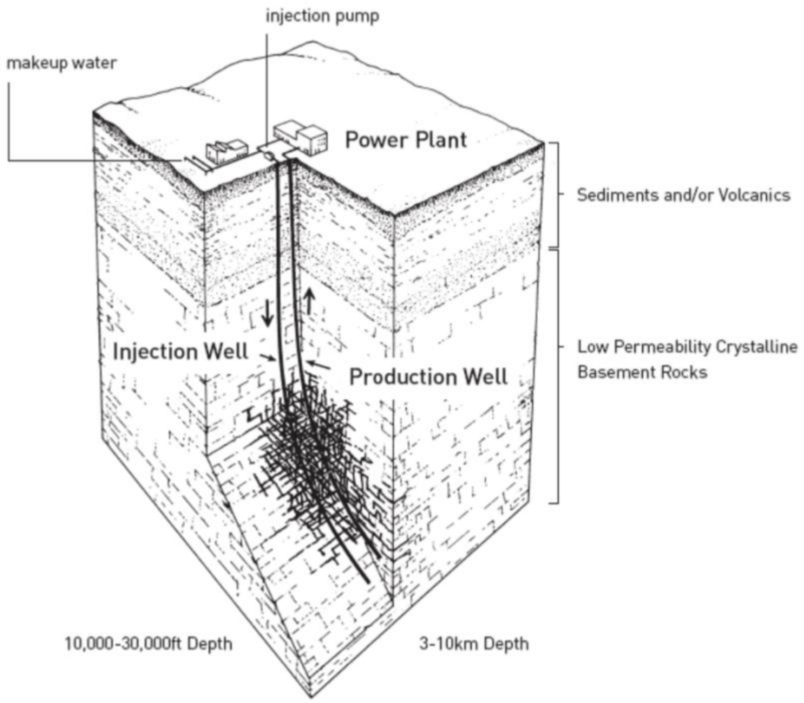

FIGURE 1. Schematic of a two-well EGS reservoir in low-permeability crystalline bedrock (Tester et al., 2006).

TABLE 1. Permeability, Circulation Rates, and Wellhead Pressures for Existing EGS Sites

EGS Site	**Injection Well TVD (m)**	**Pre-Stimulation Permeability (m^2)**	**Post-Stimulation Permeability (m^2)**	**Circulation Flow Test Rate (L/s)**	**Well Head Pressure (psi)**	**Flow Test Date**	**Reference**
Fenton Hill	3940	--	--	11	3890	1986	(Nathenson, 1999)
Rosemanowes	2115	--	--	5	580	1985	(Nathenson, 1999)
Soultz	5000	3.5E-17 to 2.5E-17	1.6E-15 to 4.5E-14	31	1059	2008	(Schill et al., 2017) (Audigane et al., 2002)
Ogachi	990	3E-15 to 1E-16	1E-13 to 1E-14	7 to 20	2756	1993	(Kaieda, 2012)
Desert Peak	1768	2E-15 to 1.2E-16	5.6E-13 to 1.1E-14	32	750	2011	(Benato et al., 2016) (Chabora et al., 2012)

2.3 Periodic Hydraulic Testing

Characterization of flow through fracture networks by periodic hydraulic testing has been successfully demonstrated in previous work (Guiltinan and Becker, 2015; Fokker, 2013; Rasmussen et al., 2003). A benefit of period hydraulic testing is that EGS operations may continue during periodic hydraulic tests to determine hydraulic properties by merely varying injection or pumping rates. Periodic hydraulic tests are conducted by creating an oscillating head in one well, in which water is displaced periodically, and observing the corresponding oscillatory head response in observation wells (Renner and Messar, 2006). Periodic injection can be an indicator of hydraulic connectivity by measuring the change in fluid pressure in an observation well (Oliver et al., 2018). Periodic tests conducted at varying frequencies allow for interrogation of different regions of the granitoid rock formation, and it is particularly effective in bedrock systems because of their small storativity results in rapid propagation of pressure signals (Guiltinan and Becker, 2015).

Hydraulic diffusivity, defined as the ratio of transmissivity to storativity, has been suggested as a reliable indicator of flow pathways in heterogenous reservoirs (Knudby and Carrera, 2006). Periodic hydraulic testing has been shown to provide reliable measurements of hydraulic diffusivity (Guiltinan and Becker, 2015; Fokker, 2013). Longer periods of hydraulic oscillation leads to larger areas of interrogation, providing the ability to "tune" the test to specific zones surrounding the injection well. This is because the radius of influence is related to the square root of the product of the hydraulic diffusivity and the oscillation period under radial flow (Bakker, 2008).

In a study by Becker and Guiltinan (2010), hydraulic diffusivity was determined by fitting the hydraulic diffusion equation with drawdown data from their periodic hydraulic test based on work by Renner and Messar (2006) (Equation 1). The periodic head disturbance can be described in the Laplace domain by a sinusoidal input function:

$$\bar{\delta}_s = p_0\left(\frac{\omega}{s^2+\omega^2}\right) exp\left(\frac{\theta s}{\omega}\right) \tag{1}$$

where p_0 is the amplitude of the pressure disturbance well, ω is the frequency of the disturbance, θ is the phase shift, and s is the Laplace variable (Becker and Guiltinan, 2010). The formation transfer function was related to the pressure pulse propagation from the pumping well:

$$\bar{\delta}_f = \frac{K_0\left(r\sqrt{\frac{s}{D}}\right)}{K_0\left(r_w\sqrt{\frac{s}{D}}\right)} \tag{2}$$

where K_0 is the modified Bessel function of the second kind and zero order, r is the radial distance to the observation well, r_w is the radius of the pumping well, and D is the hydraulic diffusivity (Becker and Guiltinan, 2010). Multiplication of these equations in the Laplace domain, equivalent to convolution in the time domain, results in total observed pressure response ($\bar{\delta}_t$):

$$\bar{\delta}_t = \bar{\delta}_s \cdot \bar{\delta}_f. \tag{3}$$

Rasmussen et al. (2003) developed a period hydraulic testing method by creating a sinusoidal pressure signal that diffused into two deep confined aquifers and one shallow aquifer. The Theis analytical solution was modified to represent sinusoidal pumping rate in a confined aquifer. Their analytical solutions were validated with finite element simulation numerical solutions. Aquifer hydraulic properties were determined from the attenuation and phase lag of the signal since the period and the amplitude of the signal were known. Their results for the deep confined aquifers matched that of previous studies. In their analytical solutions, Rasmussen et al. (2003) define the amplitude of drawdown fluctuations in an observation well as:

$$|s| = \frac{Q_0}{2\pi T}\left|K_0\left(r\sqrt{\frac{i\omega}{D}}\right)\right| = \frac{Q_0}{2\pi T}\left|K_0\left(r\sqrt{\frac{i2\pi}{DP}}\right)\right| \tag{4}$$

where s is the drawdown, Q_0 is the amplitude of the pumping rate, T is the transmissivity, K_0 is the zero-order modified Bessel function of the second kind, r is the radial distance from the pumping well i is the imaginary number, ω is the frequency, D is the hydraulic diffusivity, P is the period of oscillation. As the period increases, the Bessel function of the second kind argument increases rapidly. Therefore, there is a large sensitivity to period and hydraulic diffusivity, which relates to permeability. Hydraulic testing can interrogate the formation at various depth as calculated by the radius of influence, r_i (Guiltinan and Becker, 2015):

$$r_i = 1.5\sqrt{DP}. \tag{5}$$

Therefore, increasing the period of oscillation for the hydraulic test will interrogate farther into the formation. The relationship between diffusivity and radius of influence indicates that there is a larger radius of influence for a formation with larger permeability.

2.4 Distributed Acoustic Sensing

Distributed acoustic sensing (DAS) measures oscillating strain rates along the length of a fiber optic (FO) cable cemented into a well (Becker et al., 2017) (Figure 2). The DAS system includes the FO cable and interrogator unit that uses laser optical phase demodulation to measure strain rate along the length of the cable at paired positions separated by gauge length (Becker et al., 2017). The interrogator analyzes the Rayleigh-scattering of light from light pulses emitted into the fiber. When the fiber stretches or compresses, it causes changes in the optical path of the light. By analyzing changes in the optical path length over a specific distance, DAS measures the tensile or compressive strain along the fiber (Daley et al., 2016) (Figure 3). Strain between the two points is proportional to the change in phase-lag of the light pulses emitted into the fiber (Bakku et al., 2014) (Figure 3). DAS response corresponds to the stretching of the fiber over the gauge length, ∂z. The gauge length is the specific distance, separated by two points, over which DAS measures the strain. The value of that strain measurement is linked to the center point of the moving window which has a size determined by gauge length (Daley et al., 2016). The time derivative of strain $(\partial u/\partial z)$, Equation 4, and the spatial derivative of displacement rate $(\partial u/\partial t)$, Equation 5, are equivalent (Daley et al., 2016):

$$\frac{\partial}{\partial t}\left(\frac{\partial u}{\partial z}\right) \tag{6}$$

$$\frac{\partial}{\partial z}\left(\frac{\partial u}{\partial t}\right). \tag{7}$$

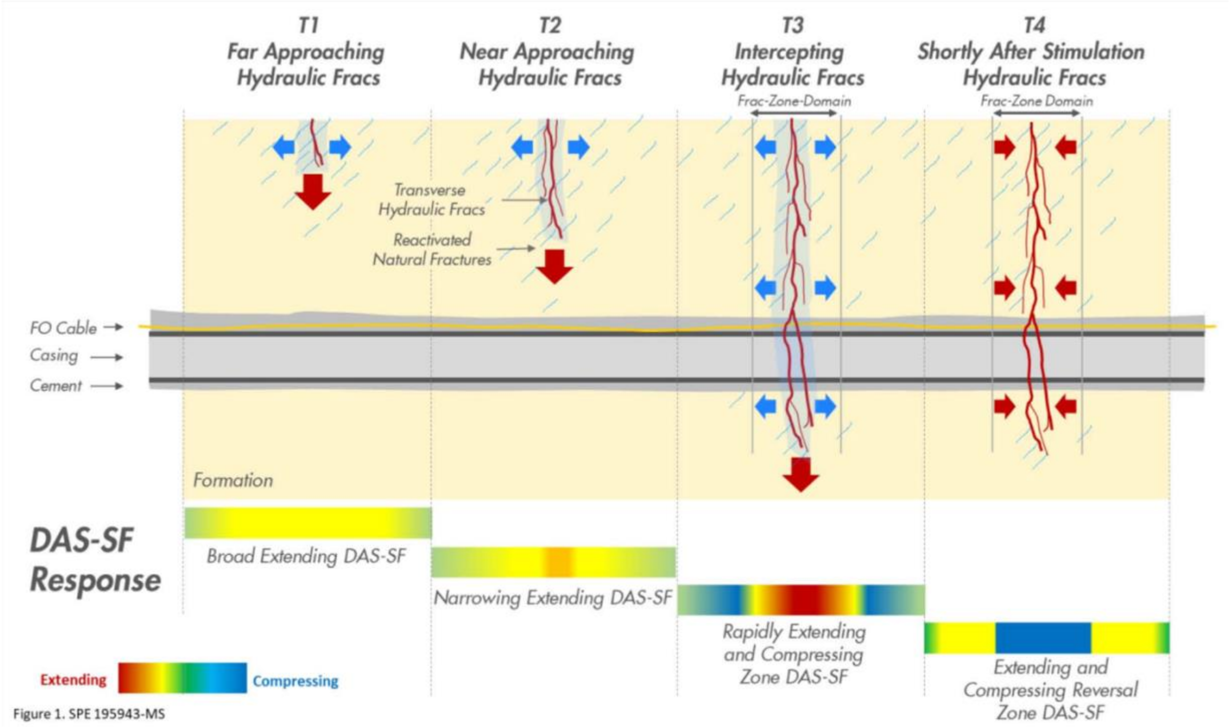

FIGURE 2. Hypothetical DAS response illustrating an extensional strain front (T1 and T2), compressional stress shadow (T3), and reversal (T4) (Ugueto et al., 2019).

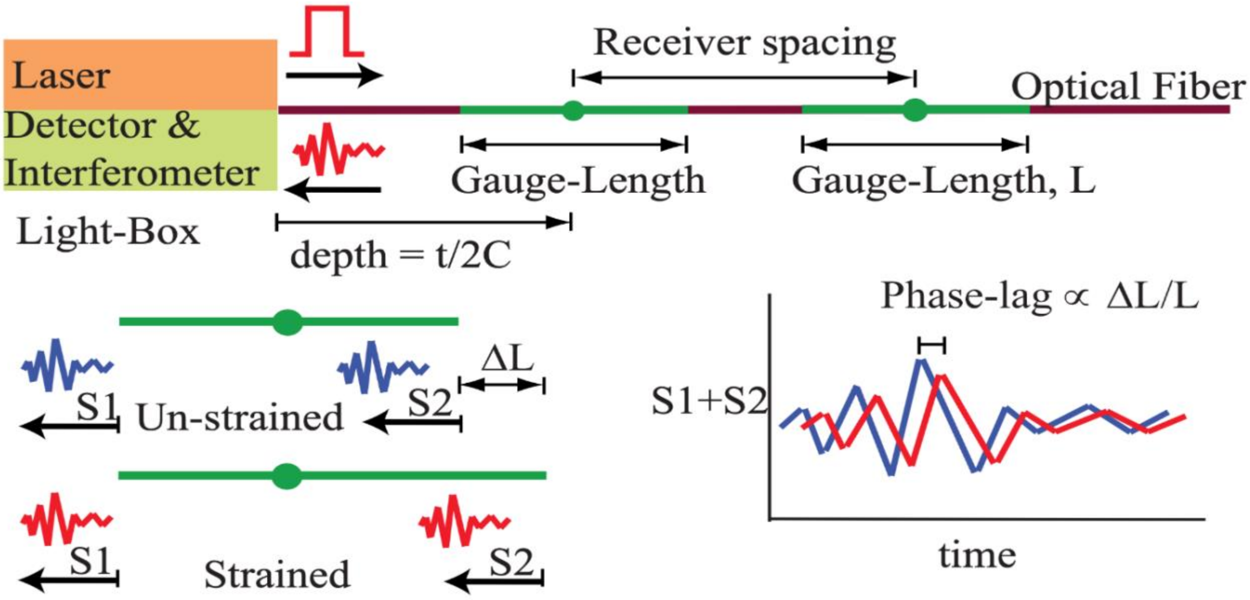

FIGURE 3. Schematic of DAS system and gauge length. Distributed strain response is measured using DAS between two points along the fiber optic cable across a moving window, or gauge length. Strain between the two points is proportional to the change in phase-lag of the light pulses (S1+S2) emitted into the fiber (Bakku et al., 2014).

DAS can be used to map and monitor hydraulic pathways in EGS reservoirs by detecting fluid pressure continuously without interrupting field operations (Oliver et al., 2018). Fluid pressure changes in fractures will result in displacement (dilation or contraction) of fracture aperture in the connected networks. Dynamic aperture displacement is measured at sub-nanostrain levels by DAS at sampling rate frequencies between 1 μHz and 1 kHz (Becker and Coleman, 2019). Displacement is measured only along the fiber, i.e., lengthening and shorting. It is relatively sensitive to hydrostatic loading because pressure changes cause axial fiber displacement only through Poisson strain, or strain perpendicular to loading (Lindsey et al., 2019).

Distributed Acoustic Sensing (DAS) has advantages over other tools for the purpose of EGS monitoring, such as its low cost, ability to withstand extreme subsurface conditions such as high temperatures and pressures, positioning versatility, and long-term viability (Lellouch et al., 2020). DAS exceeds the temperature and pressure limits of traditional methods, such as conventional electric pressure sensors, as it can operate under geothermal reservoir conditions, temperatures and pressures exceeding 200°C and 150 MPa, respectively (Oliver et al., 2018). DAS can provide continuous measurements of strain along the entire length of a well for long periods of time, allowing for a more comprehensive understanding of hydromechanical behavior and ongoing monitoring (Oliver et al., 2018). As a fracture opens, the displacement corresponds to a region of extensional strain surrounded by a stress shadow of compressional strain (Figure 2). In the case where a fracture is near the fiber, but not intersecting the fiber, the extensional strain is broader and may be referred to as a strain front (Figure 2). Strain measured by low-frequency DAS has been applied to subsurface hydraulic continuity mapping at geothermal analog sites (Becker et al., 2020). Periodic strains of less than one nanometer/m are considered the threshold for DAS, as measured by Becker and Ciervo (2018). Becker et al. (2020) successfully located hydraulically active fracture zones within granitoid bedrock using DAS to measure oscillating strain.

2.5 Coupled Fluid Flow and Solid Deformation with Poroelasticity

Poroelasticity describes the coupling of fluid flow with solid deformation. Porous media is deformable in response to changes in stress or pore pressure (Rutqvist and Stephansson, 2003). This coupling is called a two-way coupling since changes in stress cause changes in fluid pressure and vice versa (Wang, 2000). Terzaghi's (1923) Law of Effective Stress describes this hydromechanical coupling in one dimension as:

$$\sigma_t = \sigma_e + p_f \tag{8}$$

where σ_t is total vertical stress, σ_e is effective stress, and p_f is pore fluid pressure (Rutqvist and Stephansson, 2003; Terzaghi, 1923). The effective stress refers to the frictional contact and support from the grain skeleton, the pore fluid pressure refers to the pressure of fluid in the skeleton voids, and the total stress refers to the overburden (Rogers, 2017). The Law of Effective Stress demonstrates the dynamic interplay between the three variables, total vertical stress, effective stress, and pore fluid pressure.

By modifying Terzaghi's Law of Effective Stress to three-dimensional poroelastic behavior for isotropic linear elastic porous media, Biot (1962) described the theory of poroelasticity and coupled two equations to describe the elastic response of the porous media and pore pressure, respectively:

$$\sigma_m = K\varepsilon_v + \alpha p_f \tag{9}$$

$$\xi = \alpha\varepsilon_v + \frac{1}{M}p_f = \alpha_B\varepsilon_v + S_p p_f \tag{10}$$

where $\sigma_m$is mean total stress, ξ is the increment of fluid content added or withdrawn, K is the drained bulk modulus, ε_v is the volumetric strain, α_B is the Biot-Willis' coefficient, and M is Biot's modulus, in which *1/M* is the specific storage coefficient at constant strain, S_p (Rutqvist and Stephansson, 2003; Wang, 2000). The Biot-Willis coefficient describes the portion of pore fluid pressure that counteracts the overburden (Rogers, 2017). Terzaghi's Law of Effective Stress can be modified with the Biot-Willis coefficient:

$$\sigma_m = \sigma'_m + \alpha p_f \tag{11}$$

where σ'_m is the mean effective stress (Rutqvist and Stephansson, 2003).

Poroelasticity, which focuses on the influence of fluid pressure on the mechanical behavior of porous media, is required for this study as mechanical compliance in the subsurface relates fluid pressure to DAS-measured strain (Becker et al., 2020). The lag in hydraulic response compared to strain response occurs because mechanical deformation propagates ahead of the fluid pressure in the fracture (Becker et al., 2017). The propagation of fluid pressure through fractures causes compliance to change with space and time, rather than be uniform and constant (Murdoch and Germanovich, 2012). Becker et al. (2017) experimentally supported that measured aperture dilation in fractures is linearly related to the log of fluid pressure, therefore, strain is considered a proxy for fluid pressure.

2.6 Fractured Rock Hydromechanical Behavior

The primary flow pathways in the Utah FORGE reservoir are expected to be pre-existing fractures that are hydraulically stimulated to increase their permeability (Finnila et al., 2019). Flow in fractured rocks can be analyzed simply by using a model of fluid flow through infinite parallel plates, leading to an equation known as the "Cubic Law" (Rutqvist and Stephansson, 2003). This equation describes flow rate, Q_f, in a smooth, uniform aperture planar fracture:

$$Q_f = \frac{\rho_f g b^3}{w 12\mu} \nabla h \tag{12}$$

where b is the fracture aperture, w is the fracture length, ρ_f is the density of fluid, g is the acceleration of gravity, μ is the dynamic viscosity of water, and ∇h is the head gradient (Rutqvist and Stephansson, 2003).

Fracture aperture can be related to transmissivity, T_f, in a single fracture (Rutqvist and Stephansson, 2003):

$$T_f = \frac{b^3 \rho_f g}{12\mu} \tag{13}$$

Substitution of Equation 11 into Equation 10 yields:

$$Q_x = T_f \mathrm{w} \frac{\partial h}{\partial x}. \tag{14}$$

In addition to transmissivity, Poisson's equation for Darcy flow can be written as:

$$\frac{\partial h}{\partial t} = \frac{T_f}{S_f} \nabla h = D_f \nabla h \tag{15}$$

where and S_f is fracture storativity and D_f is diffusivity (Rutqvist and Stephansson, 2003).

The coefficient of storage, or storativity, of a fracture can be determined using a reworking of the Theis equation by Jacob (1940) as:

$$S_f = \frac{1}{\rho_f A} \frac{\Delta m_f}{\Delta h} = \frac{1}{A} \frac{\Delta(\rho_f g V_f)}{\Delta P} \tag{16}$$

where A is the horizontal cross-sectional area for a column of aquifer and Δm_f is the change in water mass in the column (Rutqvist and Stephansson, 2003; Jacob, 1940).

For laminar flow in a evenly spaced natural fracture using the parallel plate model, the relationship between fracture aperture and fracture permeability can be derived from the cubic law:

$$k_{eff} = \frac{\rho_f g N b^3}{12\mu} \tag{17}$$

where N is the number of fractures per unit length perpendicular to the fracture planes (Fitts, 2013).

For a single fracture, the expression for effective permeability is then:

$$k_f = \frac{b^2}{12} \tag{18}$$

where k_f is the fracture permeability and b is the fracture aperture (Lei et al., 2021).

A hydraulically-connected system, created by distributing flow evenly over multiple fractures in EGS reservoirs, prevents thermal drawdown (Doe et al., 2014; McClure, 2009). Groundwater flow within the granite-gneiss bedrock at the FORGE site is governed by fractures, the preferred pathways of least resistance (Golder Associates, 2010) . Rock strain in response to fluid stress is influenced by these fractures that determine fluid flow, and it can therefore be used as an indicator of hydraulic connectivity (Rutqvist and Stephansson, 2003).

CHAPTER 3

SITE DESCRIPTION

3.1 Overview

The Milford, Utah Frontier Observatory for Research in Geothermal Energy (FORGE) site was selected by the U.S. Department of Energy (DOE) as a test bed to optimize Enhanced Geothermal System (EGS) technologies (Moore et al., 2019). Data collected near the Utah FORGE site provide evidence regarding the temperature, rock type, stress regime, and depth required by DOE for an EGS laboratory. In this EGS laboratory, there are two deep, deviated wells drilled to serve as an injection-production well pair. Production well 16B(78)-32 is parallel to and approximately 100 meters above injection well 16A(78)-32 (Figure 5). The DAS fiber optic cable has recently been deployed in 16B(78)-32, which was drilled to a vertical depth of 2547 m in June 2023 (May and Jones, 2023). Injection well 16A(78)-32 was drilled in January 2021 to a vertical depth of 2609 m, approximately 65° from vertical, and 105° from North (Winkler et al., 2021). The flow between the injection and production wells was and will continue to be enhanced through hydraulic fracturing (stimulation). Three zones of stimulation were created in 16A(78)-32 in April 2022, intended to create flow pathways between 16A(78)-32 and 16B(78)-32 (Figure 4).

3.2 Geology

The Utah FORGE site is located within a geologically complex region characterized by extensional faulting and high heat flow located in the Great Basin (Simmons et al., 2016) (Figure 6). Regional features include normal faults resulting from Basin and Range extension (Simmons et al., 2016). While several geothermal fields associated with regional extension are found nearby, the FORGE site is not located within the Roosevelt hydrothermal system (Simmons et al., 2016) (Figure 6). The Opal Mound fault east of the FORGE site prevents hydrothermal flow from moving westward (Simmons et al., 2016). Conductive heat transfer plays a crucial role in determining the temperature gradient, hydrothermal system, and associated hot springs found near the Opal Mound fault.

Well logs reveal the physical properties of the basin fill and bedrock in the FORGE study area (Hardwick et al., 2016). Basin fill consisting of volcanic and fluvial-lacustrine sedimentary deposits overlies granite-gneiss bedrock (Hardwick et al., 2016) (Figure 6). Tertiary granitic intrusions and Precambrian gneiss make up the crystalline basement rocks of the Milford Valley basin and can be seen at the surface in the eastward Mineral Mountains (Hardwick et al., 2016). The crystalline basement rock is a requirement of this laboratory site, as geothermal heat extraction from naturally low permeability host rocks is a focus of EGS development (Allis et al., 2016). An abundance of geologic data was available for the region surrounding the FORGE site due to contributions of geothermal exploration during the late 1970s (Hardwick et al., 2016; Simmons et al., 2016).

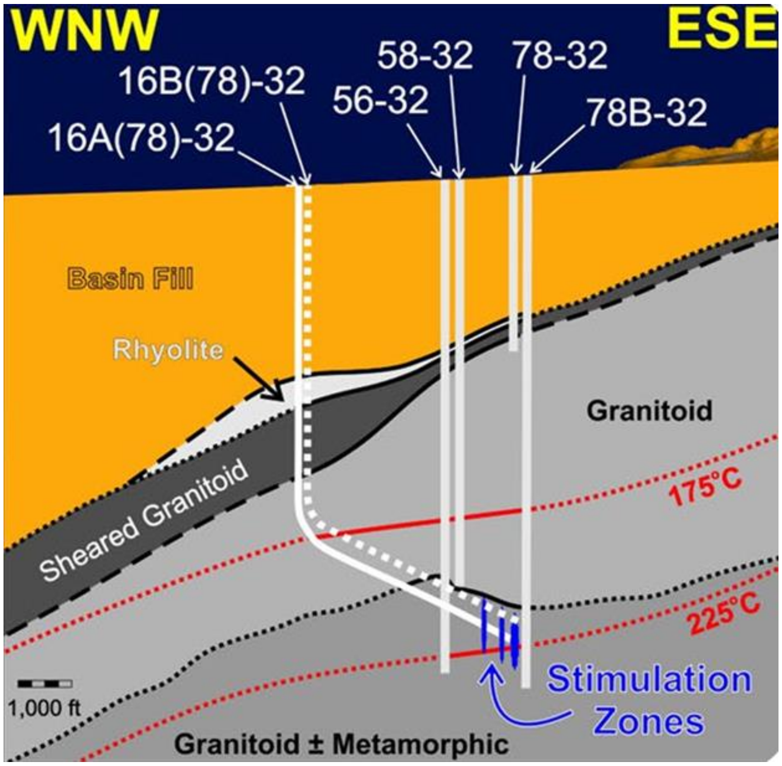

FIGURE 4. Conceptual schematic cross-section of the Utah FORGE EGS site, including wells, lithologies, temperature contours, and stimulation zones. Lithologies mapped from drilling activities. Adapted from Jones et al., 2023.

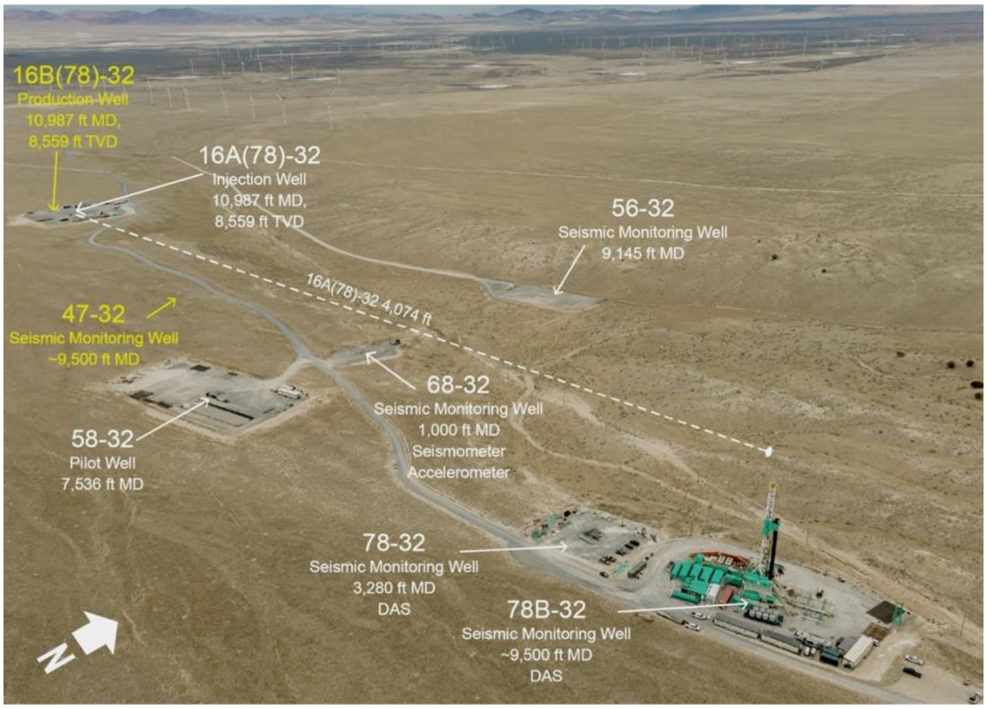

FIGURE 5. Utah FORGE site (McLennan et al., 2023). DAS will be deployed in 16B(78)-32. Water will be injected in 16A(78)-32 for the hydraulic tests.

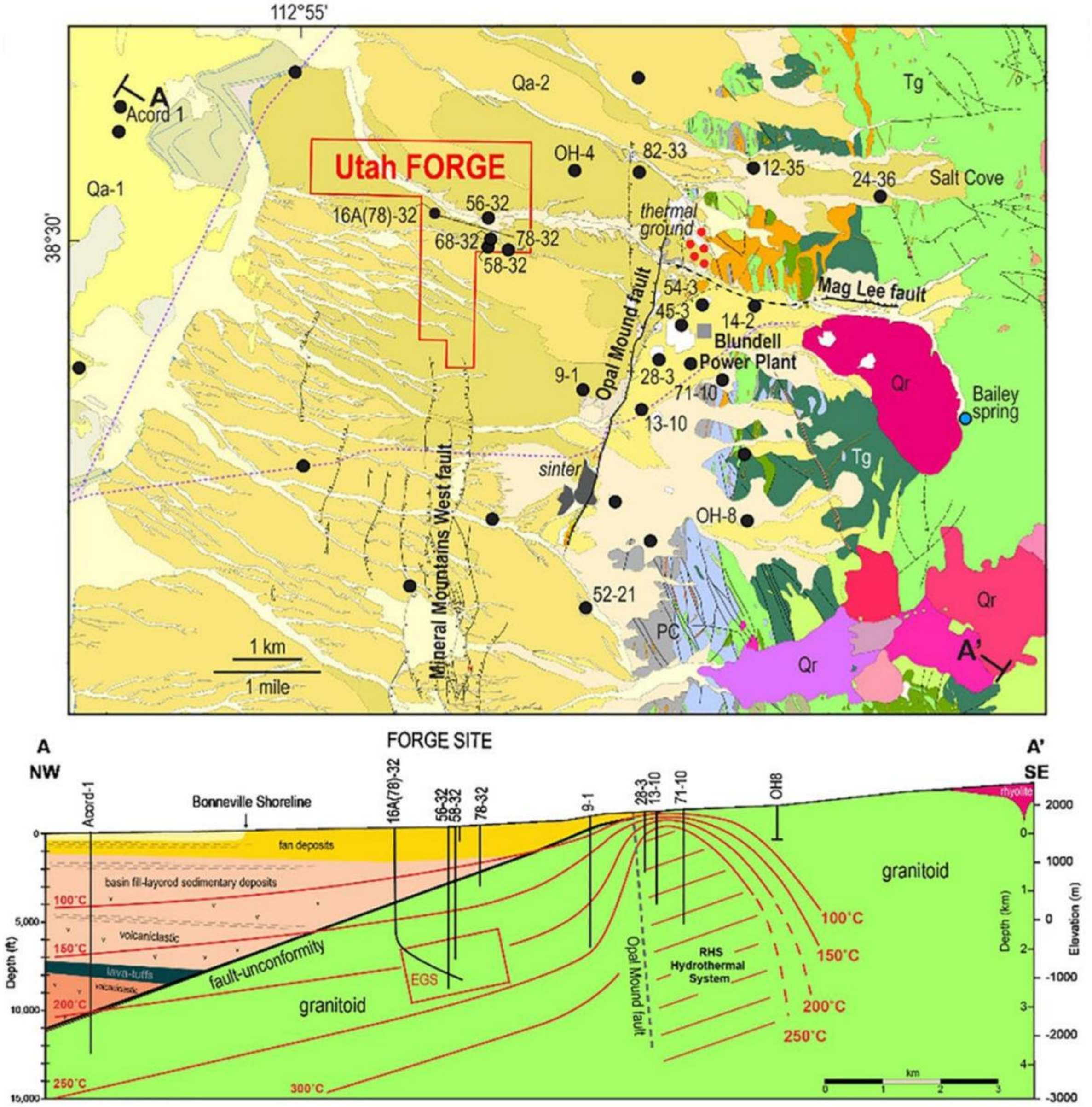

FIGURE 6. Geologic map and cross-section of the Utah FORGE EGS site. The EGS reservoir will be created in the granitoid basement rock. Abbreviations: Qa-1=Lake Bonneville silts and sands; Qa-2=alluvial fan deposits; Qr=Quaternary rhyolite lava and pyroclastic deposits; Tg=Tertiary granitoid; PC=Precambrian gneiss; black filled circles=wells. The cross-section contains temperature contours (Li et al., 2022).

CHAPTER 4

METHODS

4.1 COMSOL Hydromechanical Numerical Modeling

COMSOL 6.0 (COMSOL Inc., Burlington Massachusetts) was used for the parametric poroelastic modeling of the Utah FORGE reservoir. COMSOL is a generic finite element multiphysics simulator. COMSOL Multiphysics software is capable of supporting parametric modeling for subsurface applications, such as modeling fluid flow, solid mechanics, and heat transport. Previous work has demonstrated that COMSOL can be used to model hydraulic stimulation of natural fracture networks, such as modeling the hydromechanical behavior of deep subsurface fractured rock at the FORGE site in response to fluid injection by coupling geomechanics and fluid flow processes (Lei et al., 2021). COMSOL is flexible, well-documented, and provides sophisticated graphics for parametric modeling. This section includes equations from COMSOL documentation to describe how COMSOL solves for the model. This is explained in the Subsurface Flow and Structural Mechanics Modules User's Guides and in previous studies (Lei et al. 2021; Becker and Ciervo, 2018; Rogers, 2017). Balancing computational resources and accuracy must be considered when meshing the model, as increasing the fineness of the mesh increases both the accuracy and the time to solve.

COMSOL’s Darcy’s Law interface describes Darcy’s flow velocity field in a poroelastic medium using the pore pressure gradient, fluid viscosity, the structure of the porous medium, and gravity:

$$v = -\frac{k}{\mu}\left(\nabla p_f + p_f g\right) \tag{19}$$

where v is the Darcy’s Law fluid velocity field, k is the permeability, μ is the fluid viscosity, g is the acceleration of gravity, and p_f is the pore fluid pressure.

The Poroelasticity Interface in COMSOL couples the transient change in strain, from the Solid Mechanics Interface, with the Darcy's Law Interface that describes fluid flow in porous media. Coupling of the modules allows fluid pressure from the Darcy's Law interface to be a stress contribution in the Solid Mechanics interface. To describe the flow field in the poroelastic model, Darcy's Law and mass conservation are applied as:

$$\rho_f S_p \frac{\partial p_f}{\partial t} + \nabla \cdot \left(\rho_f v\right) = -\rho_f \alpha_B \frac{\partial}{\partial t} \varepsilon_v \tag{20}$$

where ρ_f is the density of the fluid, S_p is the storage coefficient, p_f is the pore fluid pressure, v is the Darcy's Law fluid velocity field, ε_v is the volumetric strain of the porous matrix, and α_B is the Biot-Willis' coefficient. The Poroelasticity interface describes the poroelastic behavior in the medium with the relationship between stress, strain, and pore pressure (Rogers, 2017):

$$\sigma = C\varepsilon - \alpha_B p_f I \tag{21}$$

where σ is the total stress tensor, ε is the total strain, and **C** is the elasticity matrix. Using Biot's theory, the increment in fluid content is related to volumetric strain and pore pressure (Rogers, 2017):

$$p_f = \frac{1}{S_p}(\varsigma - \alpha_B \varepsilon_v) \tag{22}$$

where S_p is the storage coefficient, ς is the increment in fluid content, and ε_v is the volumetric strain. The storage coefficient S_p can be calculated using:

$$S_p = \theta\chi_f + \frac{\alpha_B - \theta}{K_s} = \theta\chi_f + (\alpha_B - \theta)\frac{(1-\alpha_B)}{K_d} \tag{23}$$

where θ is porosity, χ_f is fluid compressibility, K_d is the drained bulk modulus, and K_s is the solid bulk modulus. For a stiff porous matrix, $\alpha_B \approx \theta$ can be considered. This is used to define and simplify the lower bound of the poroelastic storage model in COMSOL to be the fluid compressibility:

$$S_p \approx \theta \chi_f. \tag{24}$$

COMSOL uses a governing equation for poroelastic modeling to describe changes in the stress tensor and porous matrix displacement related to changes in pore pressure, described as:

$$-\nabla \cdot \sigma = \rho g \tag{25}$$

where σ is the stress tensor and ρ is the average total density. With the Solid Mechanics interface, COMSOL solves the stress tensor for the isotropic porous material under plane strain:

$$\begin{bmatrix} \sigma_{xx} \\ \sigma_{yy} \\ \sigma_{zz} \end{bmatrix} = \frac{E}{(1+v)(1-2v)} \begin{bmatrix} 1-v & v & 0 \\ v & 1-v & 0 \\ 0 & 0 & 1-2v \end{bmatrix} \begin{bmatrix} \varepsilon_{xx} \\ \varepsilon_{yy} \\ \varepsilon_{zz} \end{bmatrix} - \begin{bmatrix} \alpha_B p & 0 & 0 \\ 0 & \alpha_B p & 0 \\ 0 & 0 & \alpha_B p \end{bmatrix} \tag{26}$$

Here, E is Young's modulus and v is Poisson's ratio. Porous matrix displacement is related to normal and shear strains by:

$$\varepsilon_{xx} = \frac{\partial u}{\partial x} \quad \varepsilon_{yy} = \frac{\partial v}{\partial y} \quad \varepsilon_{xy} = \frac{1}{2}\left(\frac{\partial u}{\partial y} + \frac{\partial v}{\partial x}\right) \quad \varepsilon_{xy} = \varepsilon_{yx} \;\; \varepsilon_{xz} = \varepsilon_{yz} = 0. \tag{27}$$

To couple porous matrix deformation and fluid flow, the final poroelastic equation is related to poroelastic changes in pore pressure and displacement (Rogers, 2017) using:

$$-\nabla \cdot \sigma = -\nabla \cdot \left(C\varepsilon - \alpha p_f I\right) = \rho g = \left(\rho_f \theta + (1-\theta)\rho_s\right) g \tag{28}$$

and

$$S_p \frac{\delta p_f}{\delta t} + \nabla \cdot \left[-\frac{k}{\mu_f}\left(\nabla p_f - \rho_f g \nabla d\right)\right] = -\alpha \frac{\delta \varepsilon_{vol}}{\delta t} \tag{29}$$

where σ is the stress tensor, θ is porosity, ρ is the average total density, ρ_f is the density of the fluid, and ρ_s is the density of the solid (Rogers, 2017).

The Fracture Flow Interface within the Darcy's Law module uses tangential derivatives to solve for the flow within the fracture boundaries in the porous model. The expression is:

$$q_f = -\frac{k_f}{\mu} b(\nabla_T p + \rho g \nabla_T d) \tag{30}$$

where q_f is the volumetric flow rater per unit fracture length, k_f is the fracture permeability, μ is the fluid dynamic viscosity, b is the fracture aperture, p is the pressure, ρ is the fluid density, and d is the depth. The cubic law is used to determine the fracture permeability (k_f) from the fracture aperture using the aforementioned expression:

$$k_f = \frac{b^2}{12 f_f} \tag{31}$$

where b is the fracture aperture and f_f is the roughness factor. The Fracture Flow Interface solves for pressure using the flow equation and porous material properties as:

$$d_f \frac{\partial}{\partial t}(\varepsilon_f \rho) + \nabla_T \cdot (\rho q_f) = d_f Q_m \tag{32}$$

where ε_f is the fracture porosity and Q_m is the mass source term.

COMSOL's thin elastic layer node can be used to model fracture zones. This feature decouples the displacements within the fracture boundary and connects them by elastic and viscous forces to mimic the behavior of the thin layer without explicit meshing of the thickness (Kumar, 2013). The fractures are described as thin elastic layers, with the fracture aperture, Young's Modulus, and Poisson's Ratio give the normal stiffness of the fractures (k_n), using:

$$k_n = \frac{E(1-v)}{b(1+v)(1-2v)} \tag{33}$$

where E is Young's Modulus, v is Poisson's ratio, and b is the fracture aperture (Gudala et al., 2023).

4.2 Modeling Strain Signatures as an Indicator of Fracture Connectivity

4.2.1 Numerical Model Setup

A three-dimensional numerical model of DAS strain in the Utah FORGE reservoir was developed in COMSOL® Multiphysics version 6.0 (Figure 7). COMSOL uses the governing equations as described in Chapter 4.1 to solve for the hydromechanics, including pressure and displacement, in the model. Both complete and near-miss fractures were simulated in this study using a hydromechanical discrete fracture network (DFN) model. In this part of the study, we will refer to the primary model as Model A, and variations in the DFN of Model A will be referred to as Models B, C, and D. The fracture orientations were derived from the Utah FORGE Phase 2C Topical Report (Energy and Geoscience Institute at the University of Utah, 2019) for this section of the study, while the distribution of fractures was randomized by COMSOL's DFN add-in. Expected DAS response to these simulations was achieved by post-processing the strain data in MATLAB. The modeling workflow developed in this study may be used for DAS hydraulic tests at EGS reservoirs at FORGE and elsewhere. The workflow to model the FORGE reservoir and simulate DAS response to the hydraulic test was divided into five components: (1) setting up the hydromechanical model of the FORGE reservoir, (2) creating the fracture network, (3) defining FORGE granitoid parameters, (4) simulating the hydraulic test with a time-dependent study, and (5) post-processing strain data in MATLAB.

A hydromechanical model was constructed in COMSOL by coupling Solid Mechanics and Darcy's Law interfaces with the Poroelasticity multiphysics node. The model was created based on COMSOL documentation and workflows from COMSOL's Application Gallery. Specific examples from COMSOL's Application Gallery used to design this model included *Biot Poroelasticity*, *Geothermal Doublet*, and *Flow in a Fractured Reservoir*. The geometry of the block model reservoir and all interior components were built in COMSOL via *Component* > *Geometry.* The Discrete Fracture Network - 3D add-in was used to simulate the stimulated fractures, which contribute to the *Geometry* section. The model simulated injection well 16A(78)-32 and production well 16B(78)-32, which were connected by fractures within the granitoid basement at FORGE. The wells were defined as edges in the *Geometry* section, wherein edges are essentially lines connecting vertices. In the *Geometry* section, the wells were rotated to account for the block's orientation in space relative to the principal stress directions. The principal stress directions are necessary to control how fractures open and close with fluid pressure propagation. To unite the geometry for meshing and analysis, the final step in the *Geometry* section was the *Form Union* node.

Input parameters were derived from FORGE collaboration publications (Table 2). Water properties corresponded to estimated average reservoir conditions at 200°C and 20.7 MPa (Xing et al., 2022a).

TABLE 2. Input Parameters for the FORGE EGS Simulation in COMSOL

Parameter	**Value**	**Reference**
Young's Modulus	54.5 GPa	(Ghassemi and Kumar, 2023)
Poisson's Ratio	0.29	(Ghassemi and Kumar, 2023)
Biot Coefficient	0.69	(Ratnayake and Ghassemi, 2023a)
Porosity	0.01	(Lee and Ghassemi, 2022)
Fracture Porosity	0.5	(Nadimi et al., 2020)
Matrix Permeability	4.44E-17 m^2	(Ratnayake and Ghassemi, 2023a)
Density of Granitoid	2670 kg/m^3	(Xing et al., 2022b)
Maximum Horizontal Stress Gradient	0.0218 MPa/m	(Ghassemi and Kumar, 2023)
Minimum Horizontal Stress Gradient	0.0165 MPa/m	(Ghassemi and Kumar, 2023)
Vertical Stress Gradient	0.0256 MPa/m	(Ghassemi and Kumar, 2023)
Density of Water at Reservoir Conditions	878 kg/m^3	(Xing et al., 2022a)
Viscosity of Water at Reservoir Conditions	1.5E-4 Pa-s	(Xing et al., 2022a)
Compressibility of Water at Reservoir Conditions	8.7E-10 1/Pa	(Xing et al., 2022a)

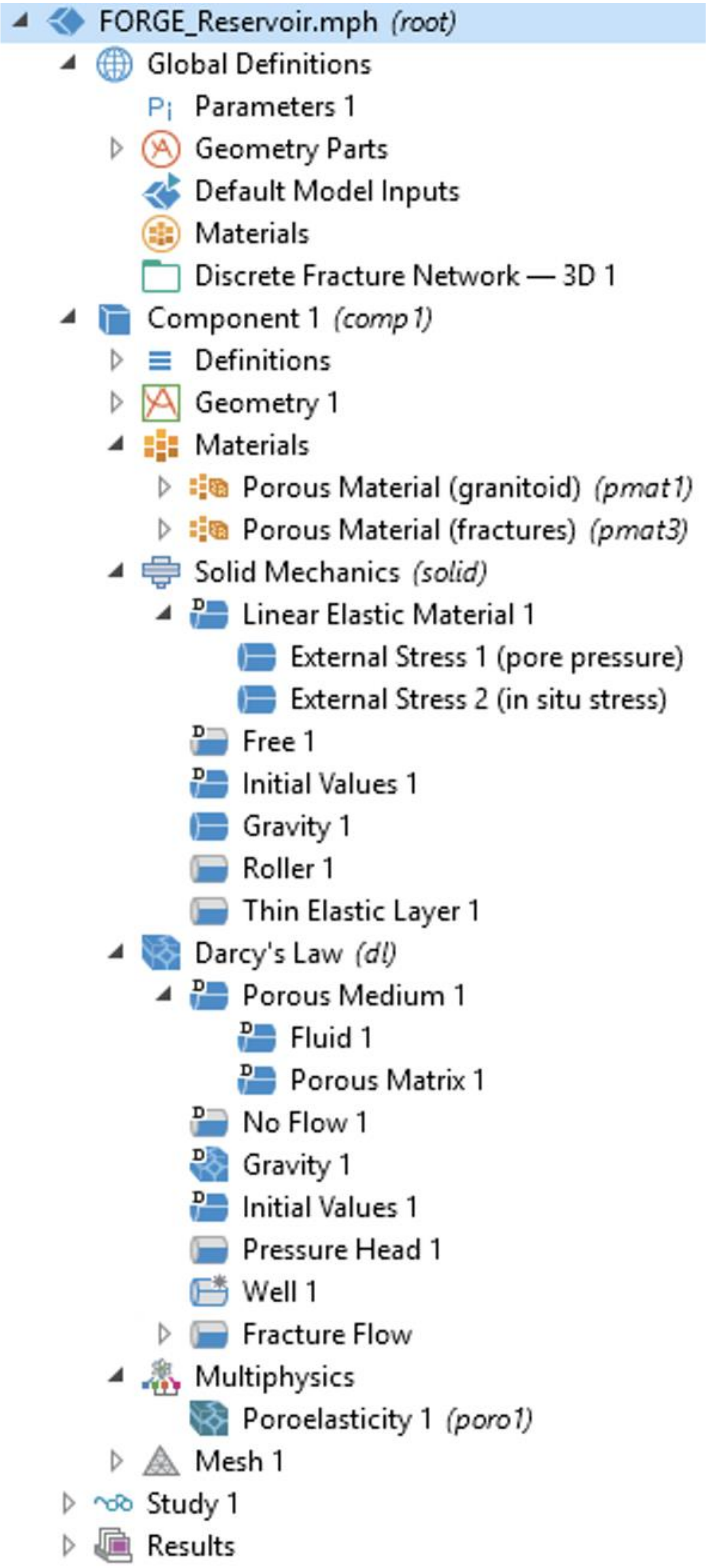

- FORGE_Reservoir.mph *(root)*
  - Global Definitions
    - Parameters 1
    - Geometry Parts
    - Default Model Inputs
    - Materials
    - Discrete Fracture Network — 3D 1
  - Component 1 *(comp1)*
    - Definitions
    - Geometry 1
    - Materials
      - Porous Material (granitoid) *(pmat1)*
      - Porous Material (fractures) *(pmat3)*
    - Solid Mechanics *(solid)*
      - Linear Elastic Material 1
        - External Stress 1 (pore pressure)
        - External Stress 2 (in situ stress)
      - Free 1
      - Initial Values 1
      - Gravity 1
      - Roller 1
      - Thin Elastic Layer 1
    - Darcy's Law *(dl)*
      - Porous Medium 1
        - Fluid 1
        - Porous Matrix 1
      - No Flow 1
      - Gravity 1
      - Initial Values 1
      - Pressure Head 1
      - Well 1
      - Fracture Flow
    - Multiphysics
      - Poroelasticity 1 *(poro1)*
    - Mesh 1
  - Study 1
  - Results

FIGURE 7. COMSOL model build for Models A, B, C, and D of the FORGE simulations.

In the Solid Mechanics interface, the simplified subsurface block model of the granitoid basement was described as an isotropic linear elastic material via *Component > Solid Mechanics > Material Models > Linear Elastic Material* because the properties of the granitoid are the same in all directions. The Structural Transient Behavior was set to Quasistatic, as required by the Poroelasticity interface in which a transient formulation of Darcy's law is combined with a quasistatic formulation of Solid Mechanics (COMSOL, 2021). In the linear elastic material node, elastic properties of Young's Modulus and Poisson's Ratio were specified to describe the stiffness of the porous material and deformation perpendicular to loading. In-situ stress gradients and pore pressure values derived from the Darcy-flow interface were applied to the block using the Linear Elastic Material External Stress node via *Component > Solid Mechanics > Linear Elastic Material > External Stress*. For one external stress, the stress input was described as pore pressure with absolute pressure corresponding to the pressure value derived from the Darcy-flow interface, *p*, and the Biot-Willis coefficient was defined. For another external stress, the stress input was described as in-situ stress in which the diagonal in situ stress tensor was defined by a function of the principal stress gradient and the depth (Table 3). The maximum and minimum horizontal stress orientations were 30° and 120° respectively relative to north at Utah FORGE as described in Lee and Ghassemi (2022). The block was rotated so that in-situ stresses were aligned with the x- and y-axes, in which the maximum horizontal stress was applied in the y-direction. Gravity was applied to the domain via the *Gravity* node. All block boundaries were free to move only in the tangential direction via the *Roller* node. To model the flexibility of the fracture zone, fractures were represented as thin elastic layers by adding the section *Component > Solid Mechanics > Mass, Spring, and Damper > Thin Elastic Layer*. The fracture material data including Young’s modulus, Poisson’s ratio, and aperture thickness were applied to this node. Fracture permeability is related to aperture as modeled by the cubic law.

TABLE 3. In-Situ Stress Tensor Input as a Function of Stress Gradient and Depth

X_stress*z	0	0
0	Y_stress*z	0
0	0	Z_stress*z

The Darcy’s Law interface was applied to describe the block as an isotropic porous medium via *Component > Darcy’s Law > Porous Medium*. The Darcian Flow model was applied, prescribing a linear pressure-velocity relationship, and the poroelastic storage model was applied to the porous medium. In *Component > Darcy’s Law > Fluid,* the fluid properties were defined from the parameters defined in the fluid material node, including density, dynamic viscosity, and compressibility. In *Component > Darcy’s Law > Porous Matrix,* the matrix properties were defined including porosity and isotropic permeability. All block boundaries were set to initial hydrostatic pressure head gradient via the *Initial Values* node, and gravity was applied to the domain via the *Gravity* node. The pressure head boundary condition was also applied to all block boundaries via the *Pressure Head* node.

Two wells were simulated within the block, an injection well with mass flow rate specified and a production well used only to measure response to injection (Figure 8). The injection well was defined in the model via *Component > Darcy’s Law > Fluid > Edges > Well.* The production well, 16B, was positioned 100 m above and parallel to the injection well (Lee and Ghassemi, 2022). In this simulation, it served only as a trajectory for the DAS cable, i.e. flow was not permitted to the production well. Well 16A(78)-32 was drilled approximately 65° from vertical and 105° from North, so both wells in the model were oriented in that direction and adjusted for the in-situ stress rotation in the *Geometry* section (Winkler et al., 2021) (Figure 9). The maximum horizontal stress was oriented at N30°E, as estimated by FMI logs at Utah FORGE (Lee and Ghassemi, 2022; Moore et al., 2020). For the scenario presented here, injection was specified only along a 10 cm segment at which a fracture intersected for the purpose of constraining flow primarily to the single fracture intersection (see fracture network description below).

To define fracture flow within the fracture geometries in the porous medium all fractures were selected under *Component > Darcy's Law > Fracture Flow*. Fracture properties applied in this section included the aperture, cubic law permeability model, and material parameters. The permeability in the DFN was many orders of magnitude larger than the rock matrix, so flow was almost entirely through fractures.

The Poroelasticity interface coupled fluid flow with solid deformation defined in the Solid Mechanics and Darcy's Law physics interfaces under *Component > Multiphysics > Poroelasticity*. This coupling allowed the solid to respond to changes in flow conditions over time. The Biot's effective stress coefficient was specified to describe the distribution of external stress between pore fluid and porous matrix.

To retrieve the axial strain along the simulated DAS fiber, the strain tensor matrix was transformed based on a rotated coordinate system aligned with the well/DAS trajectory. A rotated coordinate system was constructed since the simulated fiber was oriented within the block model corresponding to the drilling angle of 65 degrees. The rotated coordinate system was also transformed to fit the block model that was rotated for principal stress directions (Figure 10). The rotated system was constructed under *Definitions > Coordinate Systems > Rotated Systems*. Euler angles were entered to rotate the coordinate system to align *x* with the length of the simulated fiber (Table 4). The matrix transform was applied under *Definitions > Variable Utilities > Matrix Transform*. The production well edge was the geometric entity selected and the input was the strain tensor with symmetric matrix format (Table 5). The output coordinate system selected was the rotated system.

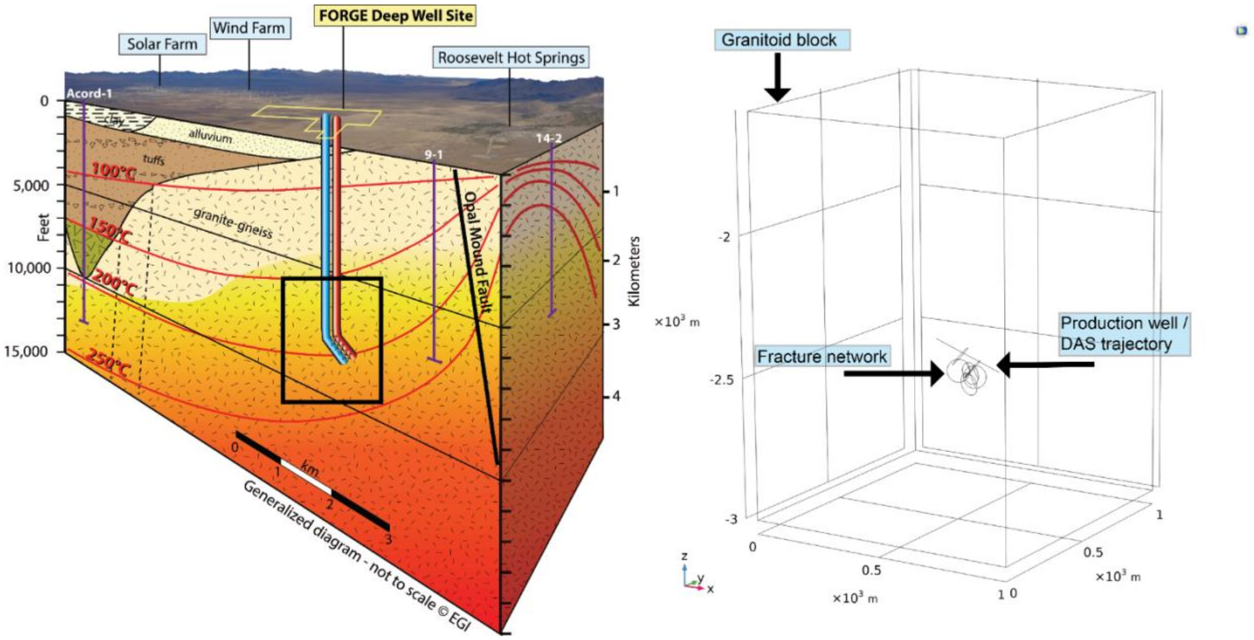

FIGURE 8. Granitoid reservoir at FORGE as modeled in COMSOL (Energy & Geoscience Institute). The Model A DFN is depicted, containing six fractures. Only a subset of the expected fractures was modeled here.

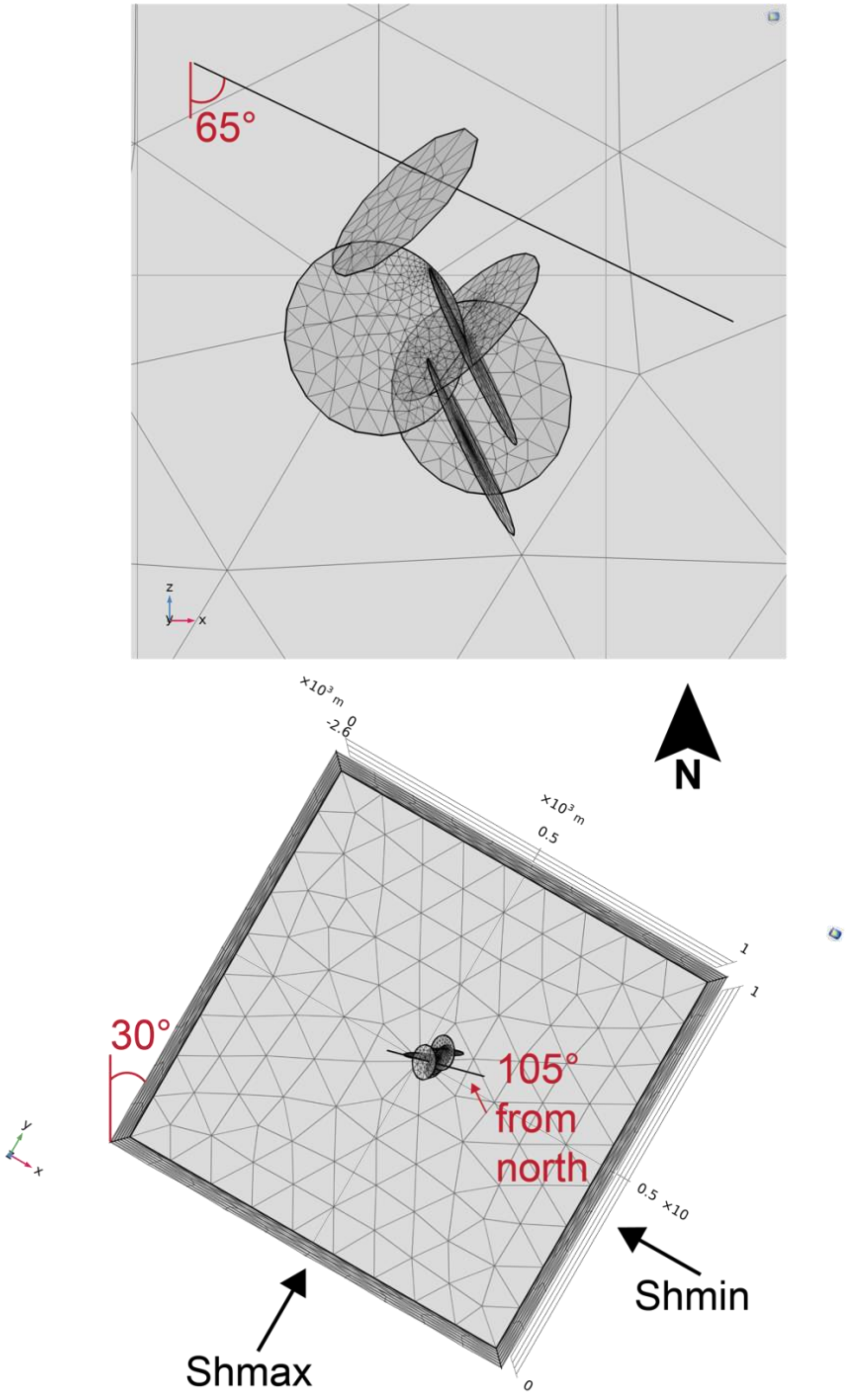

FIGURE 9. Model rotation with respect to principal stress directions. The model is rotated with respect to North to align the x- and y- axes with the maximum horizontal stress (S_{hmin}) and minimum horizontal stress (S_{Hmax}). The production well is expected to follow the injection well trajectory, which was drilled 65° from vertical and 105° from North (Model A depicted).

The orientations of the simulated fracture network were adopted from the Utah FORGE Phase 2C Report, Section B Results II (Energy and Geoscience Institute at the University of Utah, 2019) (Table 6). These orientations were adjusted to align with the rotated coordinate system. Both wells in the model were connected by a six-fracture network generated by the 3D Discrete Fracture Network add-in constrained to a bounding box to represent a region of stimulated fractures (Figure 11). A 250 m segment of the production well was simulated, with distance along the well increasing with depth from the origin to the toe (Figure 11). The DFN was simple and tightly constrained for the purposes of this study. To focus on identifying and distinguishing the strain signatures of near-miss fractures from hydraulically connected fractures, the apertures, sizes, and orientations for all 6 fractures were constant. Positions were randomly distributed, but it was required that there be at least one intersecting fracture and one near-miss fracture. The cubic-law permeability model was applied to all fractures, which have an initial aperture of 0.1 mm or about 900 darcy.

To demonstrate that near-miss fractures can be identified under multiple geologic scenarios, DFN geometry variations were simulated. The injection rate and period were the same as the base simulation, with a mass flow rate of 0.1 kg/s and a 60-minute period. In addition to the first model (Model A), three more models were built with variations in geometry and connectivity (Figure 12). Model B contained one intersecting fracture and two near-miss fractures with one near-miss fracture located closer and more hydraulicly connected to the injection well compared to the other near-miss, which also approached the production well at a more severe angle. Model C contained one intersecting and one-near miss fracture, similar to the original model. However, compared to the original model, the intersecting fracture was located closer to the injection source and the near-miss fracture was located farther. The last geometry variation, Model D, also contained one intersecting fracture and one-near miss fracture, of which both fractures were located closer to each other and farther from the injection source.

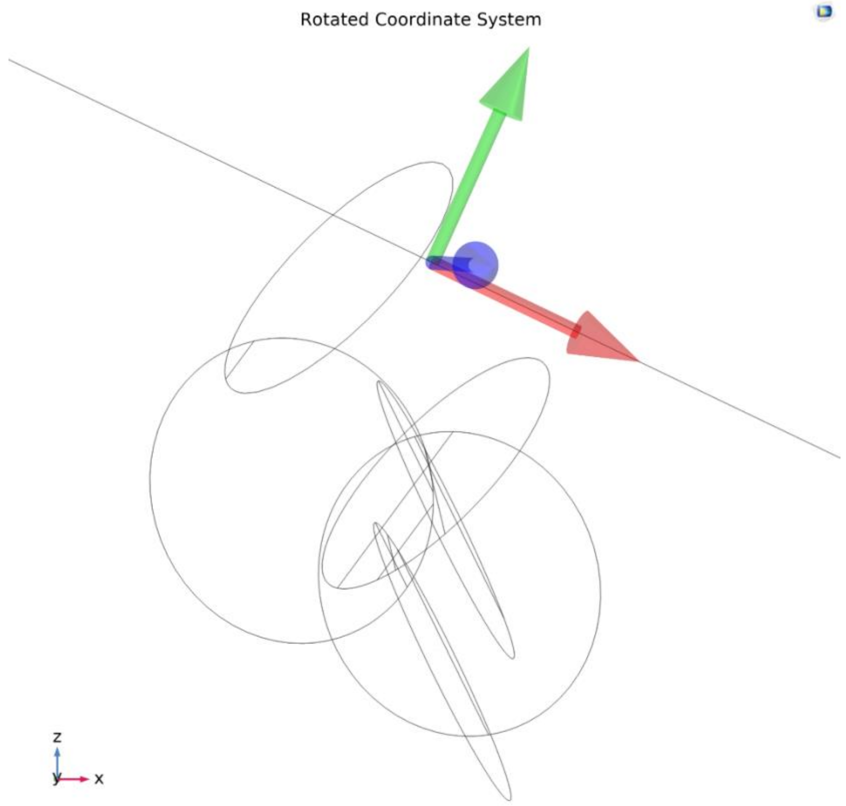

FIGURE 10. Rotated coordinate system in COMSOL to align the x-axis, in red, with the production well/DAS trajectory (grey line) for strain analysis (Model A depicted).

TABLE 4. Euler Angles to Rotate the Coordinate System to Align the X-direction with the Length of the Simulated Fiber

Euler angles (Z-X-Z) (radians)
0.2618
1.5708
-0.43633

TABLE 5. Matrix Transform Settings for the Strain Tensor to Measure Strain in the Rotated Coordinate System

	X	Y	Z
X	solid.eXX	solid.eXY	solid.eXZ
Y	solid.eXY	solid.eYY	solid.eYZ
Z	solid.eXZ	solid.eYZ	solid.eXX

TABLE 6. Fracture Set Orientations from Utah FORGE Used to Generate the DFN (Energy and Geoscience Institute at the University of Utah, 2019)

Fracture Set	Strike/Dip (degrees)
EW Vertical	96/80S
NS Inclined Dipping West	185/48W
NE Steeply Dipping SE	215/64SE

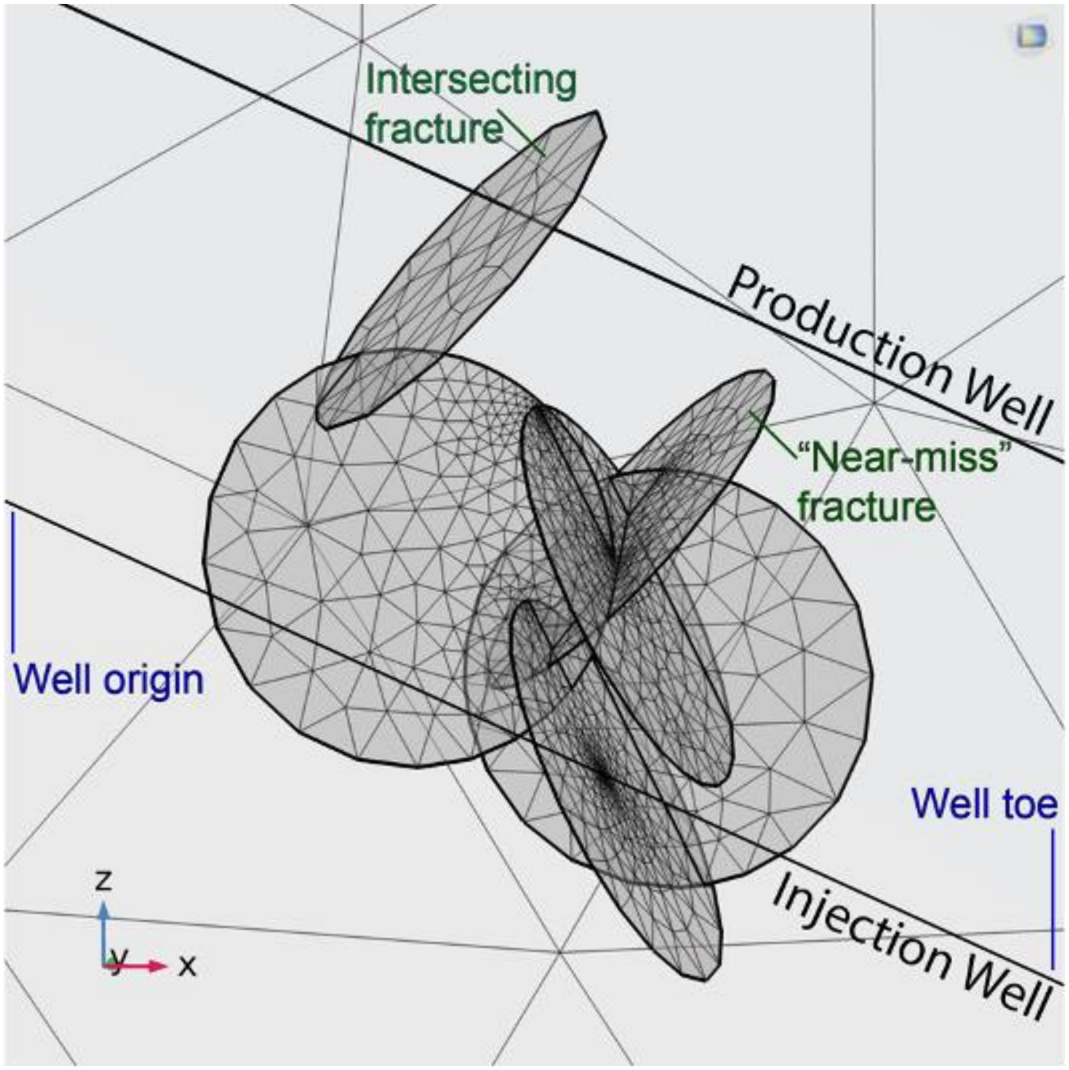

FIGURE 11. Fracture network mesh connecting Injection and Production/Observation wells consisted of a completely connected fracture and a "near-miss" fracture (Model A).

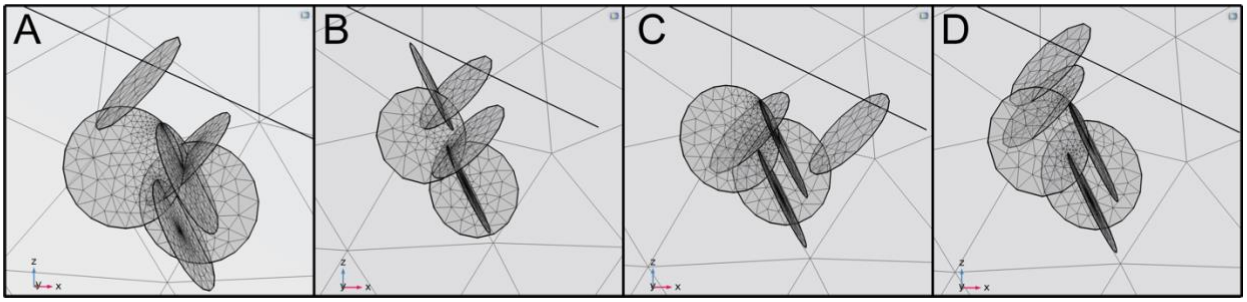

FIGURE 12. Geometry and connectivity variations of the fracture network, referred to as Models A, B, C, and D.

The model mesh was user-defined but automatically generated using *Component > Mesh*. There are nine predefined element sizes, from extremely coarse to extremely fine. Computational resources and accuracy of results must be considered when building the mesh, as increasing the fineness increases both the accuracy and the time to solve. The element size was set to Fine, but it was customized to define the minimum element size as 1 meter. A tetrahedral mesh was applied via *Component > Mesh > Free Tetrahedral*, under which additional refinements to the mesh were specified. The tetrahedral mesh was chosen as it can be used to mesh complex geometries, such as the fracture network.

4.2.2 Sinusoidal Hydraulic Test Simulations

To simulate the periodic hydraulic test, a time-dependent study was evaluated in COMSOL. The solver was defined in *Study > Step 1: Stationary* and *Study > Step 2: Time Dependent*. The stationary study required modification of the model, as the well must be disabled since it involved a time-dependent mass flow rate. The maximum step constraint was changed from the *automatic* default to *constant*, and the default constant value was used in *Study > Solver Configurations > Time-Dependent Solver*. Under *Study > Solver Configurations > Time-Dependent Solver > Fully Coupled*, the maximum number of Newton iterations was increased to 25 to prevent solver error.

The simulated periodic test involved the sinusoidal injection / withdrawal source term described in the Numerical Model Setup section. Since DAS senses strain periodically, periodic hydraulic testing was required. Injection rates and hydraulic responses were therefore sinusoidal (Figure 13). The injection well was prescribed a mass flow rate of 0.1 kg/s along the injection lateral with a period of 60 minutes. The time-dependent study was run for 90 minutes, one and a half periods, for this simulation. The sinusoidal injection mass flow rate was expressed in COMSOL as:

$$Q_m^* = Q_m \, sin\left(\frac{2\pi}{T} t\right) \tag{34}$$

where Q_m^*, Q_m, T, and t are sinusoidal injection mass flow rate, mass flow rate amplitude, period, and time, respectively. Although a perfect sinusoid hydraulic source cannot be achieved in practice, it provided a baseline evaluation of the DAS methodology.

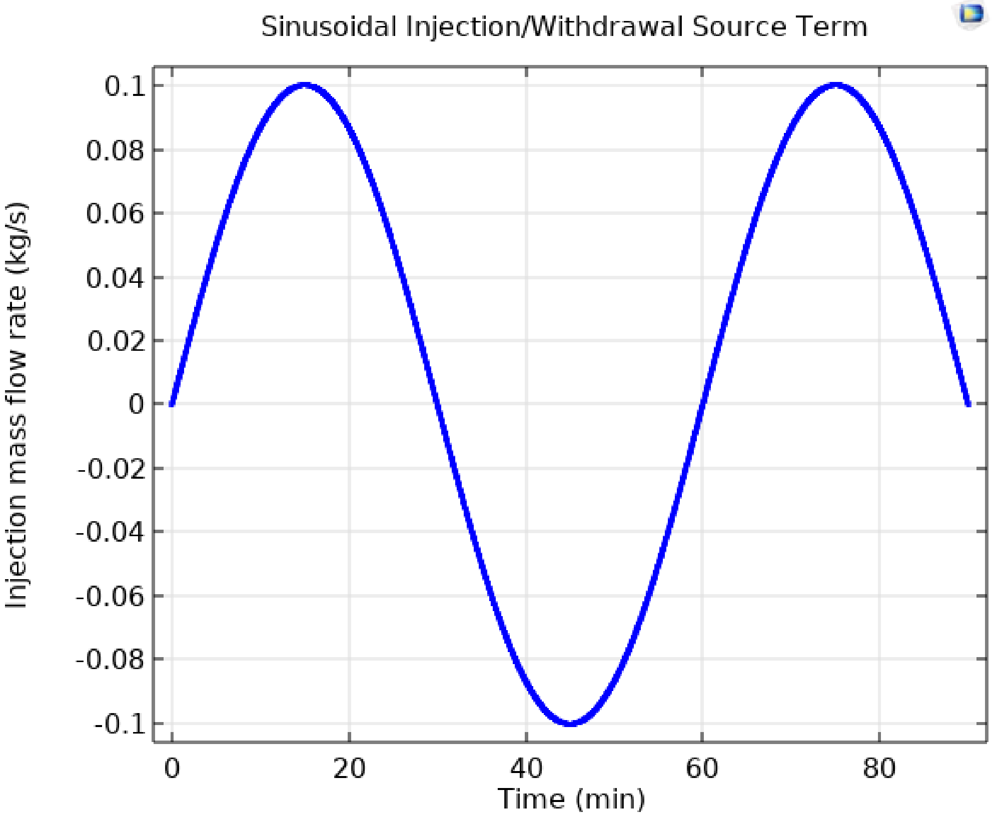

FIGURE 13. Applied sinusoidal injection/withdrawal mass flow rate.

4.2.2 Data Post-Processing

For each simulation, COMSOL output of axial strain with the corresponding arc length along the fiber was then exported for import into MATLAB. Because the fiber needed to be simulated as initially unstrained, initial strain was removed and the strain computed at each time step in MATLAB. The detrend function in MATLAB was used to subtract the straight-line fit associated with the pressure-depth gradient from the data. The derivative of that strain data was calculated to give the strain rate. Both the total strain and strain rate were plotted over the duration of the test and at specific times. Since DAS measures strain along sections of the fiber according to the gauge length instead of at individual points as COMSOL computes, the data was processed in MATLAB. The simulated gauge length was 10 m, computed as a moving average every 1 m with our MATLAB code. This simulated the limited resolution of DAS strain rate measurements due to gauge length. The original signal solved by COMSOL was plotted with the signal smoothed by gauge length for comparison.

4.2.3 Testing the Model

To verify that the model was in equilibrium with regards to fluid flow and that the hydromechanical model was fully coupled, three-dimensional analysis was performed in COMSOL. The Darcy’s velocity magnitude for the steady state condition was near zero across all outer boundaries, indicating that the fluid flow was near equilibrium (Figure 14, A). To verify that the Solid Mechanics and Darcy’s Law interfaces were coupled, the Darcy’s Law pressure was compared to the Solid Mechanics pore pressure across the entire volume. Since they were equal, the Darcy’s Law and Solid Mechanics interfaces were deemed satisfactorily coupled (Figure 14, B, C).

To verify that strain solved in COMSOL for these simulations was reasonable, strain measured along the simulated production well was compared with the results of Ratnayake and Ghassemi (2023a). Because Ratnayake and Ghassemi (2023a) will be applying the results of this study to design the tests, our test model was built to mimic their set-up solved with a 3D finite element poroelastic fracture simulator (Table 7). To calculate strain in the production well, Ratnayake and Ghassemi (2023a) used a poroelastic displacement discontinuity method that was coupled with a finite element method for fluid flow. The assumptions of Ratnayake and Ghassemi (2023a) included that the production well was 100 m above the injection well, 55 m length production well parallel to x-axis, fracture perpendicular to both wells, injection rate of 1 kg/s constrained to the point where the wellbore intersects the penny fracture, 100 m fracture diameter, 0.05 mm aperture fracture, cubic law fracture permeability, fracture porosity of 1 as fluid flows freely inside, and simulated strain measurement gauge length of 1 m.

The model was built in COMSOL to best mimic this set-up, however it was expected that the models and solutions would not be identical (Figure 15). Injection rate of 1 kg/s was constrained to a 0.015 m segment intersecting the center of a 100 m diameter penny, or disk-like, fracture. The strain for both simulations were measured as the change in strain from time 0 at the start of injection (Figure 16). Ratnayake and Ghassemi (2023a) used a negative value as tensile strain, whereas COMSOL uses a positive value for tensile strain. The results were not identical, as the simulation by Ratnayake and Ghassemi (2023a) showed no stress shadow, or compression around the tensile signal associated with the fracture opening. This difference may be attributed to a longer simulated fiber length in the model by Ratnayake and Ghassemi (2023a) compared to our COMSOL model. The regions depicting the stress shadow may be cut off in viewing window shown left in Figure 15. Other 3D poroelastic hydraulic fracture model simulations conducted by the authors depict the stress shadow (Ratnayake and Ghassemi, 2023a). The decrease in strain in Ratnayake and Ghassemi (2023a) after 80 minutes was interpreted as pushback on the dialated fracture resulting from the eventually overpowering, surrounding compressed region. Because Ratnayake and Ghassemi (2023a) used a simulator specific to fracture modelling and COMSOL is a generic simulator, differences between the results may be expected. Other explanations include the difference in numerical techniques and approximations between COMSOL and the displacement discontinuity method, meshes, boundary conditions, solver settings, and convergence criteria. The magnitude of the strain was comparable, satisfying the principal purpose of this verification. This process of testing the model was successful in terms of magnitude of strain measured at the observation well associated with injection mass flow rate into a fracture as solved by COMSOL.

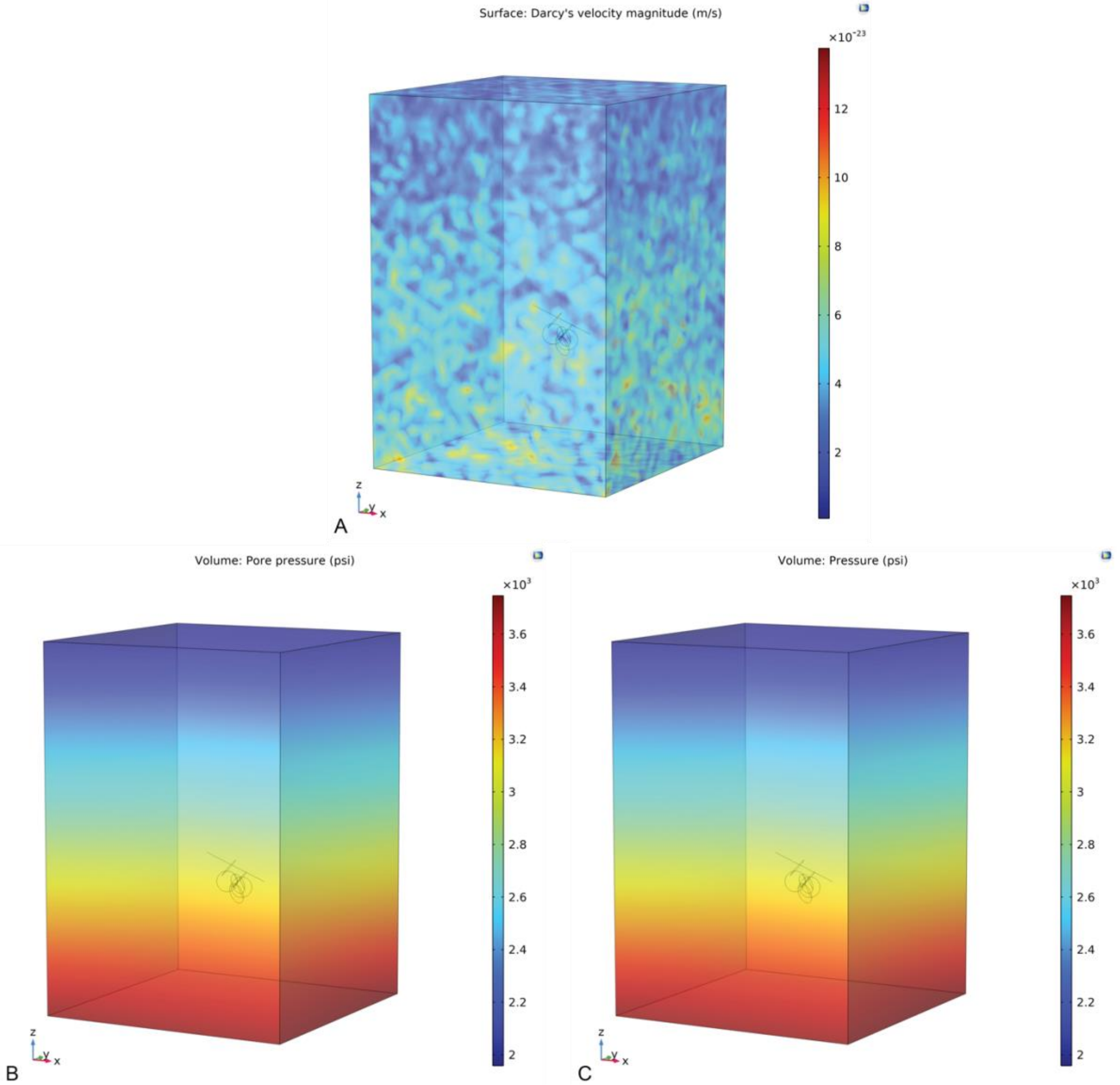

FIGURE 14. (A) Darcy's velocity magnitude at time 0, steady state. (B) Pore pressure in the Solid Mechanics interface at steady state. (C) Pressure in the Darcy's Law interface at steady state.

TABLE 7. Parameters for the Simulation in Ratnayake and Ghassemi (2023a) (top) versus Parameters for the Mimicking Model in COMSOL (bottom).

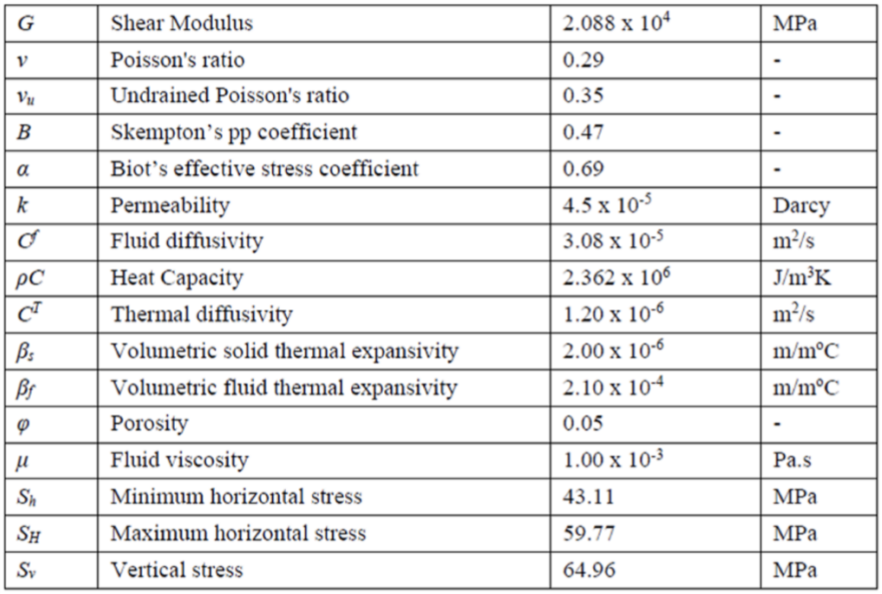

G	Shear Modulus	2.088×10^4	MPa
ν	Poisson's ratio	0.29	-
ν_u	Undrained Poisson's ratio	0.35	-
B	Skempton's pp coefficient	0.47	-
α	Biot's effective stress coefficient	0.69	-
k	Permeability	4.5×10^{-5}	Darcy
C^f	Fluid diffusivity	3.08×10^{-5}	m^2/s
ρC	Heat Capacity	2.362×10^6	J/m^3K
C^T	Thermal diffusivity	1.20×10^{-6}	m^2/s
β_s	Volumetric solid thermal expansivity	2.00×10^{-6}	m/m°C
β_f	Volumetric fluid thermal expansivity	2.10×10^{-4}	m/m°C
φ	Porosity	0.05	-
μ	Fluid viscosity	1.00×10^{-3}	Pa.s
S_h	Minimum horizontal stress	43.11	MPa
S_H	Maximum horizontal stress	59.77	MPa
S_v	Vertical stress	64.96	MPa

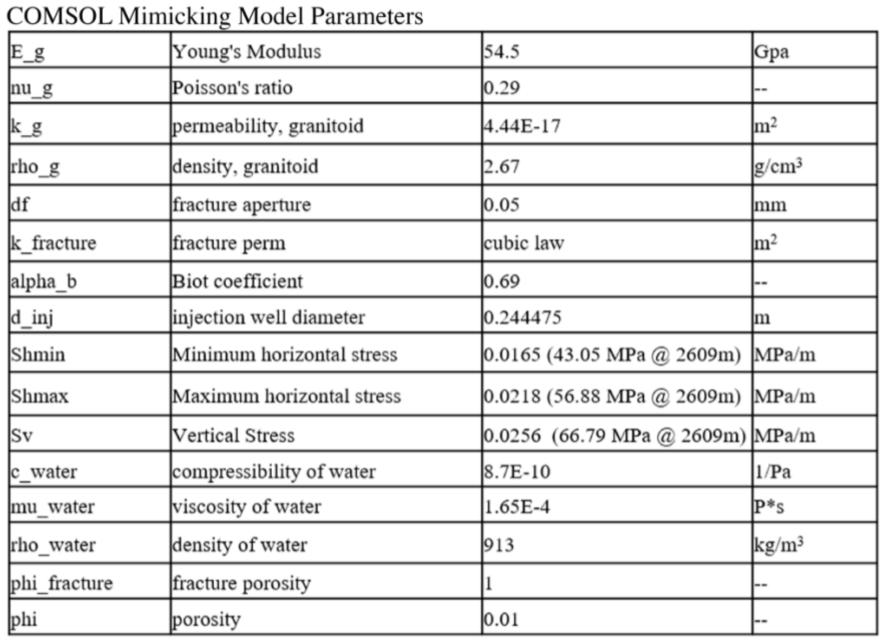

COMSOL Mimicking Model Parameters

E_g	Young's Modulus	54.5	Gpa
nu_g	Poisson's ratio	0.29	--
k_g	permeability, granitoid	4.44E-17	m^2
rho_g	density, granitoid	2.67	g/cm^3
df	fracture aperture	0.05	mm
k_fracture	fracture perm	cubic law	m^2
alpha_b	Biot coefficient	0.69	--
d_inj	injection well diameter	0.244475	m
Shmin	Minimum horizontal stress	0.0165 (43.05 MPa @ 2609m)	MPa/m
Shmax	Maximum horizontal stress	0.0218 (56.88 MPa @ 2609m)	MPa/m
Sv	Vertical Stress	0.0256 (66.79 MPa @ 2609m)	MPa/m
c_water	compressibility of water	8.7E-10	1/Pa
mu_water	viscosity of water	1.65E-4	P*s
rho_water	density of water	913	kg/m^3
phi_fracture	fracture porosity	1	--
phi	porosity	0.01	--

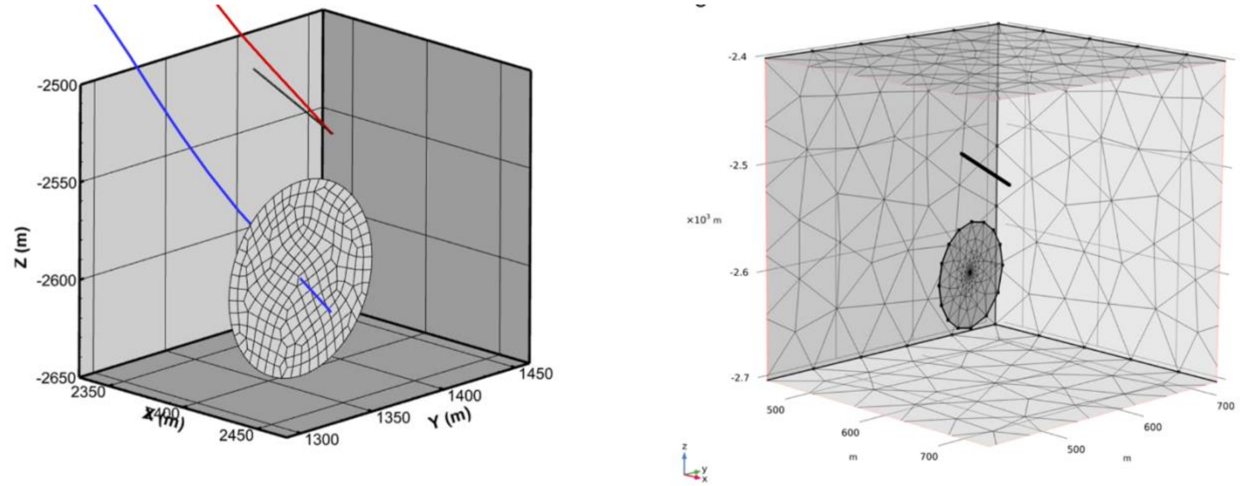

FIGURE 15. Model of the penny fracture in Ratnayake and Ghassemi (2023a) (left) versus the mimicking model in COMSOL (right).

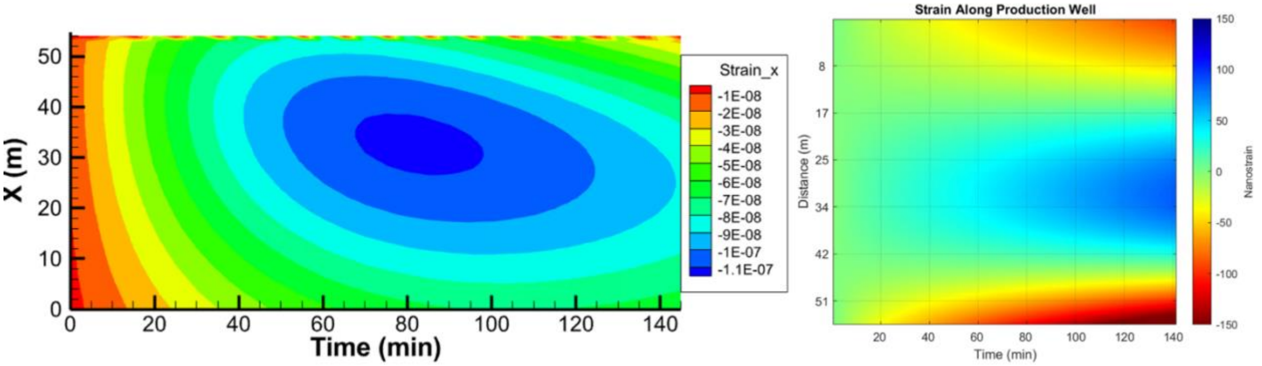

FIGURE 16. Results from Ratnayake and Ghassemi (2023a) after 140 minutes of constant rate injection (left) versus the results of the mimicking model in COMSOL (right).

4.3 Parametric Modeling for Hydraulic Test Design

4.3.1 Numerical Model Setup

A parametric sweep of ranges of fracture permeabilities, injection pressures, injection durations, and number of pulses were simulated to determine realistic expectations for the hydraulic tests to be performed at Utah FORGE. These experiments to determine hydraulic test parameter dependence will be referred to as Dependence Tests 1, 2, and 3 in this part of the study. All components of the model used in Dependence Tests 1, 2, and 3 remained identical, with the sole variation being the investigated parameters. Similar to the near-miss fracture simulations, a hydromechanical model was constructed in COMSOL by coupling Solid Mechanics and Darcy’s Law interfaces with the Poroelasticity multiphysics node. This model will be referred to as Model E. Model E was used to perform Dependence Tests 1, 2, and 3. A more complex DFN composed of a greater number of fractures and size variations was created with the Discrete Fracture Network - 3D add-in to simulate stimulated fractures more realistically, including randomized fracture sizes between 50 m and 150 m length (Table 8). The fracture orientations, sizes, and apertures were derived from FORGE by FMI log data, wells test, and modeling (Finnila et al., 2021). Because the fracture permeability is expected to change during the course of designing the hydraulic tests, fracture aperture was a varied parameter tested in the parametric sweeps. A bounding box was required to constrain the fractures to the open toe section of the well. Results using a DFN of nineteen fractures were compared to the results of the nine-fracture DFN to ensure results were consistent regardless of complexity. The nine-fracture model was preferable for time efficiency. The revised fracture set orientations from Finnila et al. (2021) were used in this simulation and prescribed proportionally as described in this study (Table 9). The random seed can be used in COMSOL to regenerate the DFN.

Model E simulated injection well 16A(78)-32 and production well 16B(78)-32 connected by the fractures within the granitoid basement at FORGE (Figure 17). Only the 61 m (200 ft) open toe section of the injection well 16A(78)-32 was simulated, as defined in the *Geometry* section. The size of the simulated production well was also reduced for meshing efficiency. The DFN was constrained to a bounding box around the open toe between 16A(78)-32 and 16B(78)-32 to simulate only fractures enhanced by stimulation. Another update was that the initial value boundary condition was changed from pressure head based on material properties to pressure with an assigned pore pressure gradient derived from McClure (2023) via *Component > Darcy's Law > Initial Values*. The pressure head node was then replaced with the pressure node, and the same pore pressure gradient value was prescribed in *Component > Darcy's Law > Pressure*. All other settings were consistent with the near-miss fracture model, with updates from FORGE literature applied (Table 10).

Under *Component > Mesh*, the mesh was further refined to account for the more complex DFN (Figure 18). The element size was set to Fine, but it was customized to define the minimum element size as 1 meter. A tetrahedral mesh was applied via *Component > Mesh > Free Tetrahedral*, under which additional refinements to the mesh were specified. The size of the well edge mesh was defined as Extremely Fine and then customized to have a maximum element size of 1 meter and minimum element size of 0.01 m. The fractures were defined as Finer and then customized to have a minimum element size of 1 m.

TABLE 8. Example of Discrete Fracture Network - 3D Settings to Generate the DFN in COMSOL. A Bounding Box was Required to Constrain the Fractures to the Open Toe Section of the Well

Setting	**Input**
Number of fractures	3
Bounding Box	Manual
Size - Width	75 m
Size - Depth	50 m
Size - Height	150 m
Corner - x	585 m
Corner - y	500 m
Corner - z	-2625 m
Distribution	Uniform random
Minimum axis length	50 m
Maximum axis length	150 m
Random Seed	91448193
Distribution	Constant
Strike	331.5
Dip	76.5
Porosity	0.01
Roughness Factor	1
Aperture distribution	Constant
Aperture	0.003 cm

TABLE 9. Fracture Set Orientations Used for Parametric Modeling Adapted from the Revised Utah FORGE DFN (Finnila et al., 2021)

Fracture Set	**Strike/Dip (degrees)**	**Quantity**	**Random Seed**
S moderately dipping W	178.5/44W	3	107697753
E steeply dipping S	91.5/76.5S	3	91448193
SSW vertical	221/85NW	2	807283444
N steeply dipping E	350/73E	1	571755355

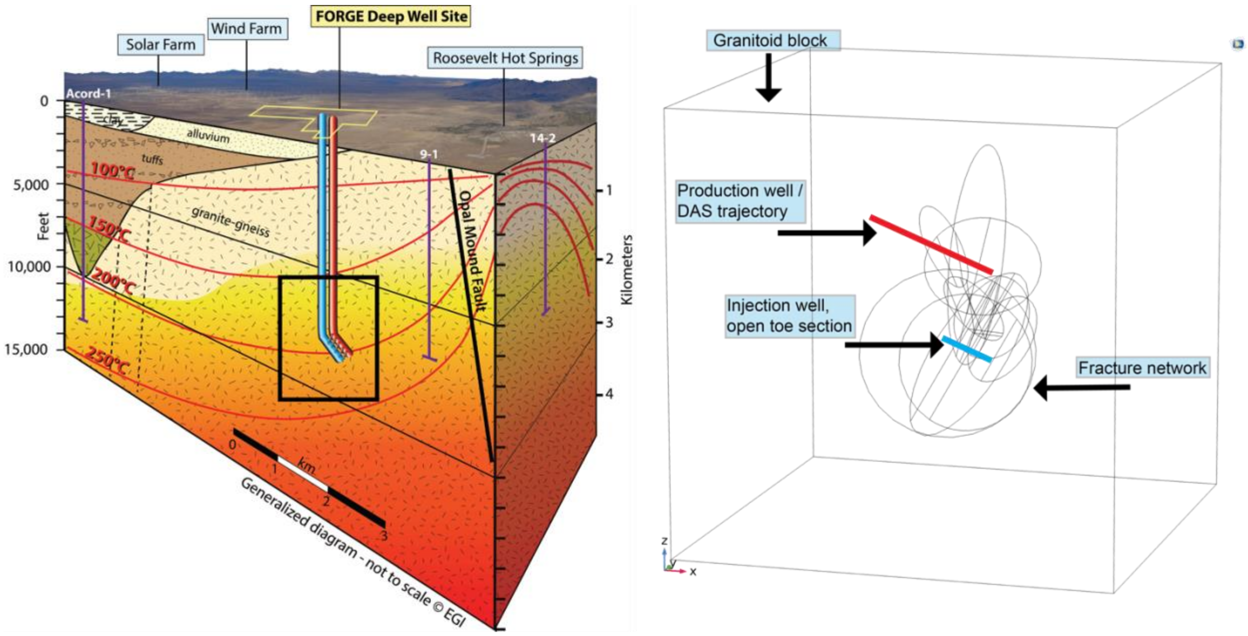

FIGURE 17. COMSOL model simulates the granitoid basement at FORGE (Energy & Geoscience Institute). Model contains a nine-fracture network. Only a subset of the expected fractures was modeled here. Injection and production well edges are thickened and colorized for clarity (Model E).

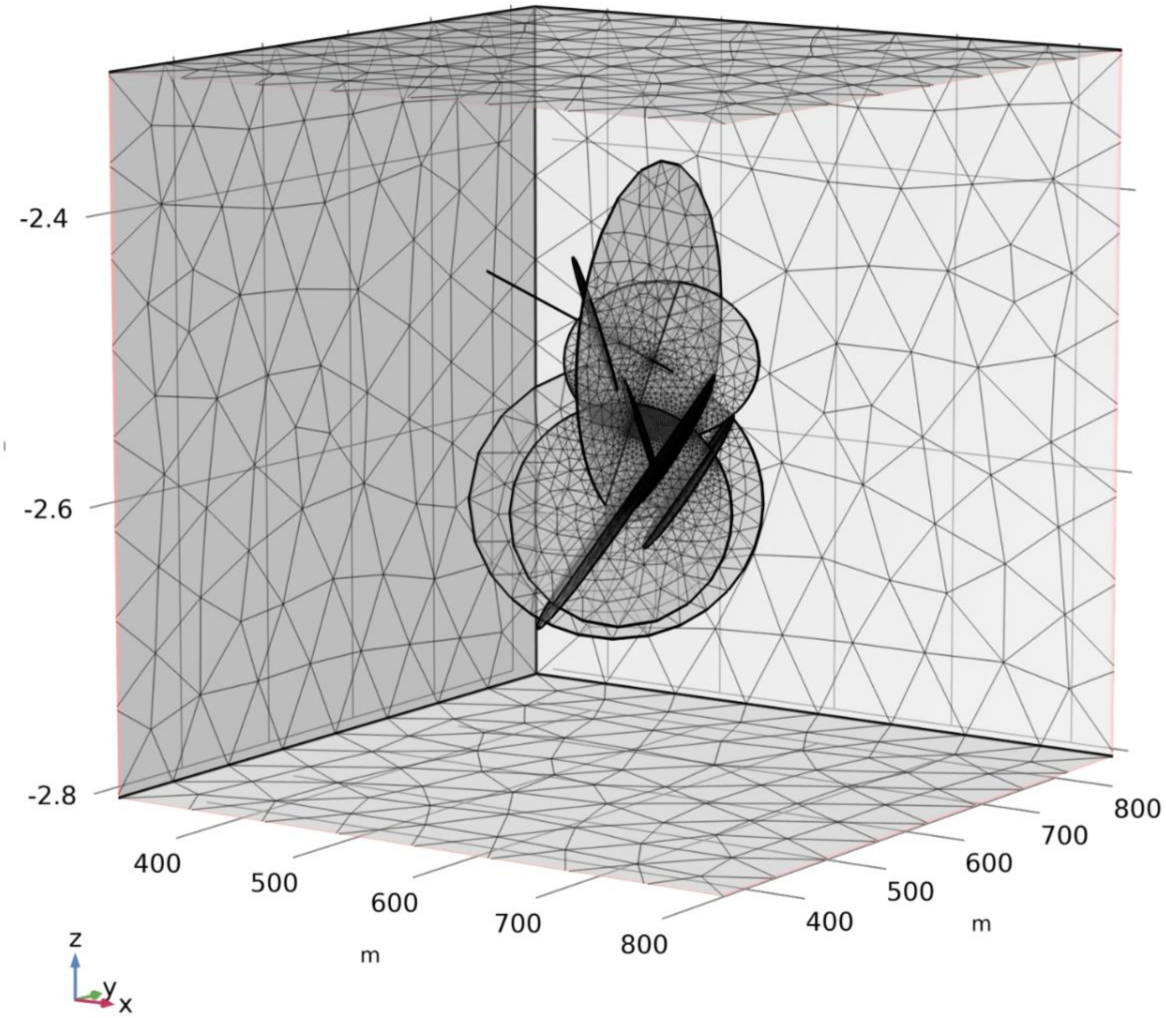

FIGURE 18. Mesh of the nine-fracture Model E used for the realistic parametric model.

TABLE 10. Input Parameters for the Realistic FORGE EGS Simulation in COMSOL (Model E)

Parameter	**Value**	**Reference**
Young's Modulus	54.5 GPa	(Ghassemi and Kumar, 2023)
Poisson's Ratio	0.29	(Ghassemi and Kumar, 2023)
Biot Coefficient	0.69	(Ratnayake and Ghassemi, 2023a)
Minimum Horizontal Stress Gradient	0.0165 MPa/m	(Ghassemi and Kumar, 2023)
Maximum Horizontal Stress Gradient	0.0218 MPa/m	(Ghassemi and Kumar, 2023)
Vertical stress gradient	0.0256 MPa/m	(Ghassemi and Kumar, 2023)
Matrix permeability	4.44E-17 m^2	(Ratnayake and Ghassemi, 2023a)
Porosity, fracture and matrix	0.01	(Lee and Ghassemi, 2022)
Density of granitoid	2670 kg/m^3	(Xing et al., 2022a)
Density of water at depth	913 kg/m^3	(Xing et al., 2022a)
Viscosity of water at depth	1.65E-4 Pa·s	(Xing et al., 2022a)
Compressibility of water at depth	8.7E-10 1/Pa	(Xing et al., 2022a)
Pore pressure gradient	0.41 psi/ft	(Mcclure, 2023)
Injection well diameter	0.1778 m	(Winkler et al., 2021)

4.3.2 Square Wave Hydraulic Test Simulations

To simulate a more realistic periodic square wave hydraulic test using Model E, a time-dependent study was evaluated in COMSOL. The simulated periodic test involved a square wave injection source term which was applied using COMSOL's rectangle function. This rectangle function was applied in the *Definitions* section in the model builder. To apply the rectangle function to simulate the square wave injection source, the *Component > Darcy's Law > Well* section was edited. Applying the square wave injection pressure was expressed as:

$$p = p_{static}[psi] + p_{inj}[psi] * rect1\left(\frac{t}{1[min]}\right) \quad (35)$$

where p_{static} was the pressure above static as measured at the toe of the injection well at 2609 m, p_{inj} was the injection pressure above static applied, and $rect1$ was the rectangle function prescribed. The square wave hydraulic signal was set to begin 20 minutes after the start of the time-dependent study. As an example, the rectangle function would be prescribed from times 20 minutes to 260 minutes to simulate a four-hour period, and, for any study time remaining, it would continue solving after injection ceased demonstrating flowback (Figure 19, Table 11). A transition zone is necessary for smoothing the injection ramp up to improve model behavior and prevent solution failure (Figure 20). The size of the transition zone corresponds to the amount of smoothing.

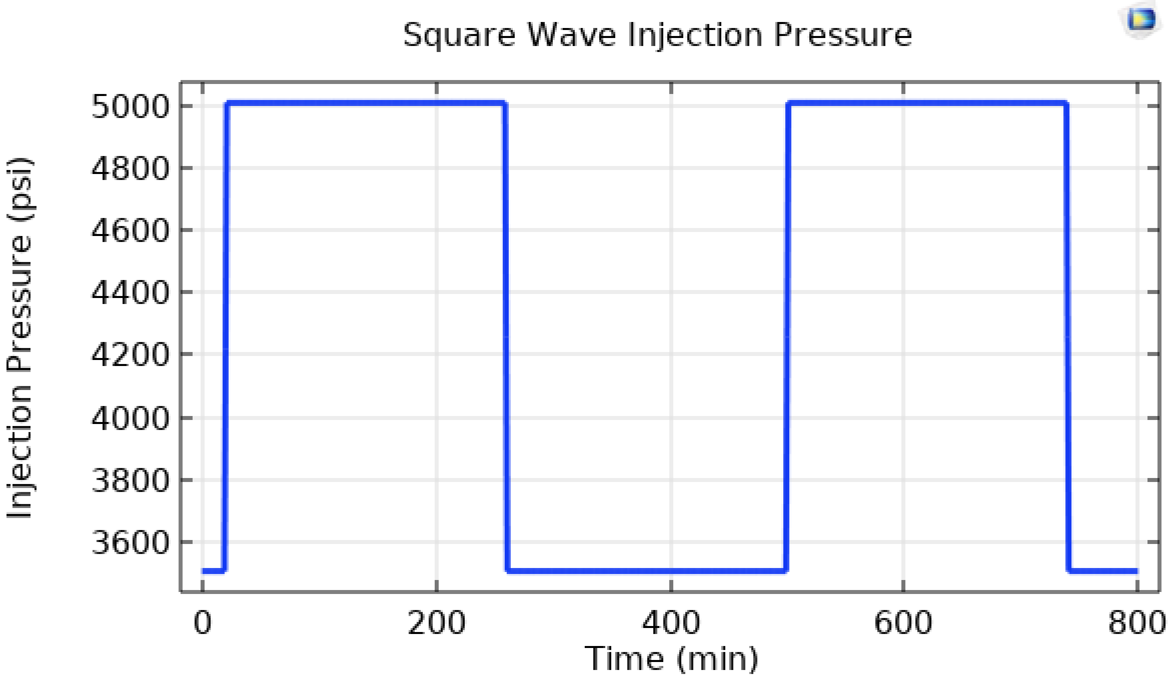

FIGURE 19. Applied square wave injection pressure for a four-hour period. (Model E)

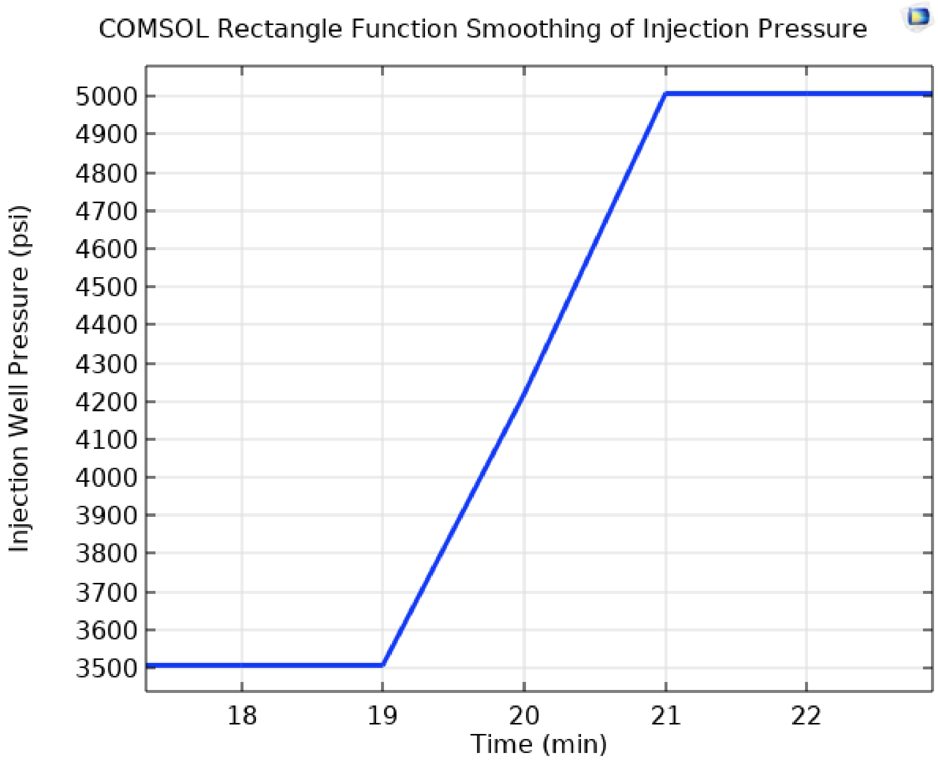

FIGURE 20. Rectangle function transition zone plot. Smoothing of square wave injection pressure for a four-hour period of 1500 psi. In this example, it took approximately two minutes to transition to peak injection pressure with the smoothing function described in Table 11 (Model E).

TABLE 11. Rectangle Function Settings for One Four-Hour Injection Period Cycle

Lower limit	20
Upper limit	260
Baseline	0
Amplitude	1
Size of transition zone	0.7
Number of continuous derivatives	2

To simulate the square wave periodic hydraulic test, a time-dependent study was evaluated in COMSOL. The solver was first defined in *Study* > *Step 1: Stationary* and *Study* > *Step 2: Time Dependent*. The stationary study required modification of the model, as the well must be disabled since it involved a time-dependent mass flow rate. The maximum step constraint was changed from the *automatic* default to *constant*, and the maximum step size was set to one minute. *Study > Solver Configurations > Time-Dependent Solver*. Under *Study > Solver Configurations > Time-Dependent Solver > Fully Coupled*, the maximum number of Newton iterations was increased to 25 to prevent solver error.

Parametric modeling was performed on a range of fracture apertures and injection pressures. A multiparametric sweep study was defined in the study node. Under *Study > Parametric Sweep*, the parameters to be included in the solution are input and the sweep type was set to *All combinations*. For the first parametric study, the variables fracture aperture and injection pressure were included (Table 12). Fracture apertures fall within the range of natural hydraulic apertures derived from data in a nearby well (Finnila et al., 2021). Permeability was computed from the cubic law relationship. All combinations of parameters were swept, totaling twelve simulations.

TABLE 12. Fracture Apertures and Injection Pressures Included in the Parametric Sweep Study (Model E)

Aperture (m)	Permeability (m^2)	Injection Pressure (psi)
3.0E-5	7.5E-11	1000
5.0E-5	2.0E-10	1500
7.5E-5	4.7E-10	2000
1.0E-4	8.3E-10	-

These simulations were run for 380 minutes, during which three one-hour period injection cycles were simulated, following a twenty-minute static period. An additional sweep was performed to simulate an injection period variation of four hours for a total of 800 minutes. The purpose of this study was to compare the results of this four-hour injection period with the one-hour injection period from the earlier study. For this study, only two fracture aperture values were included in the parametric sweep, totaling two simulations.

4.3.3 Data Post-Processing

Similar to the previous simulations, the COMSOL output of strain along the length of the simulated fiber was exported for import into MATLAB for each simulation. Initial strain was removed in MATLAB to depict only the change in strain for the duration of the hydraulic test. Both the total strain and strain rate were plotted over the duration of the test and at specific times.

Like the previous simulations, the results were post-processed in MATLAB with simulated gauge length of 10 m as a moving average every 1 m. This simulated the limited resolution of DAS strain rate measurements due to gauge length. The original signal solved by COMSOL was plotted with the signal smoothed by gauge length for comparison. This was an important step to be considered in the design of the hydraulic tests.

To compare the results of the parametric sweeps, the MATLAB results were used to generate a 2D color plot of strain values for the range of simulated injection pressures and fracture apertures. The strain associated with a fracture intersection along the simulated fiber was used in this analysis. Between the beginning of the test to the end of an injection period, the change in strain was used as the color value of the plot. These results may be useful for determining the expected strain to be observed during the tests for this range of permeabilities and injection pressures, but they cannot be used alone to determine the optimal test design.

4.3.4 Testing the Model

The model was tested by comparing results of a single fracture model with the cubic law analytical solution (36). An injection source term was placed in the center of a single penny fracture with a fracture length of 100 m and hydraulic aperture of 5E-5 m. The fluid was injected at 1 kg/s, or 1E-3 m^3/s, with a viscosity of 1.65E-4 Pa·s. The cubic law is expressed as:

$$Q = \frac{W}{L\mu}\frac{b^3}{12}\Delta p \tag{36}$$

where Q is the flow rate, W is the fracture width, L is the fracture length, μ is the fluid viscosity, b is the fracture aperture, and Δp is the change in fluid pressure. The change in fluid pressure was measured between the fracture intersection point and the edge of the fracture. The results of the test were successful in terms of comparing COMSOL's solution of injected pressure propagation within a fracture with the cubic law analytical solution. The results were calculated as follows:

$$Q = \frac{100\,m}{(100\,m)(1.65\cdot 10^{-4}\,Pa\cdot s)}\frac{(5E-5\,m)^3}{12}(4.436\cdot 10^7\,Pa - 2.883\cdot 10^7\,Pa) \approx 0.001\frac{m^3}{s}. \tag{37}$$

Further, to verify that the model was in equilibrium with regards to fluid flow and that the hydromechanical model was fully coupled, the model was tested in 3D in COMSOL. The Darcy's velocity magnitude for the steady state condition was near zero across all outer boundaries, indicating that the fluid flow was near equilibrium (Figure 21, A). To verify that the Solid Mechanics and Darcy's Law interfaces were coupled, the Darcy's Law pressure was compared to the Solid Mechanics pore pressure across the entire volume. Since they were equal, the Darcy's Law and Solid Mechanics interfaces were deemed satisfactorily coupled (Figure 21, B, C).

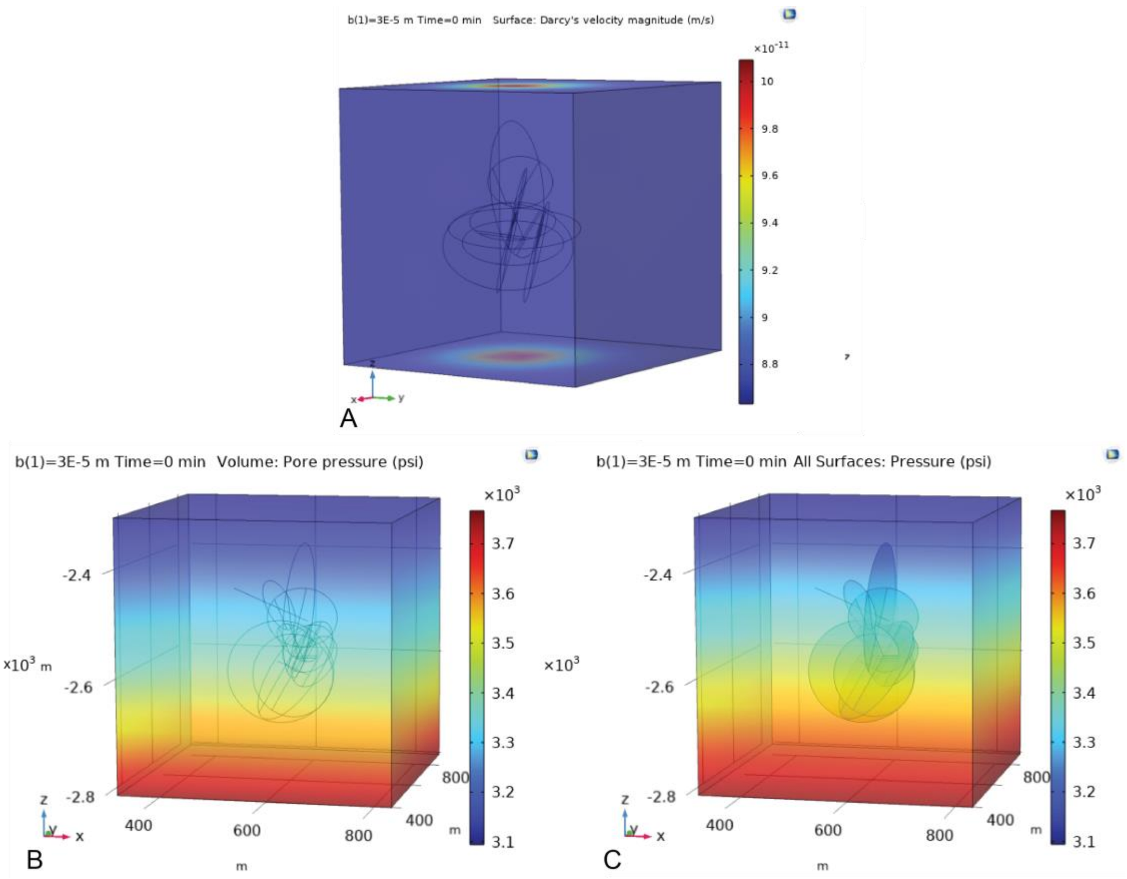

FIGURE 21. Plots to verify steady state. (A) Darcy's velocity magnitude at time 0, steady state. (B) Pore pressure in the Solid Mechanics interface at steady state. (C) Pressure in the Darcy's Law interface at steady state.

CHAPTER 5

RESULTS

5.1 Modeling Strain Signatures as an Indicator of Fracture Connectivity

5.1.1 Simulated DAS-Measured Strain

The results of the COMSOL time-dependent study depicted simulated strain measured along the production well over time. These results correspond to Methods section 4.2 involving Models A, B, C, and D. The strain signatures reflected the stretching and compressing/relaxing behavior of the fiber as the pressure front reached the production well. The sinusoidal hydraulic signal was observed at the production well where an intersecting fracture acted as a conduit to the pressure front from the injection well to the production well (Figure 22). The mechanical strain propagated in advance of the fluid pressure for both injection and withdrawal (Figure 22). For this period of 60 minutes, sinusoidal injection and withdrawal peaked at 15 and 45 minutes, respectively (Figure 22). The strain associated with the first injection period peaked just under 40 minutes (Figure 22). In this study, the length of the simulated well was 250-m, with the toe of the well corresponding to 250 m distance in all figures. In Model A, a well-intersecting fracture crossed the production well at 107 m distance along the well (Figure 23). A near-miss fracture approached the production well around 168 m distance. The near-miss fracture was more directly connected to the injection point than the completely connected fracture. However, the connected fracture experienced larger magnitude strain as it was a constrained conduit for the strain to propagate.

Strain rate along the production well varied over the course of injection and withdrawal (Figure 25). Positive strain rate corresponded to fiber lengthening, while negative strain rate corresponded to fiber shortening. A change in strain rate polarity was associated with the change in direction of fluid pressure propagation. The simulated FO cable along the production well was stretched as fluid pressure propagated toward the well and compressed as fluid was withdrawn. This corresponded to the period of the sinusoidal injection/withdrawal source term. A stress shadow was observed around the opening of near or intersecting fractures with injection and closing with withdrawal. A dovetail pattern in the waterfall plot indicates the propagation of strain from the fracture to the surrounding matrix.

Figure 25 shows the strain rate magnitude at various snapshots in time. The gauge length smoothed the strain rate measurement in space, reducing the spatial resolution of measurement. During initial injection, both intersecting and near-miss fractures experienced only tensile strain rate associated with fracture opening and fluid propagation in the direction of the production well (Figure 26, A). The “near-miss” fracture in this scenario was located closer to the injection point, allowing the strain signal to follow the injection and withdrawal rate more closely. The connected fracture in this scenario, therefore, had a delayed signal compared to the "near-miss,” (Figure 26, B). The strain shadow associated with the closing intersecting fracture and the relaxation of surrounding material was observable even with gauge length applied (Figure 26, C). The gauge length smoothed the signal, obscuring the thin regions experiencing the largest strain. After some time, the withdrawal of fluid led to compressive strain associated with both fractures (Figure 25, D).

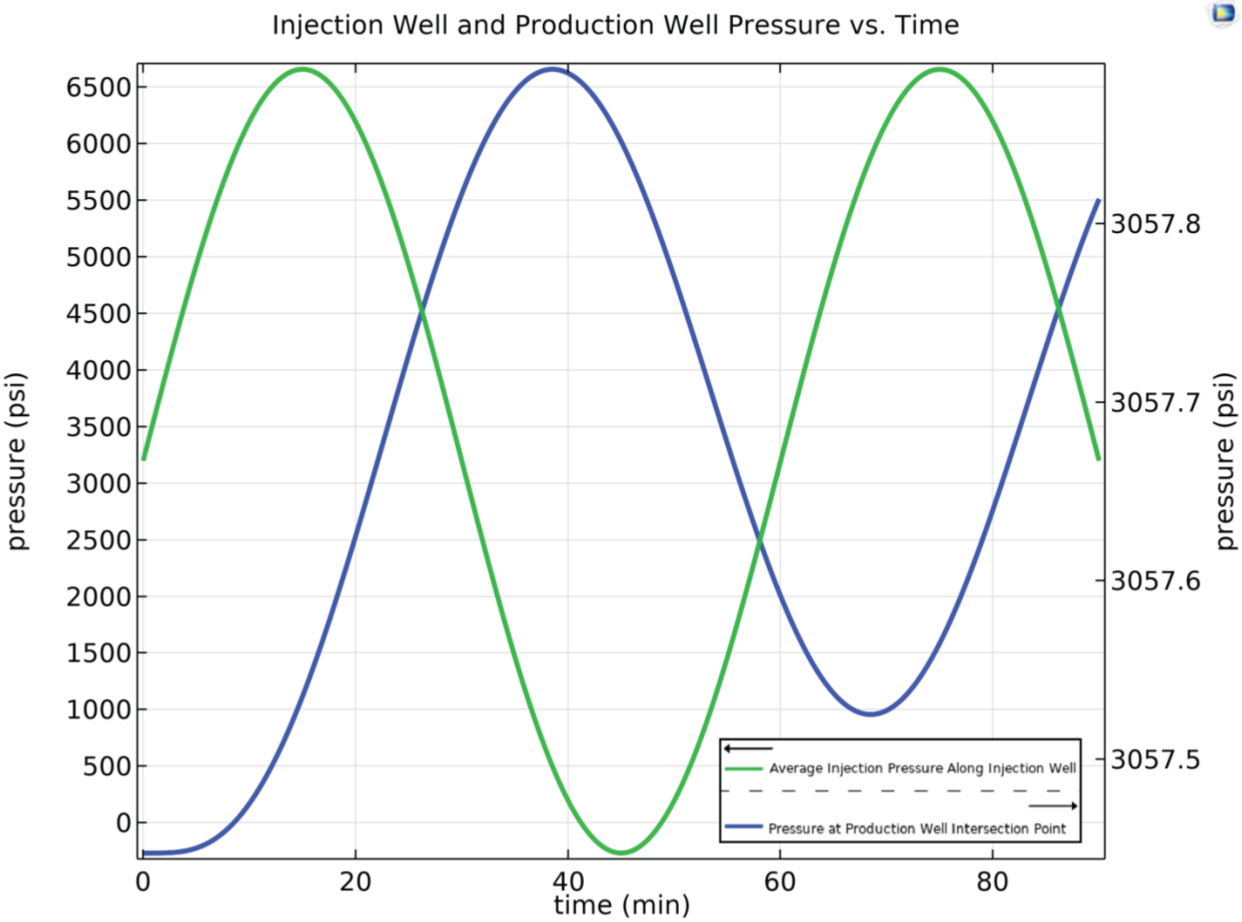

FIGURE 22. Sinusoidal hydraulic signal in propagated from injection well to production well in Model A. Average pressure along the injection well (green) and at a fracture-well intersection point along the production well (blue) over time.

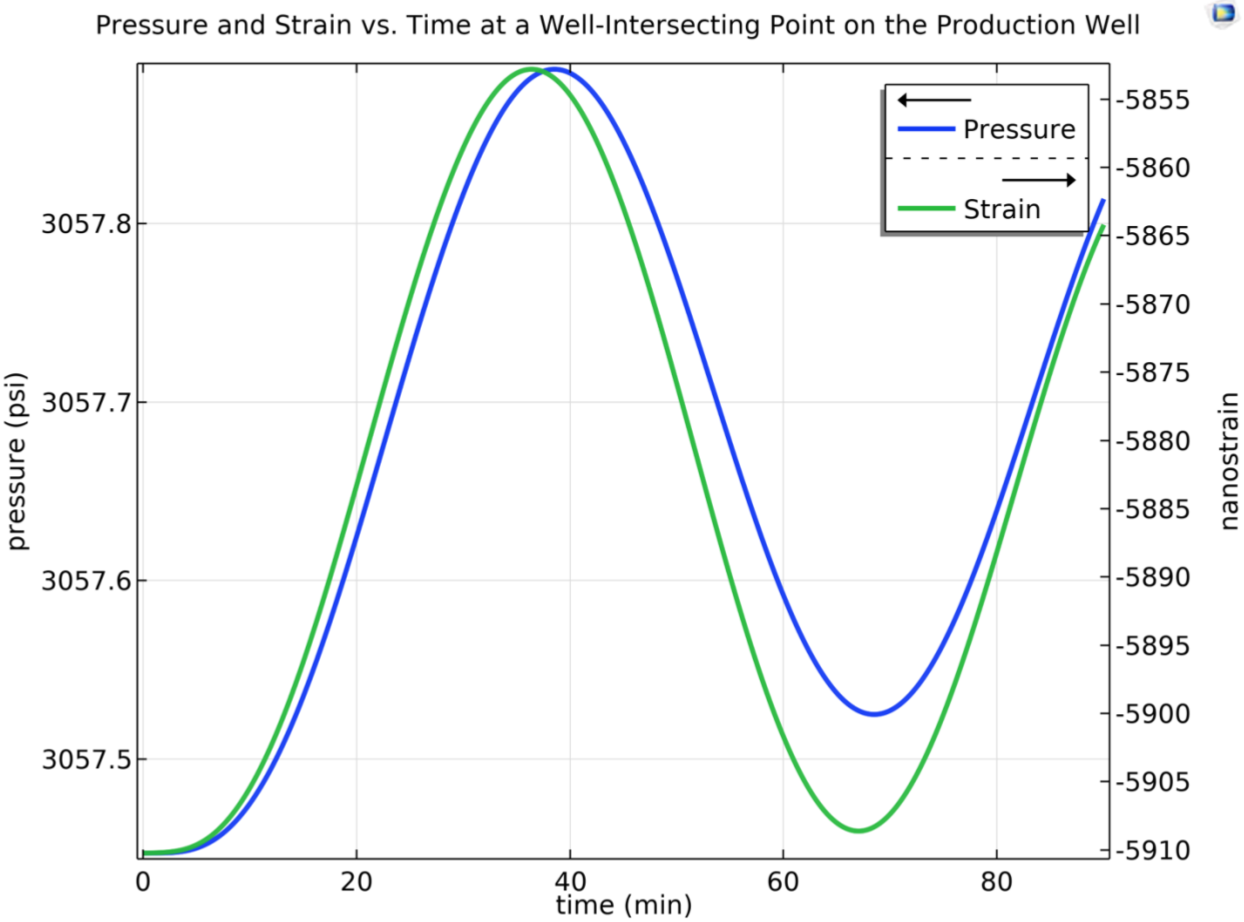

FIGURE 23. Pressure and strain measured at a production well-fracture intersection point of Model A. The nanostrain values were taken directly from COMSOL output, so they were not processed to remove initial strain due to depth in this figure. Only the change in strain is representative of DAS response. In this case, the fracture intersection point change in strain from peak to peak was approximately 55 nanostrain.

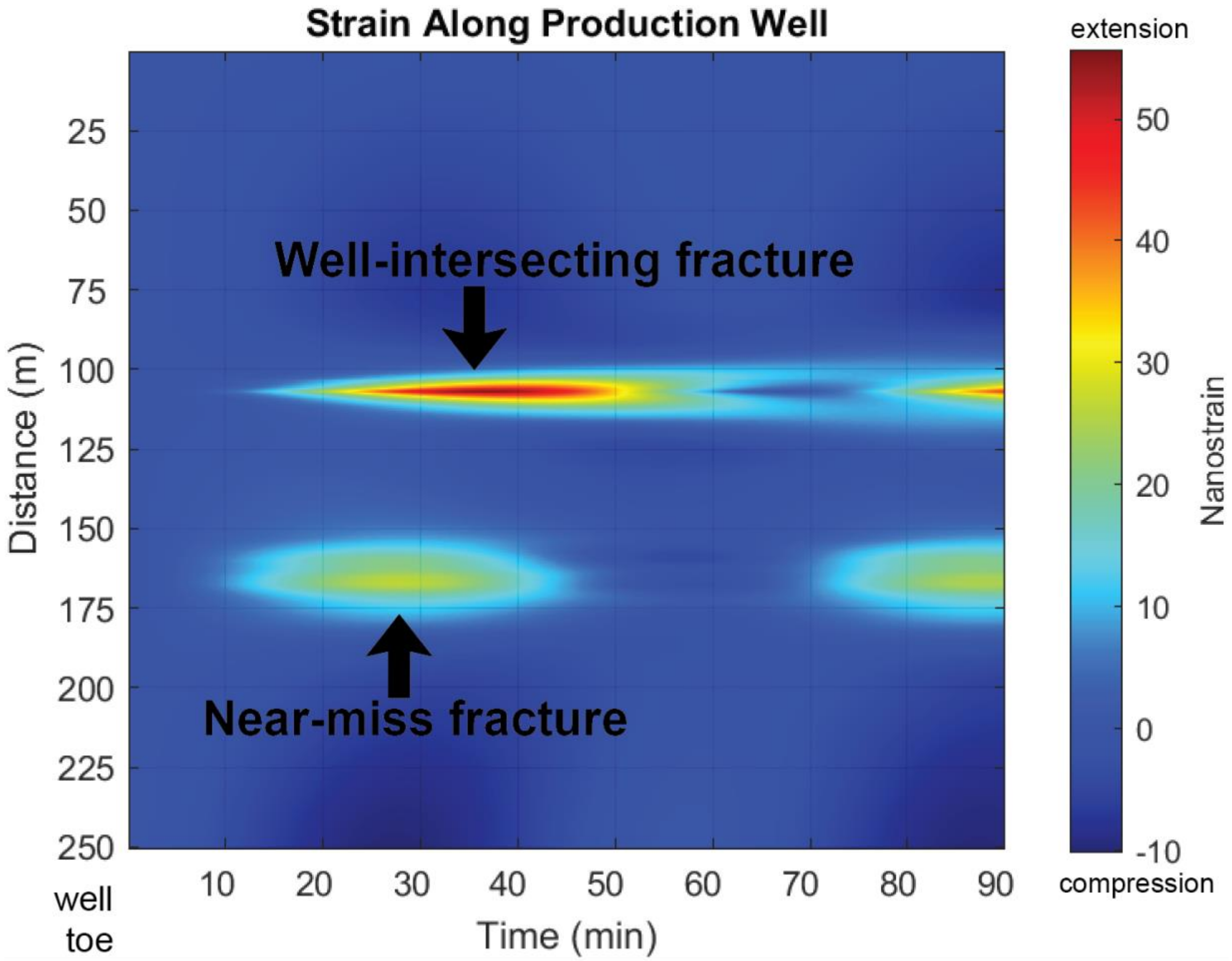

FIGURE 24. Model A two-dimensional color plot of nanostrain measured along the production well over time. The fiber was stretched as injected water traveled toward the fracture and then relaxed as the fluid withdrew. A well-intersecting fracture hydraulically connected the injection and production well. This fracture intersected the production well at 107 m distance along the well. A near-miss fracture approached the production well around 168 m distance.

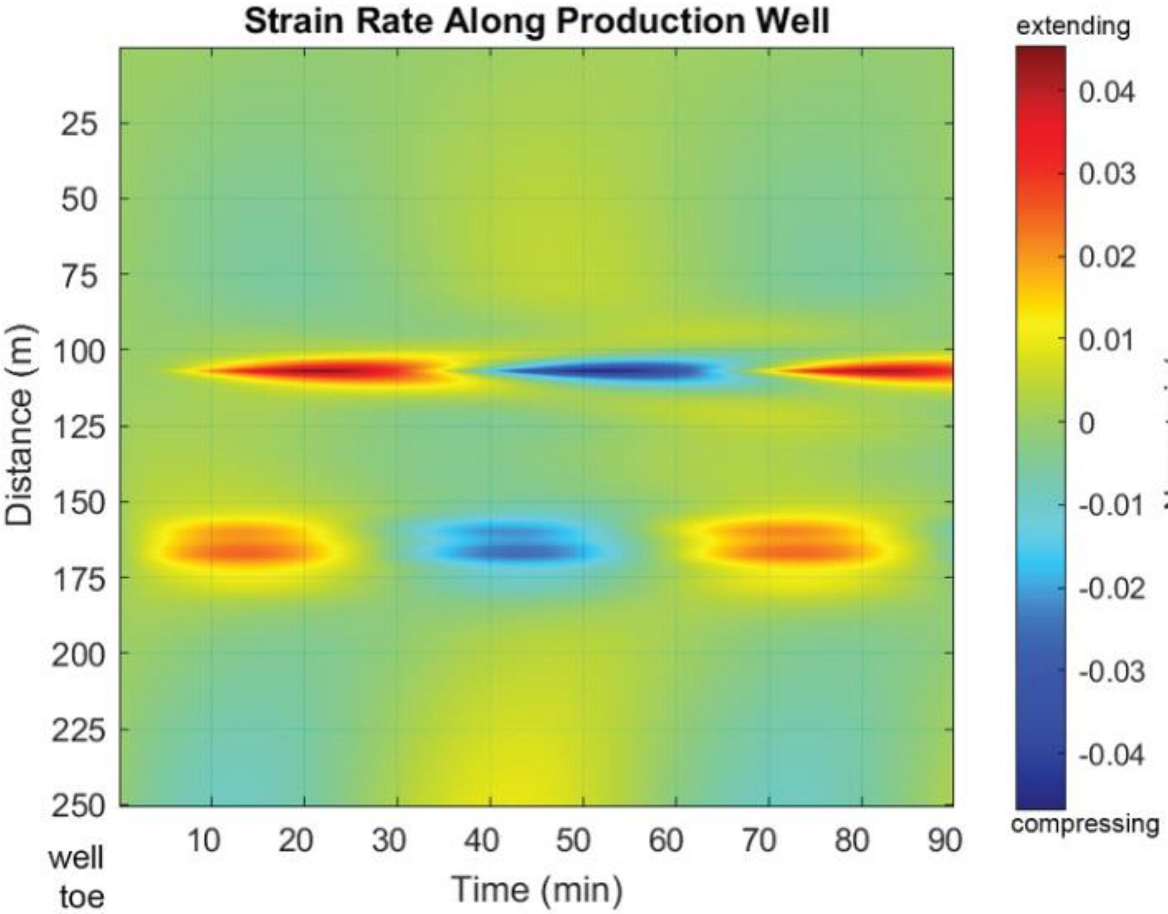

FIGURE 25. Model A strain rate along the well over time. The strain rate along the production well over time demonstrated the change in strain rate polarity over the course of injection and withdrawal. A stress shadow was observable around the opening of the fracture (distance = 107 m) with injection and closing with withdrawal. Positive strain rate values correspond to extending, and negative strain rate values correspond to compressing.

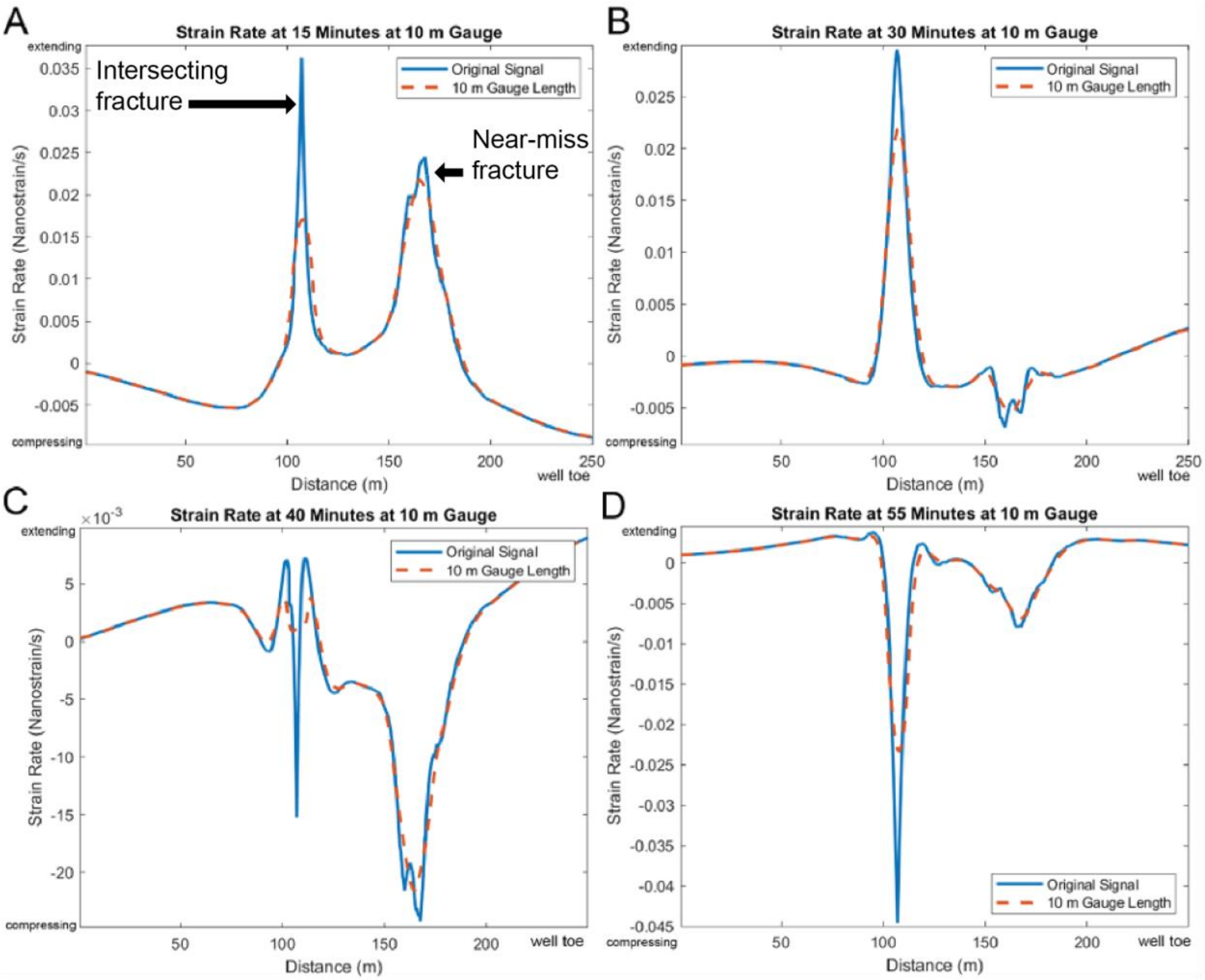

FIGURE 26. Model A strain rate along the fiber at specific times. Strain rate along the distance of the well varies over the course of injection and withdrawal. DAS strain rate measurements limited by gauge length are estimated by applying a 10 m moving average window. Positive strain rate values correspond to extending, and negative strain rate values correspond to compressing.

5.1.2 Variations Due to Fracture Geometry

To demonstrate that near-miss fractures could be identified under different circumstances, DFN geometry variations from Model A (5.1.1) were simulated in Models B, C, and D (Figure 27). The strain rate signature in the DAS data was a function of the distance and orientation of the fracture with respect to the DAS fiber. For the first geometry variation Model B, there are two near-miss fractures and one well-intersecting fracture. The near-miss fracture located around 160 m was located closer and more hydraulically connected to the injection well compared to the other near-miss fracture at around 74 m (Figure 27, B). The more hydraulically connected near-miss fracture was associated with a larger magnitude signal than the other near-miss. The near-miss fracture located farther from the injection well approached closer to the production well than the other near-miss, but it approached at an angle, thus distributing the fluid pressure and strain signal over a wider area along the well. The second geometry variation model, Model C, showed that signals for both the intersecting fracture located closer to the injection source and the near-miss fracture located farther compared to the first model were discernible (Figure 27, C). The last geometry variation model, Model D, demonstrated that the proximity between the two fractures, one intersecting and one near-miss, made it more difficult, but still possible, to discern both fracture positions (Figure 27, D). In these simulations, the gauge length did not have a marked effect on interpretation.

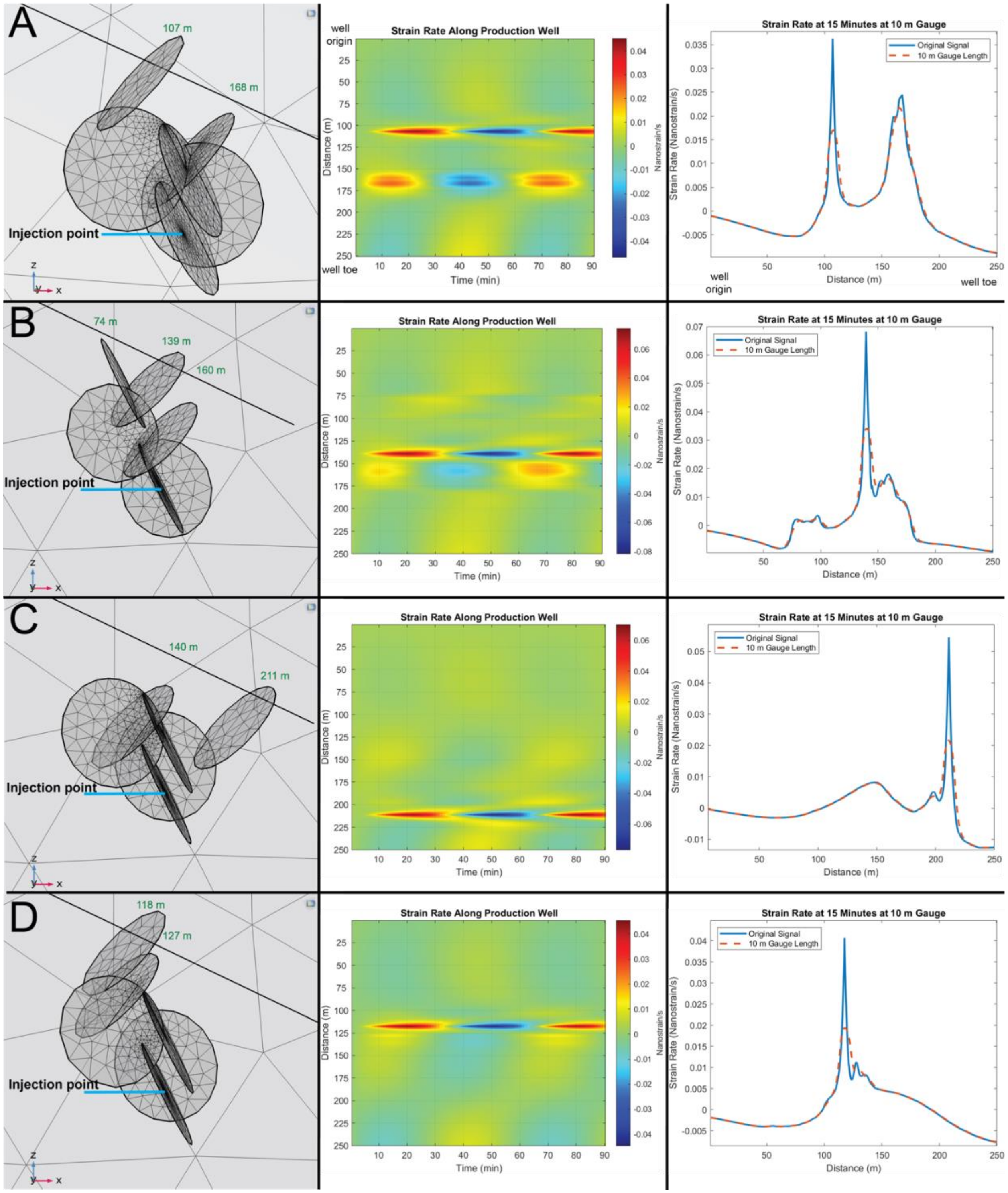

FIGURE 27. Fracture orientations for Models A, B, C, and D. Fracture orientations were adjusted to simulate strain rate along the well over time associated with geometry variations. The distance along the production well at which either a fracture intersects, or a "near-miss" fracture approached corresponds to the y-axis of the color plots.

5.2 Parametric Modeling for Hydraulic Test Design

5.2.1 Dependence Test 1: Hydraulic Test Injection Pressure Dependence

To understand how injection pressure affects the discernibility of connected fractures in the model, a sweep of injection pressures was tested, notated as Dependence Test 1. These results correspond to Model E as described in Methods section 4.3. All simulations in Dependence Tests 1, 2, and 3 used the same model and DFN. As described in Chapter 4.2, this DFN for Model E was more complex than Models A, B, C, and D used in Chapters 4.1 and 5.1. This model is more complex because it is composed of a greater number of fractures and size variations to simulate stimulated fractures more realistically, including randomized fracture sizes (Figure 28). For each fracture aperture value, injection pressures of 1000 psi, 1500 psi, and 2000 psi were tested (Figure 29). All simulations involved three pulses of one-hour periods. After 20 minutes of no injection, injection pulses began wherein water was injected for 60 minutes and then halted for the following 60 minutes. This pattern was consistent for all one-hour injection scenarios for three cycles. Increasing injection pressure corresponded to an increase in strain and strain rate at fiber-fracture intersection points (Table 13).

The fracture aperture was 50 microns and the injection period was 60 minutes. 320 minutes corresponds to the end of the third injection pulse, including a 20-minute static period prior to the first pulse. These values were acquired from the COMSOL strain data post-processed in MATLAB. The values were determined at the fracture intersection at 131.9 m along the production well for the simulation with fracture aperture 50 microns, which corresponded to a fracture permeability of 2E-10 m^2 or 200 Darcy based on the cubic law. This fracture was directly connected to the injection well, which explained why it was the first fracture to be identified by its strain signal in response to fluid flow. The trend for all fracture apertures was the same. Increasing the injection pressure did not have a significant impact on the resolution of this intersecting fracture for this injection period and number of pulses (Figure 29; Figure 30). Increasing the pressure also did not increase the resolution of other connected fractures. The discernibility of the small-aperture fractures did not increase substantially with increasing pressure (Figure 30).

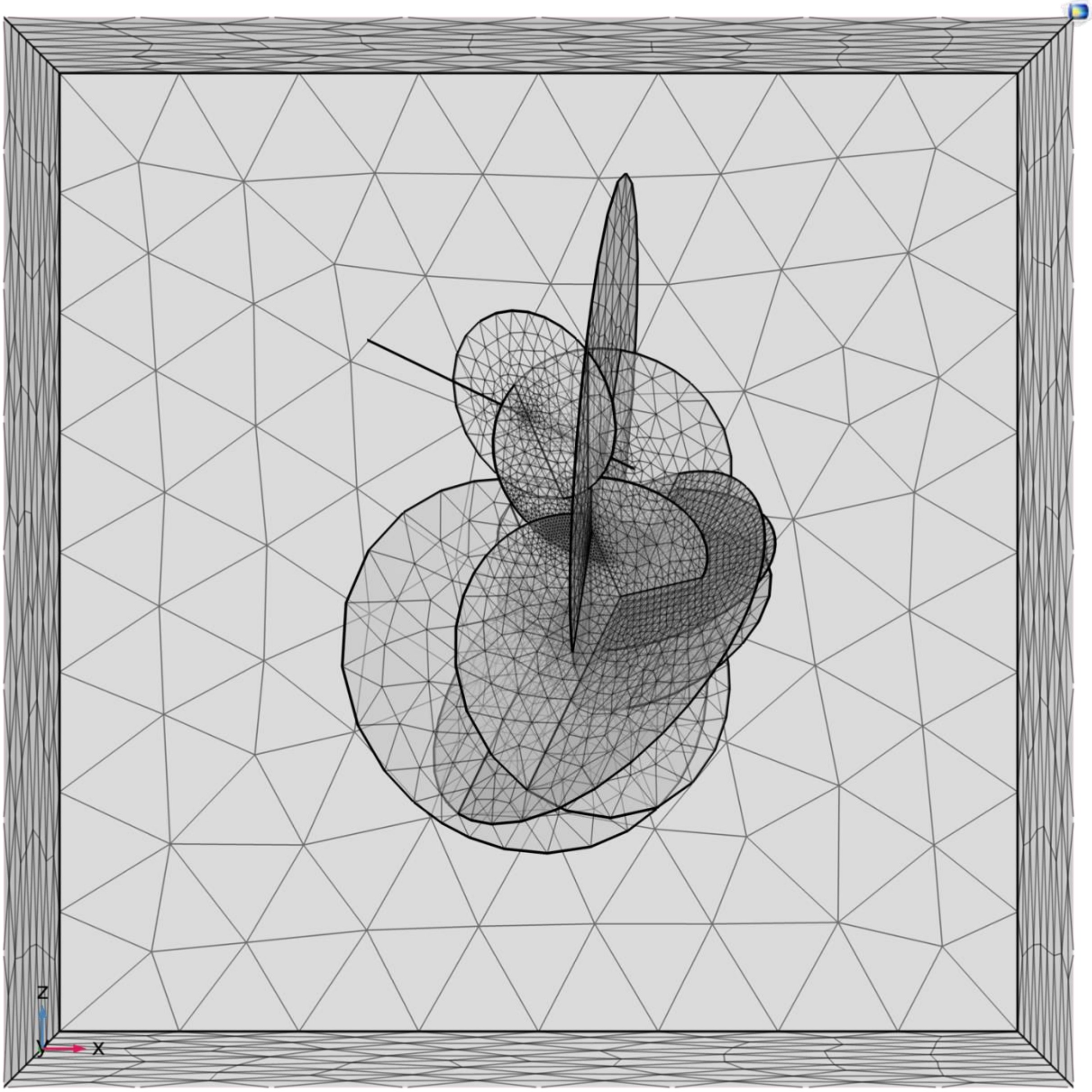

FIGURE 28. Mesh of nine-fracture model used for all the realistic parametric simulations.

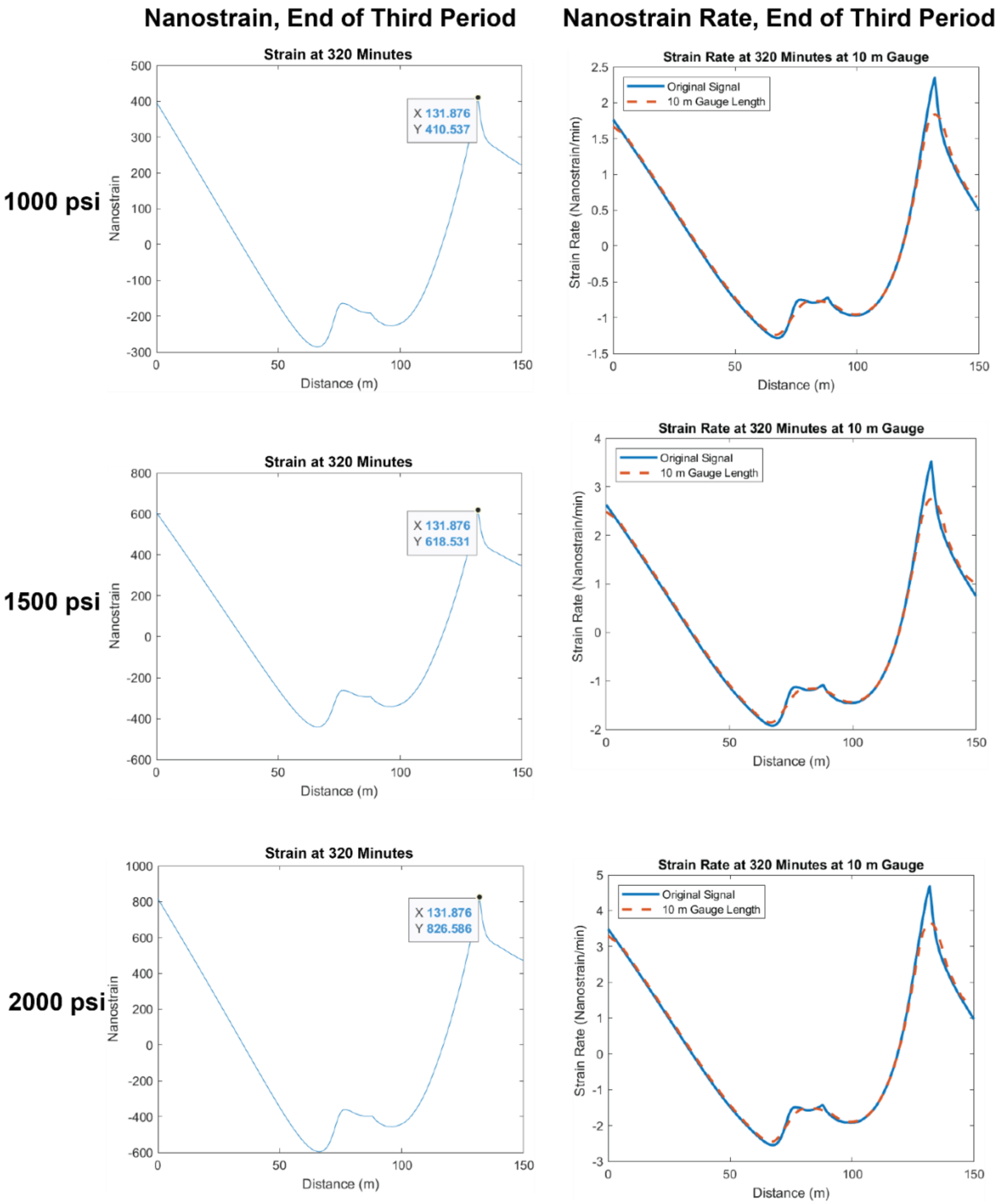

FIGURE 29. Dependence Test 1 strain plot along the fiber after three injection periods. A range of injection pressures were simulated for fracture aperture of 50 microns. A fracture intersects the simulated production well at 131.876 m.

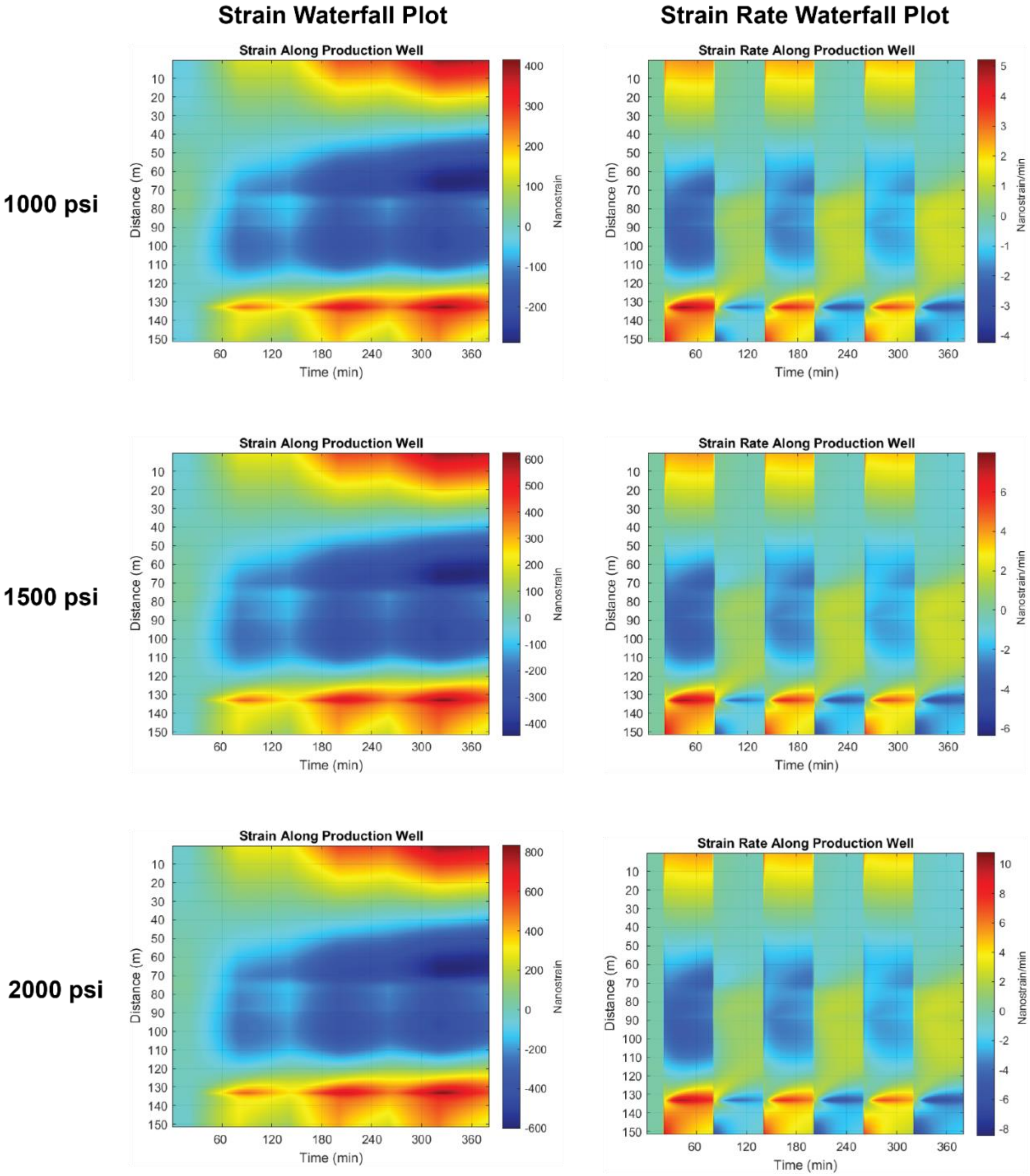

FIGURE 30. Dependence Test 1 two-dimensional color plot of strain along the well over time. A range of injection pressures were simulated for fracture aperture of 50 microns. A fracture intersects the simulated production well at 131.9 m.

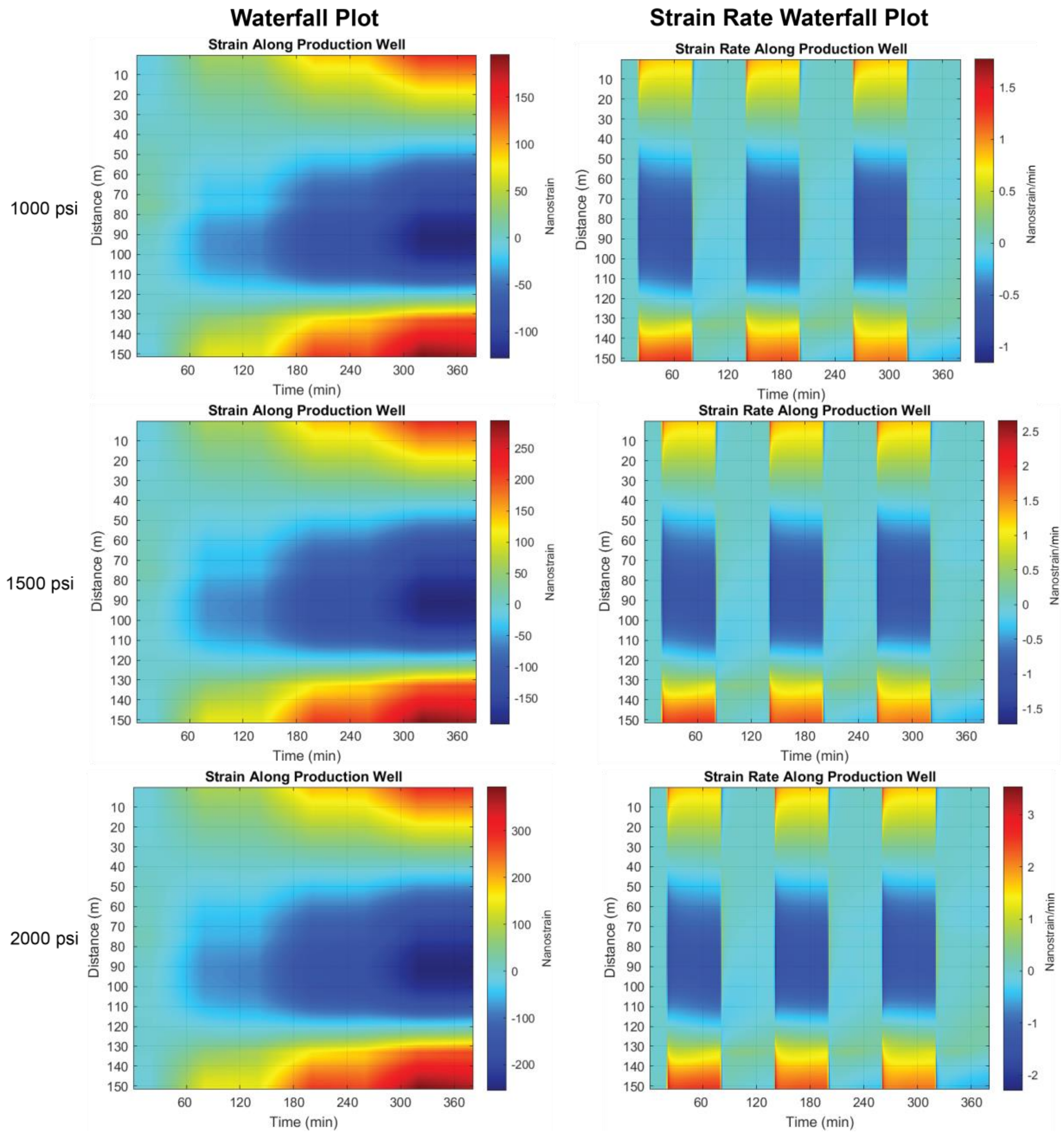

FIGURE 31. Dependence Test 1 two-dimensional color plots of strain and strain rate along the well over time. Fracture aperture was 30 microns. Injection period was 1 hour.

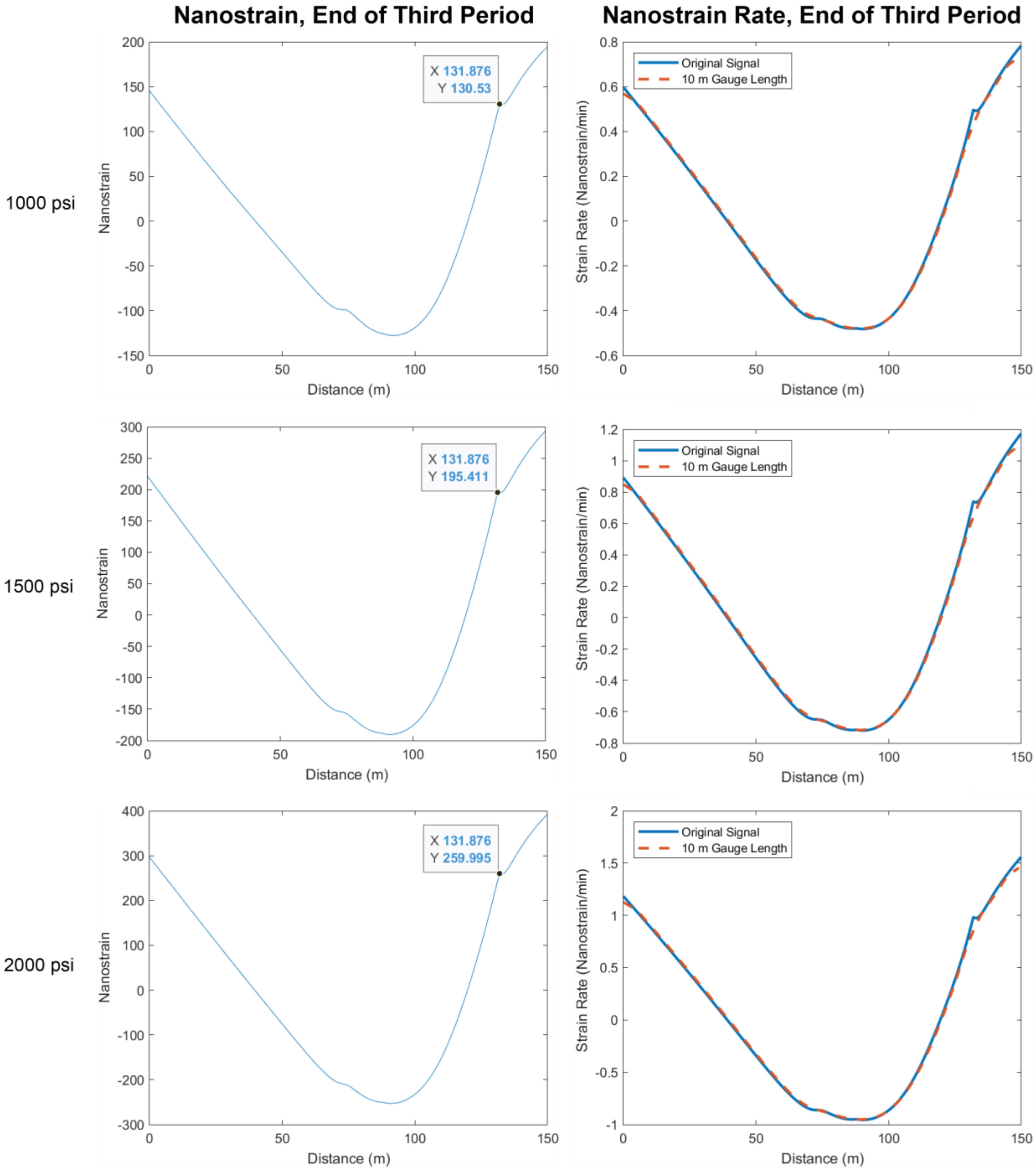

FIGURE 32. Dependence Test 1 plots of strain rate along the well after three injection periods. Fracture aperture was 30 microns. Injection period was 1 hour.

TABLE 13. Relationship Between Injection Pressure and Strain at a Fracture Intersection Along the Simulated Fiber

Injection pressure	Nanostrain at 320 minutes	Nanostrain/minute at 320 minutes
1000	410	2.35
1500	618	3.52
2000	826	4.86

5.2.2 Dependence Test 2: Hydraulic Test Permeability Dependence

Since the fracture permeability is expected to change between hydraulic test design and implementation, a range of permeabilities were tested to understand how permeability will affect results of the test, notated as Dependence Test 2. Four homogeneous fracture apertures for a one-hour period injection scenario were simulated using Model E in four distinct simulations, 30 microns, 50 microns, 75 microns, and 100 microns. The smallest fracture aperture in this test, 30 microns, corresponded to permeability of 7.5E-11 m^2, or 75 Darcy, based on the cubic law. For a four-hour period injection scenario, three fracture apertures were simulated: 10 microns, 30 microns, and 75 microns. The smallest fracture aperture in this test, 10 microns, corresponded to permeability of 1E-11 m^2, or 10 Darcy, based on the cubic law.

Pressure was measured at an intersecting point along the production well during the course of the simulated hydraulic tests. For the 75-micron aperture simulation, the pressure response at the intersection points indicated that flowback was measurable (Figure 32). This was not the case for the smaller aperture fractures, as the hydraulic signal was hardly noticeable and flowback was nearly immeasurable. This may be explained by more fluid reaching the production well for the 75-micron case compared to the 30-micron case.

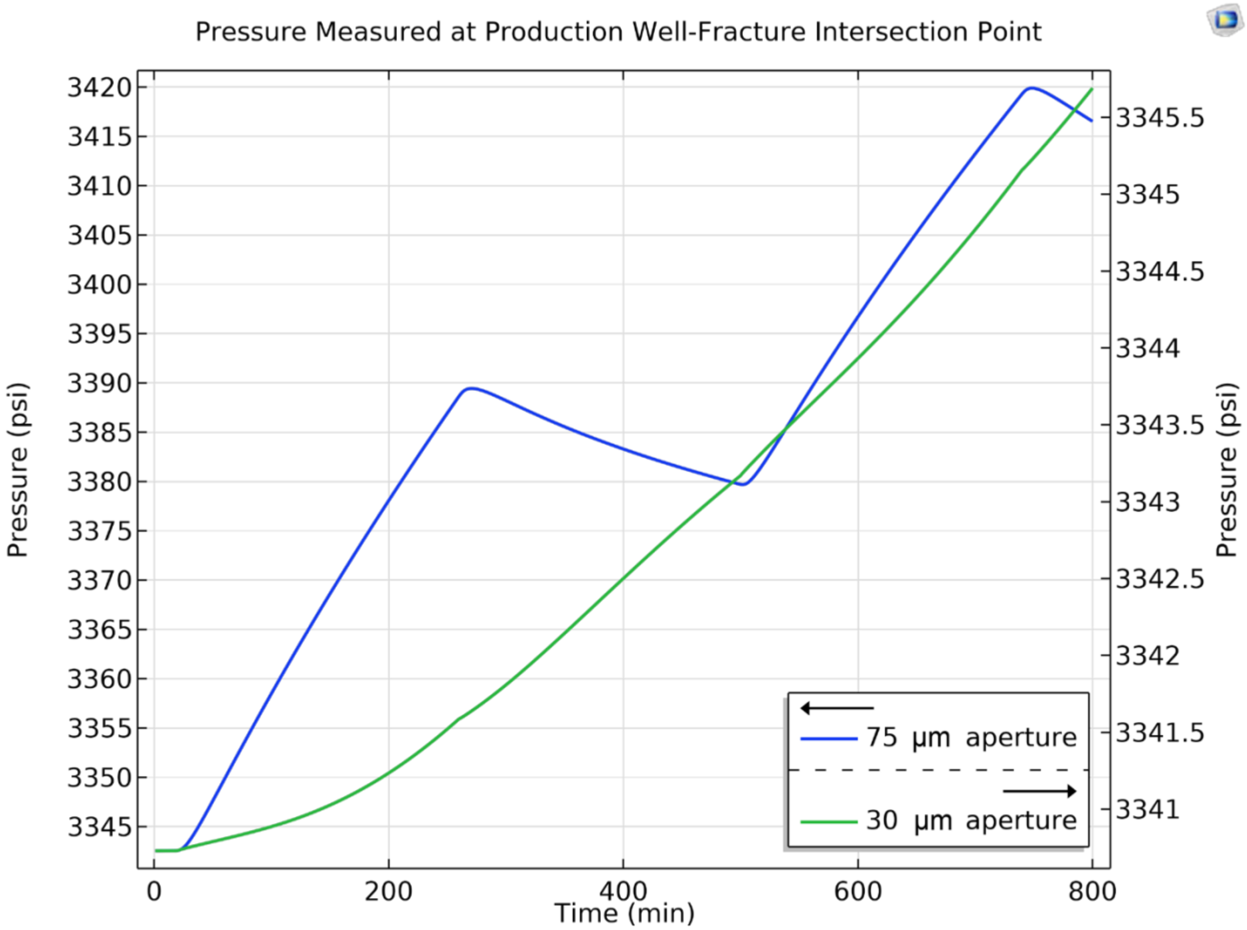

FIGURE 33. Flowback from production well for two apertures. Pressure measured at a point along the production well at which a fracture intersected. Two simulations are shown with different uniform apertures for, 30-micron (green) and 75-micron (blue). Both simulations had an injection pressure of 1500 psi and four-hour period.

The results demonstrated that larger permeabilities corresponded to larger strain signatures associated with a larger volume of water injected into the fracture network toward the DAS trajectory along the production well. The results of three-dimensional fluid flow plots demonstrate that flow was faster and reached farther through the fracture network for larger aperture fractures (Figure 34). During and after injection, three-dimensional plots of Darcy's velocity field and magnitude showed that the pressure gradient is larger at farther distances in fracture networks with apertures of 75 microns compared to 30 microns, as illustrated by the Darcy's velocity vectors in Figure 34 (A, C). In these plots, the Darcy velocity magnitude is expressed with the color bar. After injection ceased, fluid flowing in the fractures farthest from the injection source for the larger aperture fracture network further demonstrated that the fluid traveled farther and at larger velocities through the fracture network.

The propagation of pressure was further analyzed for a single fracture that hydraulically connected the injection and production well. Looking at a single fracture, permeability increase corresponded to greater pressure increase at the furthest point in the fracture. The steady state pressure value at this point was 21.927 MPa (3180.27 psi) (Figure 35, A). That point within the fracture of 30-micron aperture increased by 2.68E3 Pa (0.39 psi) (Figure 35, B). For the 75-micron aperture fracture, the pressure at that point increased by 1.48E5 Pa (21.49 psi) (Figure 35, C). This indicated that the fluid pressure propagated farther and faster in the larger aperture fracture. While the storativity remained the same, larger permeability indicated larger diffusivity. Therefore, the pressure pulse propagated faster.

Figures 36 and 37 show a comparison of fracture apertures and strain response for 1500 psi injection for three one-hour periods. Figures 36 and 37 show that fracture permeability was largely related to strain response. A greater quantity of hydraulically-connected fractures were discernible with the larger aperture simulations. This was the case for all injection pressures with a one-hour injection period. For the smaller fracture apertures, strain response corresponded to fluid flowing through only the fracture directly connecting the injection and production well. With increasing permeability, fluid could flow through several more fractures that eventually connected to the production well within the same timeframe.

In these simulations, fractures with small aperture values were associated with indistinguishable strain signatures. This was likely a result of fluid being constrained in the small fractures and unable to make its way to the production well/DAS trajectory. The general fracture zone was discerned, but the exact locations of fracture intersections were not identified. Many other models at FORGE and other EGS sites have used a larger-than-expected fracture aperture value for their modeling (Finnila et al., 2023; Held et al., 2014; Tenma et al., 2008). This may be to simplify the DFN to account for variability, to reduce the solving time, or to reduce the complexity of the mesh.

A fracture aperture of 10 microns, or 1E-11 m^2 and 10 Darcy cubic-law permeability, was tested with a four-hour injection period scenario (Figure 38). Hydraulically-connected or near-miss fractures were not identified in this scenario. The general inflation of the reservoir due to fluid volume injected in the network was observed. A 10 Darcy permeability does not, therefore, lead to fluid pressure expression in the production well for this injection period.

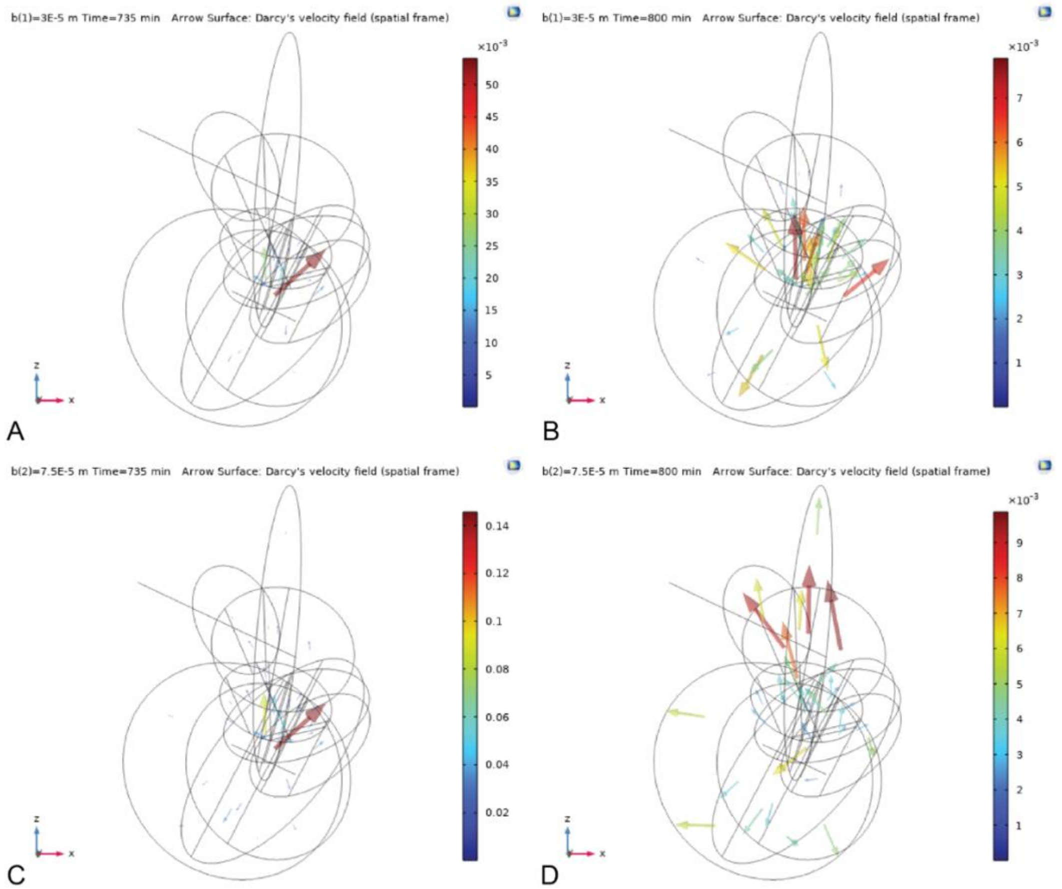

FIGURE 34. Darcy's velocity field and magnitude illustrate the flow for apertures (A,B) 30 microns and (C,D) 75 microns. The color bar corresponds to Darcy's velocity magnitude. At time 735 minutes, five minutes prior to the end of a second four-hour period, Darcy's velocity magnitude is larger for the larger aperture fractures (C) compared to the smaller aperture fractures (D). Time 800 minutes corresponds to an hour after injection ceases.

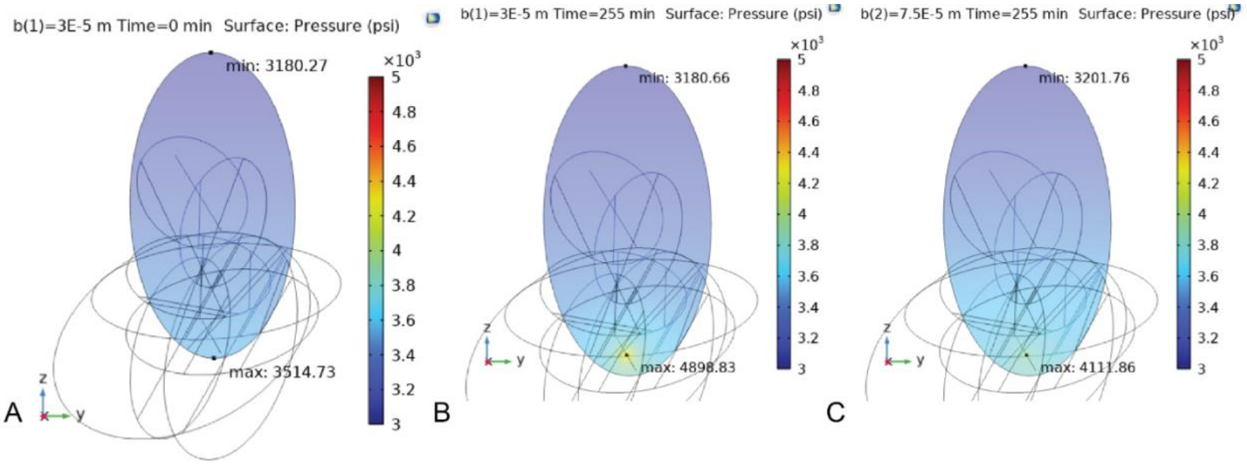

FIGURE 35. Pressure propagation versus aperture for a single fracture in the model. Minimum and maximum pressure at (A) time 0 versus (B) time 255 minutes for aperture 3E-5 m and (C) time 255 minutes for aperture 7.5E-5 m. Time 255 minutes is five minutes prior to the end of a four-hour period injection.

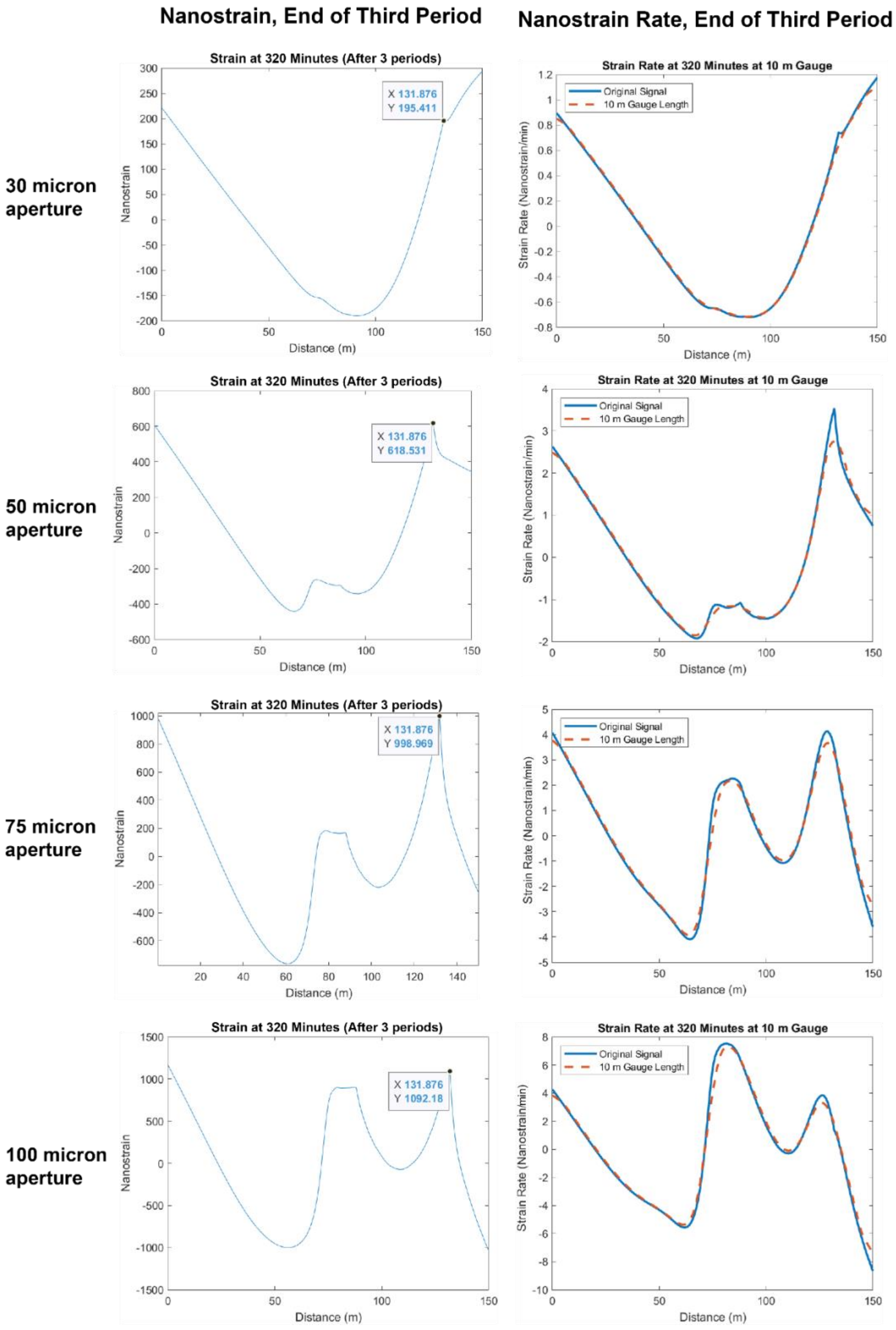

FIGURE 36. Comparison of fracture aperture and strain response. All simulations involved 3 one-hour injection periods of 1500 psi. For the strain rate plots, the DAS gauge length of 10 m was simulated.

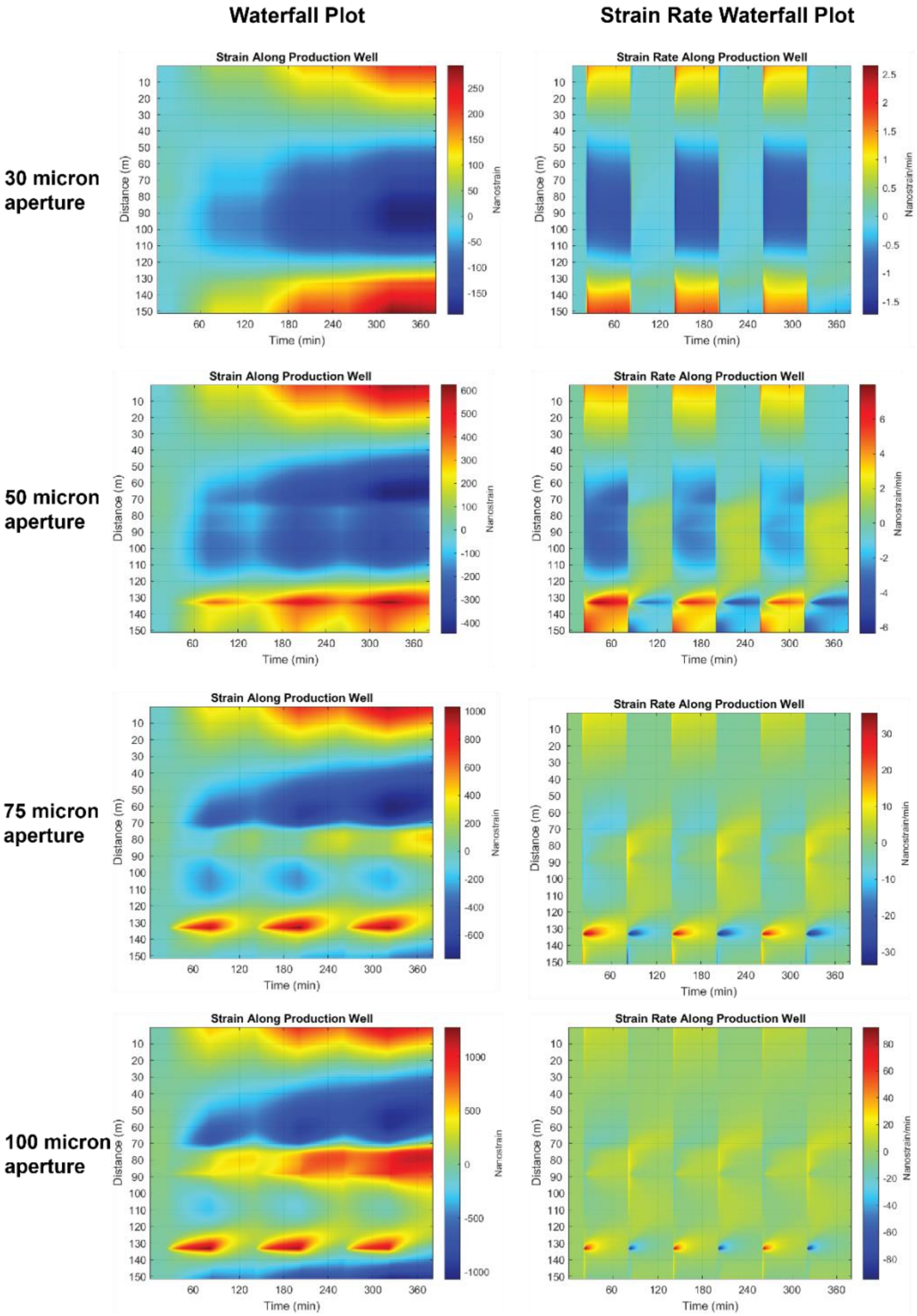

FIGURE 37. Waterfall plots of strain and strain-rate signals over time for three one-hour injection periods of 1500 psi. Three fracture apertures are compared.

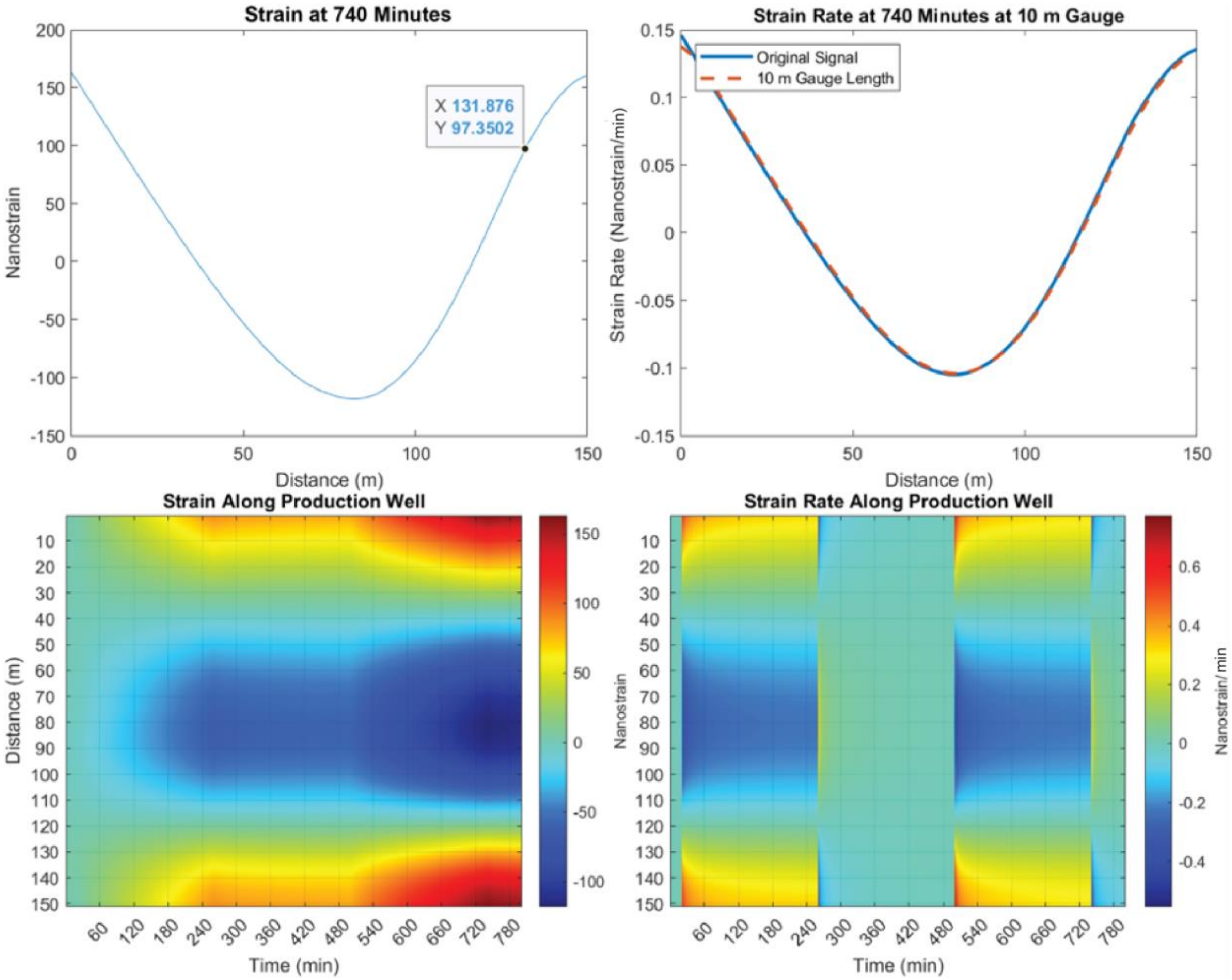

FIGURE 38. Strain and strain rate plots for uniform fracture aperture of 10 micron, or 1E-11 m^2 permeability.

5.2.3 Dependence Test 3: Hydraulic Test Period and Number of Pulses Dependence

To understand the impact of injection period on strain response, two injection periods were compared, one-hour and four-hour periods, notated as Dependence Test 3. The former was run for three periods, totaling three hours of injection time, while the latter was run for two periods, totaling eight hours of injection time (Figure 39). For all simulations in this test, Model E was use with an injection pressure of 1500 psi above static. Increasing the injection period largely influenced the strain response for the two different permeability models simulated. Minus the 20-minute steady state period at the beginning of each simulation, the three one-hour injection periods totaled 300 minutes and the one four-hour injection periods totaled 240 minutes. Therefore, less overall time for the simulation resulted in larger strain response at the fracture intersection point (Figure 38, 38, 39).

At the end of the second four-hour period, another hydraulically-connected fracture became increasingly discernible via its strain response as fluid made its way through it, as expected since the radius of influence is larger and longer periods propagate farther (Figure 41, 42). This resulted in a decrease in strain response for the first-noticeable fracture between the end of period one and the end of period two. In this scenario, the longer period resulted in fewer cycles needed to identify connected fractures.

With regards to the effect of the number of pulses in the hydraulic test, only two pulses were needed to identify a second intersecting fracture zone for the four-hour period simulation. Three pulses of one-hour injection periods did not offer the same resolution as the two pulses of the four-hour injection regarding the other connected fractures. However, the resolution of another connected fracture did improve with each pulse, indicating that fluid pressure was propagating toward the production well. The number of pulses required to influence distinctness of fracture locations may be larger for shorter injection periods, as the three one-hour period scenario failed to reach the strain magnitude in the second connected fracture compared to the two four-hour period scenarios.

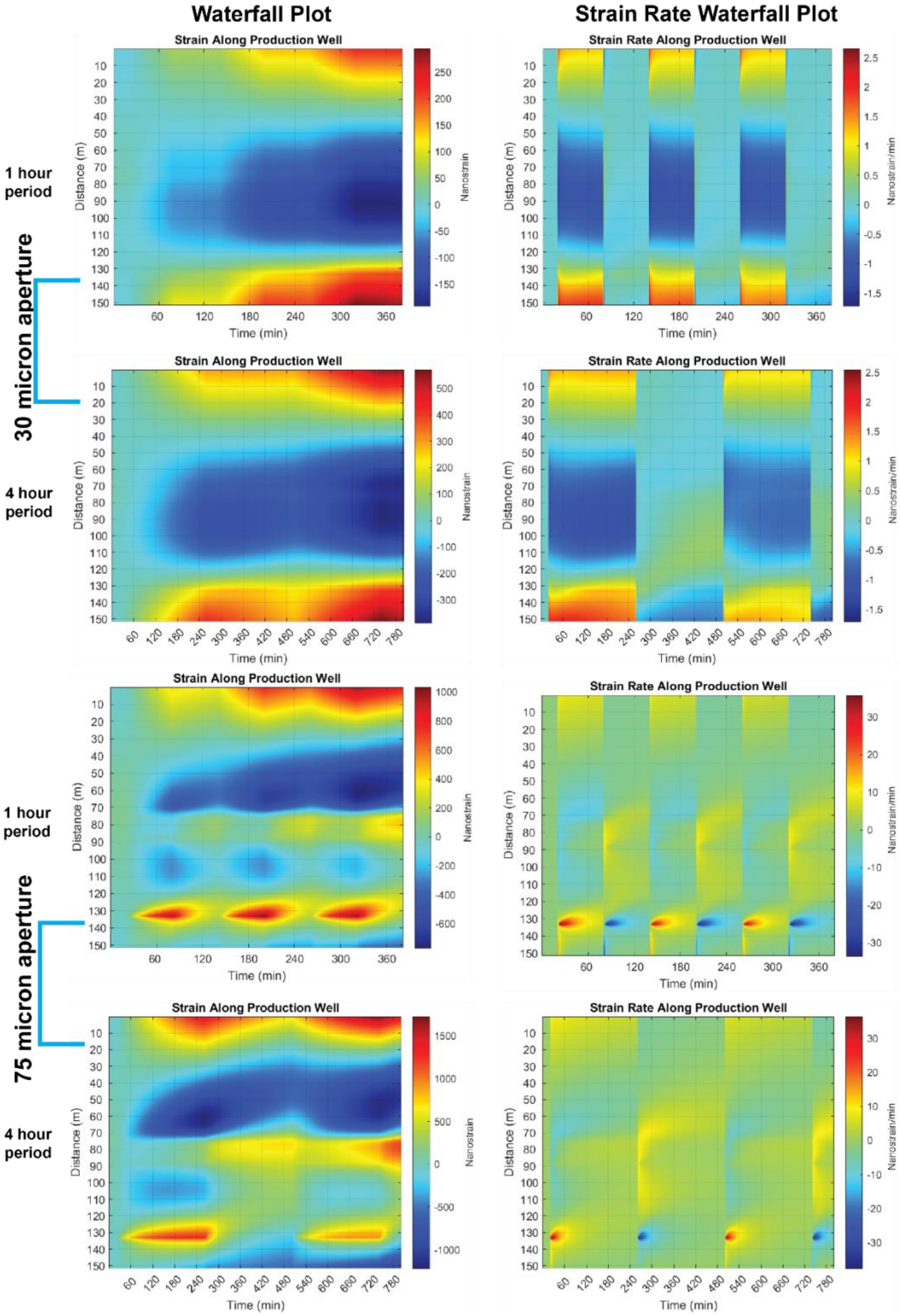

FIGURE 39. Waterfall strain and strain rate plots comparing injection period and strain response for two different fracture aperture scenarios. All simulations involved injection pressure of 1500 psi.

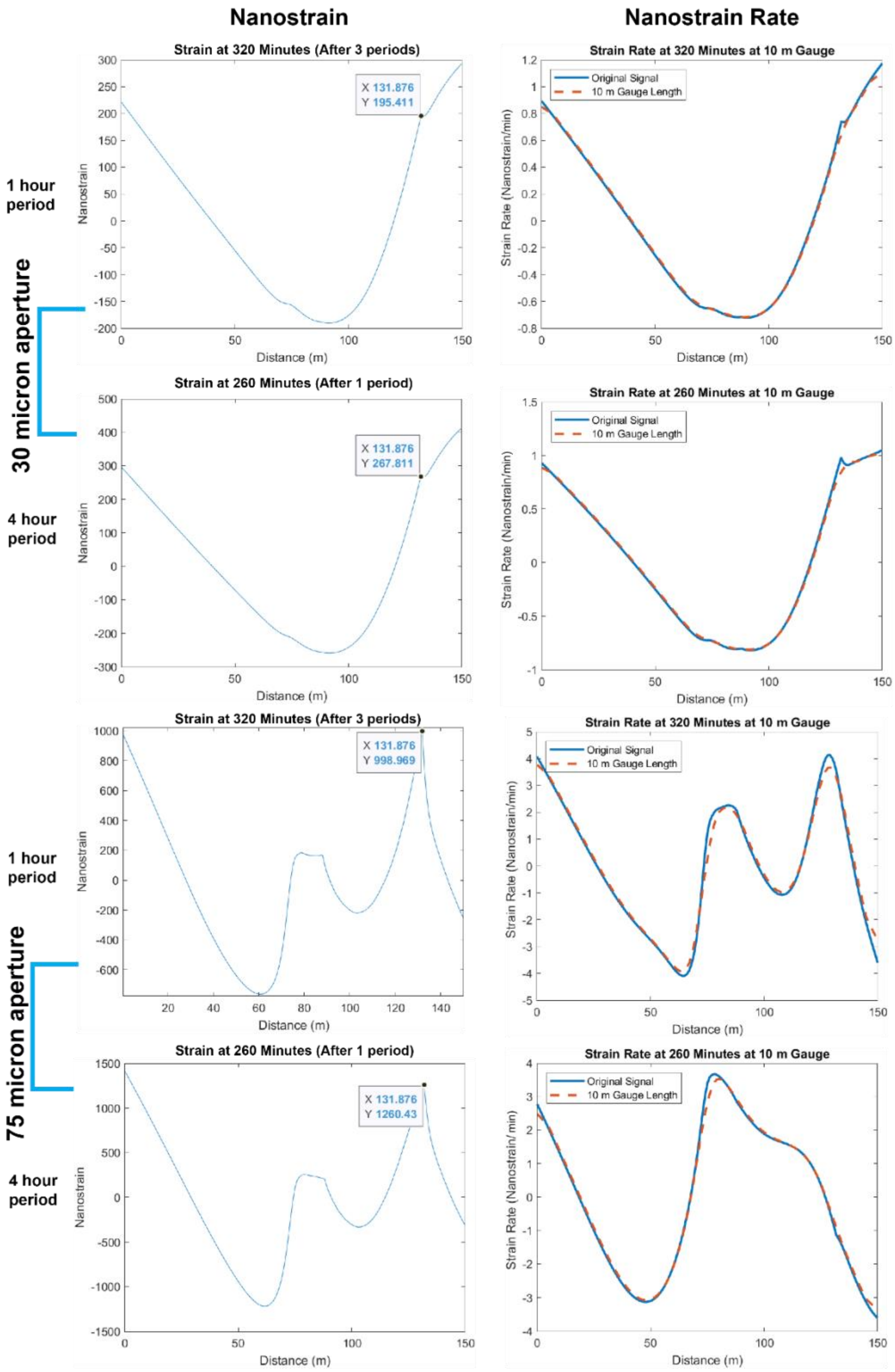

FIGURE 40. Strain response plots for comparison of two injection period lengths, 1 hour and 4 hours. Two different fracture aperture scenarios were tested. All simulations involved injection pressure of 1500 psi. For the strain rate plots, the DAS gauge length of 10 m was simulated.

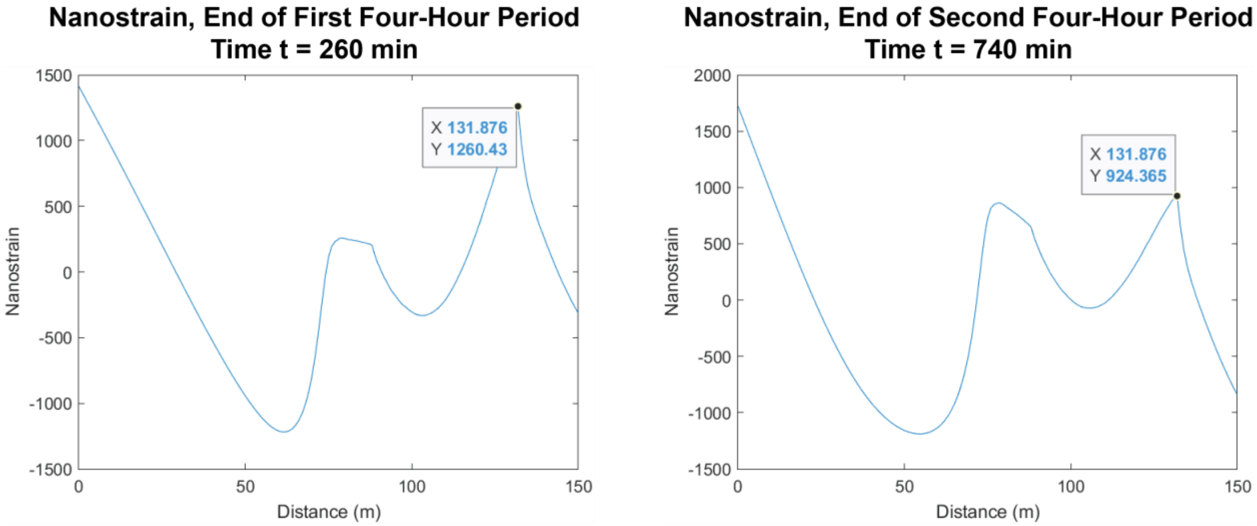

FIGURE 41. Four-hour period plots of strain along the well at specific times. Strain plots at the end of the end of the first and second four-hour periods for a simulation with uniform fracture aperture of 75 micron.

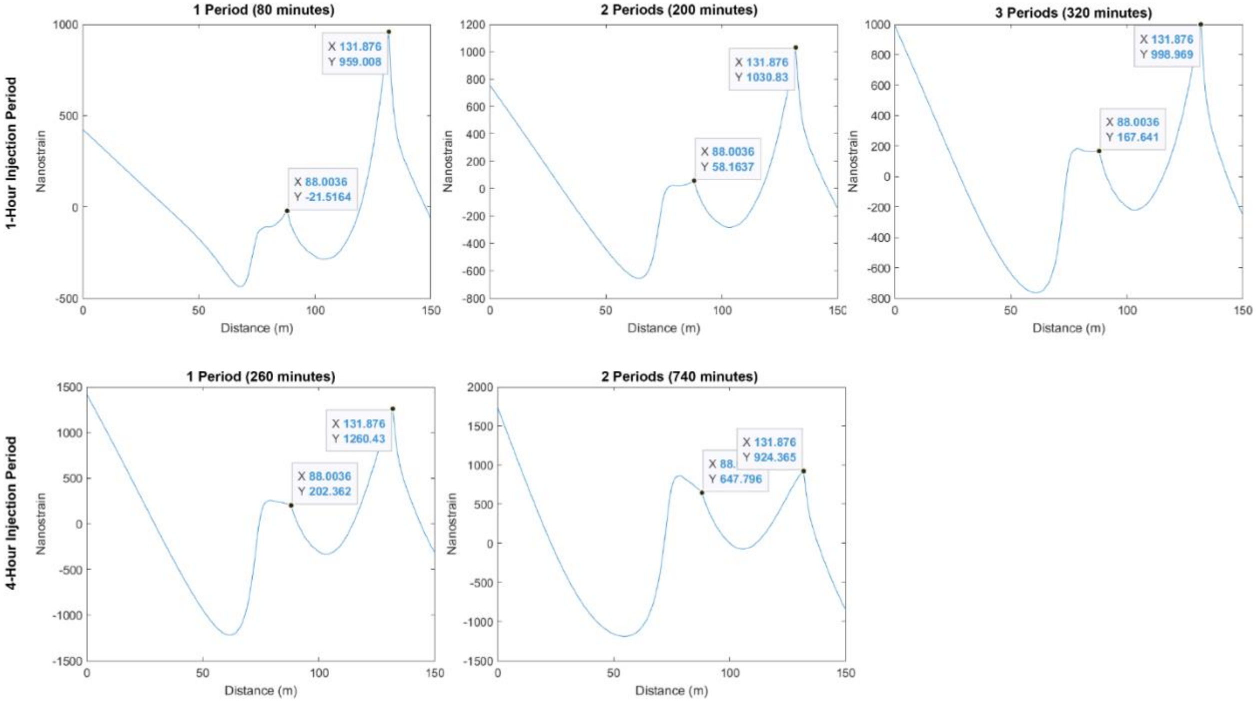

FIGURE 42. Strain plots at specific times comparing effects on multiple fractures from two injection period scenarios in Dependence Test 3. Three pulses for the one-hour injection period and two pulses for the four-hour injection period were simulated. Both simulations have uniform fracture aperture of 75 micron.

5.2.4 Composite Analysis

Multivariate color plots were created to compare the relationship between two dependence tests and the strain response. The relationship between strain response and both injection pressure and fracture permeability were illustrated with a color plot (Figure 43). The values associated with each simulation were plotted and then interpolated to generate a smooth display of these relationships. The strain response expected to be measured by DAS increased in intensity with increasing fracture permeability and injection pressure.

A color plot of injection period versus fracture aperture was produced (Figure 44). For this plot, strain at fracture intersections were plotted for fracture apertures of 30 microns, 50 microns, and 75 microns and injection period of one hour and four hours. These data points were then interpolated. The strain measurements for the one-hour periods were taken at the end of the third period, or 320 minutes, where total injection time was three hours. The strain measurements for the four-hour periods were taken at the end of the first period, or 260 minutes, where total injection time was four hours. The results support that a longer period with fewer pulses may be more rewarding in terms of strain signature than more pulses of a shorter period, as a greater volume of fluid is injected. Nonetheless, permeability appeared to be largely influential to the strain response, as demonstrated by the striking trend of increasing strain response with increasing aperture.

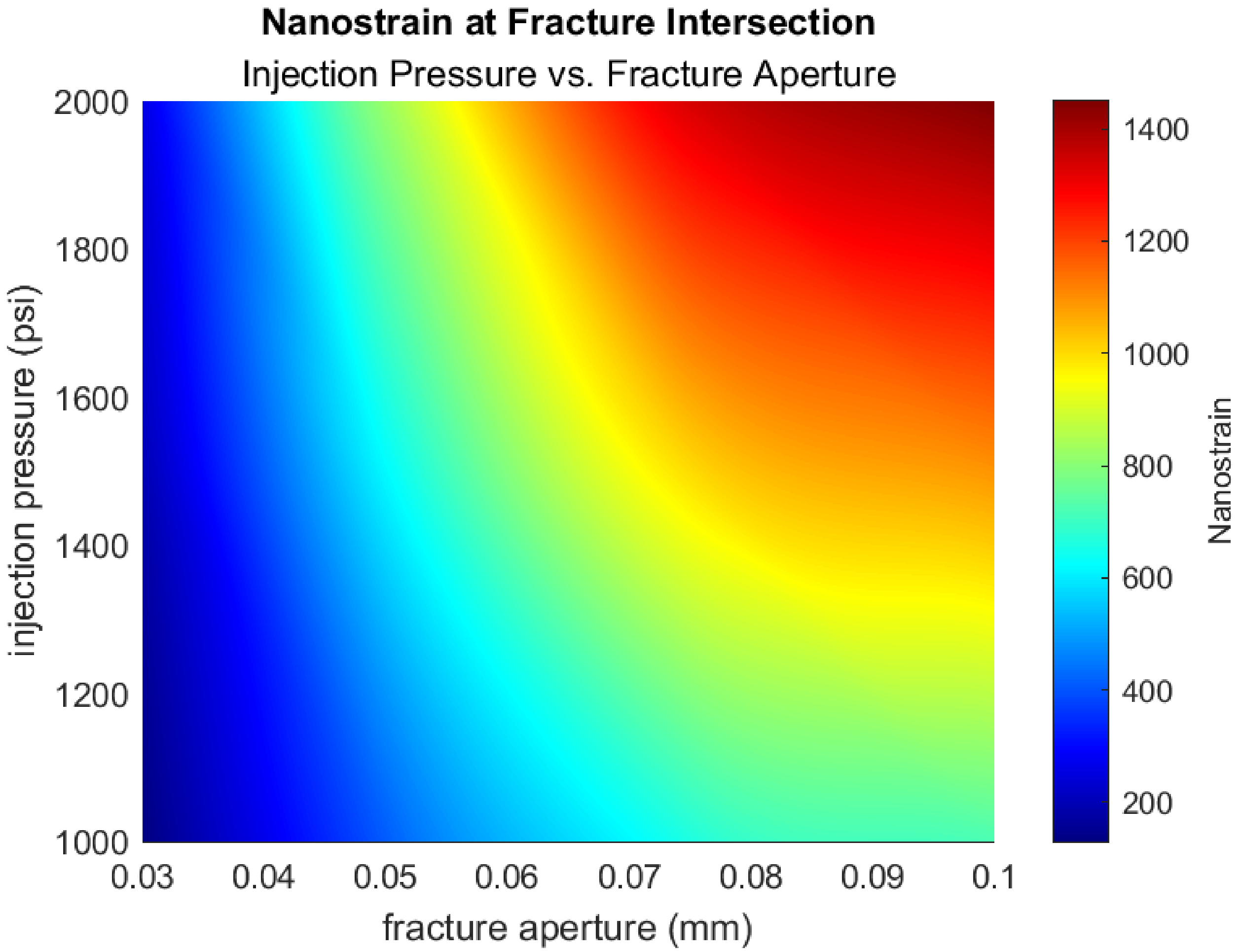

FIGURE 43. Two-dimensional color plot comparing Dependence Tests 1 and 2. The plot was produced from interpolated data from twelve individual simulations with varying injection pressure and fracture permeability. Strain response was influenced by both fracture aperture and injection pressure.

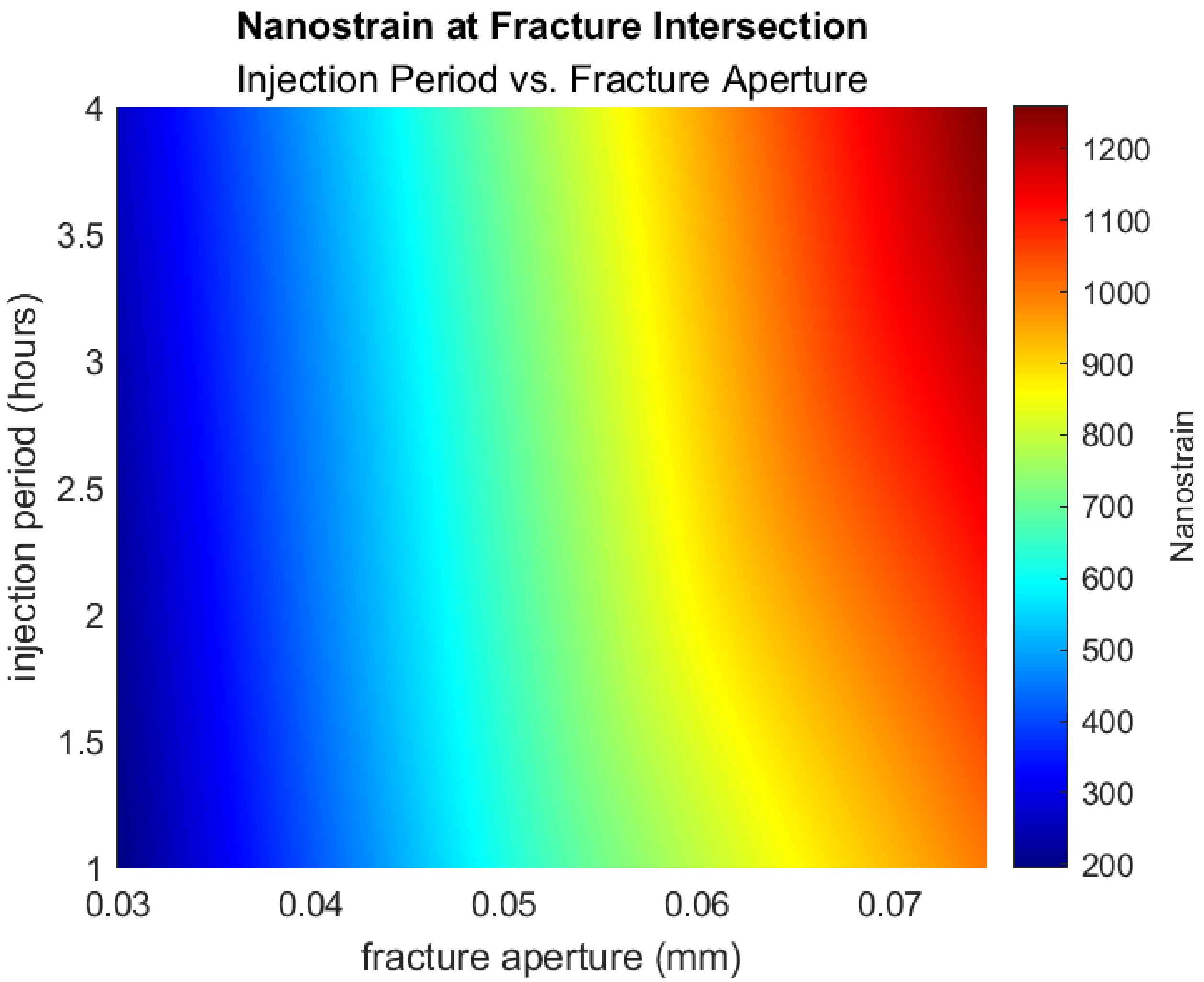

FIGURE 44. Two-dimensional color plot comparing Dependence Tests 2 and 3. The plot was produced from interpolating strain measurements at a hydraulically-connected fracture intersection point for five different injection period and fracture aperture scenarios. Strain response was influenced by both the fracture permeability and the length of injection period.

CHAPTER 6

DISCUSSION

Parametric hydromechanical modeling was used to understand how test design parameters affect DAS response to periodic hydraulic testing, including injection rate, injection pulse duration, and number of repeated pulses to use in the test. These simulations demonstrated how strain response can distinguish complete and incomplete hydraulic pathways. By modeling the Utah FORGE site, where EGS well connectivity will be evaluated by DAS periodic hydraulic testing, we were able to decipher the system response to injection and optimize injection rates and periods.

Previous work showed that strain anomalies, as measured by DAS, were associated with hydraulically communicating fracture zones in a periodic hydraulic test (Becker et al., 2020). This was supported by the poroelastic modeling results in this study, as the known location of fractures corresponded directly with peaks in tensile strain during injection and compression during withdrawal or flowback. The results of the study concurred with previous studies that demonstrated that the mechanical strain propagated in advance of the fluid pressure during both injection and withdrawal. The complexity of the fracture network, and therefore the fluid flow pathways, conformed to the expectations set by previous work.

6.1 Distinguishing Near-Miss Fractures

After hydraulic stimulation, fractures may be incomplete, approaching but not intersecting the production well. These “near-miss” fractures can be addressed in future stimulation stages or re-stimulated to complete the connection. DAS has been established by previous work as a method to identify hydraulically communicating fracture zones (Becker et al., 2020). The results of these simulations indicated that DAS data analysis can be used to identify near-miss stimulated fractures, as their response can be distinguished from fractures that are hydraulically connecting the EGS well pair. Both hydraulically-connected intersecting fractures and near-miss fractures demonstrated periodic strains larger than 1 nanostrain, the threshold for DAS (Becker and Ciervo, 2018). Intersecting fractures produce a distinctly different strain behavior than near-miss fractures on the strain-rate waterfall plots. Hydraulically connected, well-intersecting fractures were characterized by large magnitude, sharp strain rate signals, whereas “near-miss” fractures were characterized by smaller magnitude, broad signals. Both near-miss and intersecting fractures corresponded to stress shadows surrounding the fracture location. “Dovetail” signatures (e.g., Figure 23, 25) characterized the regions just outside the fracture zone to make room for the relaxing of local material. Near-miss fractures were associated with less extreme dovetail signatures as there was no opening or closing of a fracture or fluid propagation directly along the well. Near-miss fractures that were oriented obliquely to the direction of the DAS fiber produced a broader and lower magnitude strain rate response than those oriented perpendicular to the DAS fiber. These dovetail signatures were blunted, but not obscured by DAS gauge length limitations.

6.2 FORGE Hydraulic Test Expectations

To assist with the design of periodic hydraulic tests to be conducted at Utah FORGE, parametric modeling was performed using a model representative of the FORGE site. The dependence of strain signatures observable by DAS was analyzed in terms of injection pressure, injection period, and the number of pulses. Within the complex fracture network, there was an increase in the number of interrogated fractures with increasing period, corresponding to the radius of influence (Equation 5). The quantity of fractures interrogated in the simulations also increased with increasing permeability, thus further supporting the relationship between diffusivity and radius of influence. The models are in line with these simple representations of radial flow, lending confidence to the results of the simulations. A longer injection period may be more effective to map fractures intersecting the production well than larger injection pressures for this type of periodic hydraulic test, as a larger volume is injected with a longer period. The number of pulses required to influence distinctness of fracture locations may be larger for shorter injection periods, as only two pulses were needed to identify a second intersecting fracture zone for the longer period simulation. The results demonstrated that increasing injection pressure from 1000 psi to 2000 psi did not substantially increase the distinctness of the fracture locations for a one-hour injection period. While the color plots (Figures 43, 44) depict the relationship between measured strain, period, and injection pressure, they fail to depict the increase in the number of fractures resolved. Because increasing the period of the hydraulic tests probed farther into the formation, a larger number of connected fractures were interrogated and resultantly distributed the fluid pressure and strain magnitude across several fractures intersecting the well (Figure 41, 42). Overall, the increase in period and number of pulses were the determining factors that increased the quantity of resolvable connected fractures. To interrogate fractures farther from the production well, smaller injection periods may be applied.

Because fracture permeability will change with further stimulation, this variable was also included in the parametric simulations. The fracture permeability was a significant factor in the results of the simulations. This phenomenon was described by the cubic law, which describes that flow rate is directly proportional to the aperture cubed (Equation 17). Larger fractures allow for significantly greater flow rates and more space for fluid to pass through. The results of these simulations indicated that fracture permeability influenced strain response and the discernibility of the location of fractures that hydraulically connect the well pair. Figure 37 revealed that a fracture network with an aperture of 30 microns was less discernable than the larger aperture fracture networks with an aperture of 50, 75, and 100 microns. This was the case for all pressures and periods tested. Increasing the injection pressure and period appeared to greatly affect the distinctness of small aperture fractures more so than large aperture fractures. For example, Figure 40 shows that increasing the period from one to four hours greatly improved the distinction of the 30-micron fracture intersection, while it made less of an impact on the distinction of the 75-micron fracture intersection. For these reasons, it may be expected that fracture networks with stimulated apertures of at least 50 microns may be resolved by DAS for the minimum parameters tested in this study, and networks with apertures below 50 microns may require larger injection pressures and periods. While it was determined that smaller fracture permeability decreased the distinctness of the fracture locations, these simulations demonstrated strong potential for mapping fractures through which fluid flows between injector and producer using strain as the indicator for the reservoir characteristics simulated in this study.

While numerical models have different, and therefore non-unique, results, the results are reasonable in comparison to the analytical solution and simulations run by Ratnayake and Ghassemi (2023a). The fracture network used in these simulations was more complex than a single fracture connecting the well pair, as several fractures intersected one another, had different shapes, and had different positions relative to the well pair and one another. This complexity implied that fluid flowed through many pathways and directions before eventually reaching the production depending on permeability and test parameters. This, in turn, added substantial complexity to predicting and interpreting DAS response. The flow pathways between the well pairs were widespread and dynamic, so the fluid was straining the formation in more regions than one, as modeling in other studies exhibit.

For small fracture permeability values, the noticeable strain anomaly corresponded to nearly the whole section of the 61 m open toe. This was distinct from the larger fracture permeability simulations, as strain anomalies were identified over a wider area along the production well where fractures extended. This implied that the smaller strain signatures associated with the smaller fracture permeabilities corresponded to flow in fractures near the injection well source. The small aperture fractures corresponded significantly smaller fluid flow rates, as described by the cubic law (Equation 17). Those near-source fractures were identifiable as fluid and strain propagated through them, but the fractures farther away from the injection source were not yet taking fluid. This contrasts with strain signatures observed for larger fracture permeabilities, in which the activated fractures closer to the production well measurement location overshadowed the fractures closer to the injection source, but farther from the measurement site (Figure 40). Since the peak strain corresponded to where the fluid was flowing and straining the formation, it is suggested that future work attempt to map all fractures with an injection rate such as 1500 psi and a long injection period such as 4 hours. For stimulated fracture apertures of at least 50 microns, the minimum parameters tested in this study, injection pressure of 1000 psi for a 1-hour injection period, may be sufficient.

Shortcomings in this method include the simplicity of the DFN. This simplified fracture network may not have been representative of the more complex fracture network with a larger combined permeability. Additionally, the use of uniform fracture aperture may be disadvantageous to the realistic model, as the fractures are not expected to have uniform aperture. A sensitivity analysis for variable aperture is recommended. Furthermore, the results of COMSOL poroelastic modeling should be compared to that of other poroelastic modeling software and real data in future studies.

CHAPTER 7

CONCLUSION

Hydromechanical modeling was conducted to support periodic hydraulic tests at the Utah Frontier Observatory for Research in Geothermal Energy (FORGE). These tests aim to understand flow continuity between the injection well and the production well in this Enhanced Geothermal Systems (EGS) field laboratory. Periodic hydraulic tests conducted at varying frequencies allow for interrogation of different regions of the formation. At Utah FORGE, a fiber optic cable will be installed along the production well, 16B(78)-32, which will be positioned 100 m above and parallel to the injection well, 16A(78)-32. Distributed acoustic sensing (DAS) measures oscillating strain rates along the fiber. The response to injection will be measured by DAS at Utah FORGE as fluid injection hydraulically strains the stimulated bedrock. This measured response will be applied to evaluate the stimulated fracture network between the well pair.

As a precursor to the hydraulic tests that will be conducted at Utah FORGE, parametric hydromechanical models were generated to understand how various design parameters affect DAS response, including injection rate, injection duration for each pulse, and number of repeated pulses to use in the test. This hydromechanical model also simulated the low-frequency sub-nanostrain signatures of both complete and near-miss fractures observable by DAS. The model constructed with COMSOL Multiphysics software simulated the FORGE reservoir and DAS hydromechanical response to the hydraulic test. These simulations indicated that near-miss hydraulically connected fractures may be identified and distinguished from intersecting hydraulically connected fractures through DAS data analysis. By locating near-miss fractures, it may be possible to re-stimulate and extend these fractures and thus improve hydraulic connectivity between injector-producer well pairs.

The design of DAS periodic hydraulic tests was determined to be largely dependent on total injected volume and mean fracture aperture. Fractures within a network with mean aperture below 30 microns were not detectable by DAS for the tested injection pressures and periods. For mean fracture aperture less than 50 microns, an injection pressure of 1500 psi and injection period of 4 hours is recommended to detect the small aperture fractures. For known stimulated fracture apertures of at least 50 microns, the minimum parameters tested in this study, injection pressure of 1000 psi and injection period of 1 hour, may be sufficient. Increasing the injection pressure and period beyond 1000 psi and 1 hour respectively did not significantly increase resolution of the intersecting fractures of a network with mean aperture larger than 50 microns.

APPENDIX

COMSOL AND MATLAB FILES

The COMSOL and Matlab Files are available on the Geothermal Data Repository (https://gdr.openei.org/). PlotStrainFromCOMSOL.mlx is a Matlab® data file containing the code for plotting strain data derived from COMSOL for this study in .csv format. This code detrends the data, generates waterfall plots, and applies a gauge length for the purpose of this investigation. A sample .csv file containing data from one of the many simulations is included and loaded into the Matlab script. This file (COMSOL_NanostrainExport_7.5E-5m_1500psi.csv) includes the strain data exported from COMSOL for the Model E simulation involving a fracture aperture of 7.5E-5 m and injection pressure of 1500 psi. Comments within the script offer instructions for use. COMSOL files containing the model for both sections of the study are also available. The COMSOL files available include Model A from the section about modeling strain signatures as an indicator of fracture connectivity (UtahFORGE_A) and the model used for the section about parametric modeling for hydraulic test design (UtahFORGE_E). To reduce the file size, the meshes and solutions are cleared. Both models are ready to run after rendering the mesh. The COMSOL and Matlab Files are also available as supplemental files to this PDF in the ProQuest Dissertations and Theses database.

REFERENCES

REFERENCES

Allis, R., Moore, J., Davatzes, N., Gwynn, M., Hardwick, C., Kirby, S., McLennan, J., Pankow, K., Potter, S., and Simmons, S., 2016, EGS concept testing and development at the Milford, Utah FORGE site: Proceedings, 41st Workshop on Geothermal Reservoir Engineering: Stanford, California, Stanford University, v. 41, no. SGP-TR-209, 13 p.

Audigane, P., Royer, J.-J., and Kaieda, H., 2002, Permeability characterization of the Soultz and Ogachi large-scale reservoir using induced microseismicity: Geophysics, v. 67, p. 204–211, doi:10.1190/1.1451573.

Bakker, M., 2008, Sinusoidal pumping of groundwater near cylindrical inhomogeneities: Journal of Engineering Mathematics, v. 64, p. 131-143, doi:10.1007/s10665-008-9244-0.

Bakku*, S.K., Fehler, M., Wills, P., Mestayer, J., Mateeva, A., and Lopez, J., 2014, Vertical seismic profiling using distributed acoustic sensing in a hydrofrac treatment well, *in* SEG Technical Program Expanded Abstracts 2014: Denver, Colorado, Society of Exploration Geophysicists, p. 5024–5028, doi:10.1190/segam2014-1559.1.

Becker, M., and Ciervo, C., 2018, A slimhole approach to measuring distributed hydromechanical strain in fractured geothermal reservoirs: Proceedings, 43rd Workshop on Geothermal Reservoir Engineering: Stanford, California, Stanford University, v. 43, no. SGP-TR-213, p. 12-14.

Becker, M.W., Ciervo, C., Cole, M., Coleman, T., and Mondanos, M., 2017, Fracture hydromechanical response measured by fiber optic distributed acoustic sensing at milliHertz frequencies: Geophysical Research Letters, v. 44, p. 7295–7302, doi:10.1002/2017GL073931.

Becker, M.W., and Coleman, T., 2019, Distributed acoustic sensing of strain at Earth tide frequencies: Sensors, v. 19, no. 9, doi:10.3390/s19091975.

Becker, M.W., Coleman, T.I., and Ciervo, C.C., 2020, Distributed acoustic sensing as a distributed hydraulic sensor in fractured bedrock: Water Resources Research, v. 56, no. 9, 10 p., doi:10.1029/2020WR028140.

Becker, M., and Guiltinan, E., 2010, Cross-hole periodic hydraulic testing of inter-well connectivity: Proceedings, Thirty-Fifth Workshop on Geothermal Reservoir Engineering: Stanford, California, Stanford University, v. 35, no. SGP-TR-188, p. 292-297.

Benato, S., Hickman, S., Davatzes, N.C., Taron, J., Spielman, P., Elsworth, D., Majer, E.L., and Boyle, K., 2016, Conceptual model and numerical analysis of the Desert Peak EGS project: Reservoir response to the shallow medium flow-rate hydraulic stimulation phase: Geothermics, v. 63, p. 139–156, doi:10.1016/j.geothermics.2015.06.008.

Biot, M.A., 1962, Mechanics of deformation and acoustic propagation in porous media: Journal of Applied Physics, v. 33, p. 1482–1498, doi:10.1063/1.1728759.

Chabora, E. et al., 2012, Hydraulic stimulation of well 27-15, Desert Peak Geothermal Field, Nevada, USA: Proceedings, 37th Workshop on Geothermal Reservoir Engineering: Stanford, California, Stanford University, v. 37, no. SGP-TR-194, 12p.

COMSOL AB, 2021, Subsurface flow module user's guide: Stockholm, Sweden, COMSOL Multiphysics®, v. 6.0, 300 p. https://doc.comsol.com/6.0/doc/com.comsol.help.ssf/SubsurfaceFlowModuleUsersGuide.pdf

COMSOL AB, 2021, Structural mechanics module user's guide: Stockholm, Sweden, COMSOL Multiphysics®, v. 6.0, 1774 p. https://doc.comsol.com/6.0/doc/com.comsol.help.sme/StructuralMechanicsModuleUsersGuide.pdf

Daley, T.M., Miller, D.E., Dodds, K., Cook, P., and Freifeld, B.M., 2016, Field testing of modular borehole monitoring with simultaneous distributed acoustic sensing and geophone vertical seismic profiles at Citronelle, Alabama: Field testing of MBM: Geophysical Prospecting, v. 64, p. 1318–1334, doi:10.1111/1365-2478.12324.

Doe, T., McLaren, R., and Dershowitz, W., 2014, Discrete fracture network simulations of enhanced geothermal systems: Proceedings, 39th Workshop on Geothermal Reservoir Engineering: Stanford, California, Stanford University, v. 39, no. SGP-TR-202, 11 p.

Duchane, D., and Brown, D., 2002, Hot dry rock (HDR) geothermal energy research and development at Fenton Hill, New Mexico: Oregon Institute of Technology Geo-Heat Center Quarterly Bulletin, v. 23, no. 4, p. 13-19.

Energy and Geoscience Institute at the University of Utah, 2019, Utah FORGE: Phase 2C topical report: United States, USDOE Geothermal Data Repository, doi:10.15121.1578287.

Finnila, A., Doe, T., Podgorney, R., Damjanac, B., Xing, P., and Associates, G., 2021, Revisions to the discrete fracture network model at Utah FORGE Site: GRC Transactions, v. 45, p. 757-766.

Finnila, A., Forbes, B., and Podgorney, R., 2019, Building and utilizing a discrete fracture network model of the FORGE Utah site: Proceedings, 44th Workshop on Geothermal Reservoir Engineering: Stanford, California, Stanford University, v. 44, no. SGP-TR-214, 12 p.

Fitts, C., 2013, Groundwater science: New York, Academic Press, v. 2, 672 p.

Fokker, P. A., 2013, Numerical modeling of periodic pumping tests in wells penetrating a heterogeneous aquifer: American Journal of Environmental Sciences, v. 9, p. 1–13, doi:10.3844/ajessp.2013.1.13.

Ghassemi, A., and Kumar, D., 2023, Hydraulic fracturing in petroleum and geothermal reservoirs with reference to the Utah FORGE stimulation: Proceedings, 48th Workshop on Geothermal Reservoir Engineering: Stanford, California, Stanford University, v. 48, no. SGP-TR-224, 9 p.

Golder Associates, 2010, Fractured bedrock field methods and analytical tools: Victoria, BC, University of Victoria, Science Advisory Board for Contaminated Sites in British Columbia, v. 1, 99 p.

Gudala, M., Govindarajan, S.K., Yan, B., and Sun, S., 2023, Comparison of supercritical CO2 with water as geofluid in geothermal reservoirs with numerical investigation using fully coupled thermo-hydro-geomechanical model: Journal of Energy Resources Technology, v. 145, doi:10.1115/1.4055538.

Guiltinan, E., 2012, Characterizing well connectivity in fractured bedrock using periodic hydraulic tests [M.S. Thesis]: California State University, Long Beach, 106 p.

Guiltinan, E., and Becker, M.W., 2015, Measuring well hydraulic connectivity in fractured bedrock using periodic slug tests: Journal of Hydrology, v. 521, p. 100–107, doi:10.1016/j.jhydrol.2014.11.066.

Guo, B., Fu, P., Hao, Y., Peters, C.A., and Carrigan, C.R., 2016, Thermal drawdown-induced flow channeling in a single fracture in EGS: Geothermics, v. 61, p. 46–62.

Hardwick, C.L., Gwynn, M., Allis, R., Wannamaker, P., and Moore, J., 2016, Geophysical signatures of the Milford, Utah FORGE site: Proceedings, 41st Workshop on Geothermal Reservoir Engineering: Stanford, California, Stanford University, v. 41, no. SGP-TR-209, 11 p.

Held, S., Genter, A., Kohl, T., Kölbel, T., Sausse, J., and Schoenball, M., 2014, Economic evaluation of geothermal reservoir performance through modeling the complexity of the operating EGS in Soultz-sous-Forêts: Geothermics, v. 51, p. 270–280, doi:10.1016/j.geothermics.2014.01.016.

Jacob, C.E., 1940, On the flow of water in an elastic artesian aquifer: Eos, Transactions American Geophysical Union, v. 21, no. 2, p. 574–586, doi:10.1029/TR021i002p00574.

Jones, C., England, K., Simmons, S., Rose, P., Mella, M., Barker, B., McLennan, J., and Moore, J., 2023, Stimulation, tracers and geochemistry at Utah FORGE: Proceedings, 48th Workshop on Geothermal Reservoir Engineering, SGP-TR-224, v. 48, 9 p.

Kaieda, H., 2012, Ogachi EGS reservoir analysis: Geothermal Resources Council Transactions, v. 36, p. 487-492.

Kelkar, S., WoldeGabriel, G., and Rehfeldt, K., 2016, Lessons learned from the pioneering hot dry rock project at Fenton Hill, USA: Geothermics, v. 63, p. 5–14.

Knudby, C., and Carrera, J., 2006, On the use of apparent hydraulic diffusivity as an indicator of connectivity: Journal of Hydrology, v. 329, p. 377–389, doi:10.1016/j.jhydrol.2006.02.026.

Kumar, C., 2013, Structural analysis with thin elastic layers, COMSOL: https://www.comsol.com/blogs/structural-analysis-with-thin-elastic-layers/ (accessed June 2023).

Lee, S.H., and Ghassemi, A., 2022, Numerical simulation of fluid circulation in hydraulically fractured Utah FORGE wells: Proceedings, 47th Workshop on Geothermal Reservoir Engineering: Stanford, California, Stanford University, v. 47, no. SGP-TR-223, 16 p.

Lei, Q., Gholizadeh Doonechaly, N., and Tsang, C.F., 2021, Modelling fluid injection-induced fracture activation, damage growth, seismicity occurrence and connectivity change in naturally fractured rocks: International Journal of Rock Mechanics and Mining Sciences, v. 138, p. 104598, doi:10.1016/j.ijrmms.2020.104598.

Lellouch, A., Lindsey, N.J., Ellsworth, W.L., and Biondi, B.L., 2020, Comparison between distributed acoustic sensing and geophones: Downhole microseismic monitoring of the FORGE geothermal experiment: Seismological Research Letters, v. 91, p. 3256–3268, doi:10.1785/0220200149.

Li, D., Huang, L., Zheng, Y., Li, Y., Wannamaker, P., and Moore, J., 2022, Feasibility of source-free DAS logging for next-generation borehole imaging: Springer Nature, v. 12, no. 1, p. 11910, doi:10.1038/s41598-022-16027-3.

Lindsey, N.J., Dawe, T.C., and Ajo-Franklin, J.B., 2019, Illuminating seafloor faults and ocean dynamics with dark fiber distributed acoustic sensing: Science, v. 366, p. 1103–1107, doi:10.1126/science.aay5881.

May, D., and Jones, D., 2023, Utah FORGE: Well 16B(78)-32 logs from Schlumberger Technologies: United States, USDOE Geothermal Data Repository, Energy and Geoscience Institute at the University of Utah, doi:10.15121/2001059.

Mcclure, M., 2023, Calibration parameters required to match the Utah FORGE 16A(78)-32 stage 3 stimulation with a planar fracturing model: Proceedings, 48th Workshop on Geothermal Reservoir Engineering: Stanford, California, Stanford University, v. 48, SGP-TR-224, 17 p.

McClure, M.W., 2009, Fracture stimulation in enhanced geothermal systems [M.S. Thesis]: Stanford University, 86 p.

McLennan, J., England, K., Rose, P., Moore, J., and Barker, B., 2023, Stimulation of a high-temperature granitic reservoir at the Utah FORGE site: Society of Petroleum Engineers, doi:10.2118/212346-MS.

Moore, J., McLennan, J., Allis, R., Pankow, K., Simmons, S., Podgorney, R., Wannamaker, P., Bartley, J., Jones, C., and Rickard, W., 2019, The Utah frontier observatory for research in geothermal energy (FORGE): An international laboratory for enhanced geothermal system technology development: Proceedings, 44th Workshop on Geothermal Reservoir Engineering: Stanford, California, Stanford University, v. 44, no. SGP-TR-214, 12 p.

Moore, J., McLennan, J., Pankow, K., Simmons, S., Podgorney, R., Wannamaker, P., Jones, C., Rickard, W., and Xing, P., 2020, The Utah frontier observatory for research in geothermal energy (FORGE): A laboratory for characterizing, creating and sustaining enhanced geothermal systems: Proceedings, 45th Workshop on Geothermal Reservoir Engineering: Stanford, California, Stanford University, v. 45, no. SGP-TR-216, 10 p.

Murdoch, L.C., and Germanovich, L.N., 2012, Storage change in a flat-lying fracture during well tests: Water Resources Research, v. 48, doi:10.1029/2011WR011571.

Nadimi, S., Forbes, B., Moore, J., Podgorney, R., and McLennan, J.D., 2020, Utah FORGE: Hydrogeothermal modeling of a granitic based discrete fracture network: Geothermics, v. 87, p. 101853, doi:10.1016/j.geothermics.2020.101853.

Nathenson, M., 1999, The dependence of permeability on effective stress from flow tests at hot dry rock reservoirs at Rosemanowes (Cornwall) and Fenton Hill (New Mexico): Geothermics, v. 28, p. 315–340, doi:10.1016/S0375-6505(99)00011-5.

Oliver, N., Bruno, M., Diessl, J., Lao, K., and Becker, M., 2018, Measuring formation strain to determine hydraulic connectivity using fiber optic distributed acoustic sensing: Geothermal Resources Council Transactions, v. 42, p. 2240-2251.

Rasmussen, T.C., Haborak, K.G., and Young, M.H., 2003, Estimating aquifer hydraulic properties using sinusoidal pumping at the Savannah River site, South Carolina, USA: Hydrogeology Journal, v. 11, p. 466–482, doi:10.1007/s10040-003-0255-7.

Ratnayake, R., and Ghassemi, A., 2023a, Modeling of distributed strain sensing (DSS) in Utah FORGE stimulations: Proceedings, 48th Workshop on Geothermal Reservoir Engineering: Stanford, California, Stanford University, v. 48, no. SGP-TR-224, 9 p.

Ratnayake, R., and Ghassemi, A., 2023b, Modeling of fiber optic strain responses to shear deformation of fractures: Unconventional Resources Technology Conference (URTeC), doi:10.15530/urtec-2023-3852059.

Renner, J., and Messar, M., 2006, Periodic pumping tests: Geophysical Journal International, v. 167, p. 479–493, doi:10.1111/j.1365-246X.2006.02984.x.

Rogers, A.L., 2017, Poroelastic modeling of groundwater and hydrocarbon reservoirs: Investigating the effects of fluid extraction on fault stability [Ph.D. Thesis]: Massachusetts Institute of Technology, 93 p.

Rutqvist, J., and Stephansson, O., 2003, The role of hydromechanical coupling in fractured rock engineering: Hydrogeology Journal, v. 11, p. 7–40, doi:10.1007/s10040-002-0241-5.

Schill, E., Genter, A., Cuenot, N., and Kohl, T., 2017, Hydraulic performance history at the Soultz EGS reservoirs from stimulation and long-term circulation tests: Geothermics, v. 70, p. 110–124, doi:10.1016/j.geothermics.2017.06.003.

Simmons, S., Kirby, S., Jones, C., Moore, J., Allis, R., Brandt, A., and Nash, G., 2016, The geology, geochemistry, and geohydrology of the FORGE deep well site, Milford, Utah: Proceedings, 41st Workshop on Geothermal Reservoir Engineering: Stanford, California, Stanford University, v. 41, no. SGP-TR-209, p. 22–24.

Tenma, N., Yamaguchi, T., and Zyvoloski, G., 2008, The Hijiori Hot Dry Rock test site, Japan: Geothermics, v. 37, p. 19–52, doi:10.1016/j.geothermics.2007.11.002.

Terzaghi, K., 1923, Die berechnung der durchassigkeitsziffer des tones aus dem verlauf der hydrodynamischen spannungserscheinungen: Sitzungsber. Akad. Wiss. Math. Naturwiss. Kl. Abt. 2A, v. 132, p. 105–124.

Tester, J.W., Anderson, B.J., Batchelor, A.S., Blackwell, D.D., DiPippo, R., Drake, E.M., Garnish, J., Livesay, B., Moore, M.C., and Nichols, K., 2006, The future of geothermal energy: Massachusetts Institute of Technology, 372 p.

Ugueto, G.A., Todea, F., Daredia, T., Wojtaszek, M., Huckabee, P.T., Reynolds, A., Laing, C., and Chavarria, J.A., 2019, Can you feel the strain? DAS strain fronts for fracture geometry in the BC Montney, Groundbirch, *in* SPE Annual Technical Conference and Exhibition: Calgary, Alberta, Canada, OnePetro, doi:10.2118/195943-MS.

Wang, H., 2000, Theory of linear poroelasticity with applications to geomechanics and hydrogeology: Princeton University Press, 314 p.

Winkler, D., Swearingen, L., and McLennan, J., 2021, Utah FORGE: Well 16A(78)-32: Summary of drilling activities: https://gdr.openei.org/submissions/1296 (accessed June 2023).

Xing, P., Damjanac, B., Moore, J., and McLennan, J., 2022a, Flowback test analyses at the Utah frontier observatory for research in geothermal energy (FORGE) site: Rock Mechanics and Rock Engineering, v. 55, p. 3023–3040, doi:10.1007/s00603-021-02604-x.

Xing, P., McLennan, J., and Moore, J., 2022b, Minimum in-situ stress measurement using temperature signatures: Geothermics, v. 98, p. 102282, doi:10.1016/j.geothermics.2021.102282.

ProQuest LLC
789 East Eisenhower Parkway
P.O. Box 1346
Ann Arbor, MI 48106 - 1346 USA